UNIVERSITY OF
KWAZULU-NATAL

INYUVESI
YAKWAZULU-NATALI

MODELLING OF QUANTUM PHASE TRANSITIONS IN DIRAC MATERIALS

by

Musa Alnour Musa Hussien

A dissertation submitted in fullfilment of the

requirements for the degree of

Doctor of Philosophy in Physics

School of Chemistry and Physics

Supervisor

Prof. Aniekan Magnus Ukpong

2022

Abstract

In this thesis, first-principles computations of the electronic ground state are used to investigate the underlying nature of the quantum phase transitions in selected Dirac materials and their associated hybrid materials. Various methods are used to break the symmetry of the ground state electronic structure and to tune the emergent phases. These involve the application of an external electric, magnetic or electromagnetic fields, and the manipulation of the internal intrinsic fields of materials, such as the introduction of strong spin orbit coupling, electron (or hole) doping, including a strong short-ranged disorder potential. The findings show that applying a perpendicular electric or magnetic field with a staggered potential in the underlying lattice allows for a tunable electronic transition between trivial and non-trivial quantum states. Signatures of the near-field electrodynamics of carriers in nanoclusters reveal the appearance of a quantum fluid phase at the distinct energies where topological quantum phase transitions occur. Emergence of the field-induced carrier density wave phase shows that the collective excitation mode is a distinct potential for carrier transmission in spintronic, optoelectronic, and photonic technologies. Furthermore, two types of insulating Dirac material are used as the tunnel barrier region of the perpendicular tunnel junction architecture. The resulting heterostructure is an artificially assembled metal-insulator-metal multilayer, and this serves as a generic platform for characterizing spin transport properties in spintronic devices. The dependence of the emergent phenomenon of proximity-induced magneto-electronic coupling on the tunnel barrier material is unraveled. By analyzing the effect of the changes in the electronic structure on the spin transmission properties, it is found that the metal-insulator-metal platform exhibits a quantum

phase transition by responding sensitively to both the tunnel barrier material and the applied perpendicular electric field during in-service operation of a spintronic device. The results show that when the electric field approaches its critical amplitude, the spin density of states exhibits a discontinuous change from half-metallic to metallic transport character in the presence of monolayer hexagonal boron nitride as a tunnel barrier material, contrary to when the monolayer molybdenum disulphide is inserted in the tunnel barrier region. The role of the applied electric field in the phase transition is characterized in terms of a spin-flip transition and an induced interfacial charge transfer. It is also found that the abrupt discontinuity in the changes in the spin-flip energy with increase in applied electric field provides the necessary and sufficient evidence of a first-order quantum phase transition in the spin transport phase. These findings show that the material of the tunnel barrier layer creates a non-trivial function in defining the magnetoelectric couplings that occur dynamically during spin tunneling.

Declaration

I, **Musa A. M. Hussien**, declare that:

1. The research reported in this thesis, except where otherwise indicated, is my original research.
2. This dissertation/thesis has not been submitted for any degree or examination at any other university.
3. This thesis does not contain other persons data, pictures, graphs or other information, unless specifically acknowledged as being sourced from other persons.
4. This thesis does not contain other persons writing, unless specifically acknowledged as being sourced from other researchers. Where other written sources have been quoted, then:
   (a) their words have been re-written, but the general information has been referenced.
   (b) where their exact words have been used, their writing has been placed inside quotation marks, and referenced.
5. Where I have reproduced a publication of which I am author, co-author or editor, I have indicated in detail which part of the publication was actually written by myself alone and have fully referenced such publications.
6. This thesis does not contain text, graphics or tables copied and pasted from the Internet, unless specifically acknowledged, and the

source being detailed in the thesis and in the References sections.

Signed  .....

Publications

The results and discussion presented in this thesis are based on details of the following publications by this author:

1. Musa A. M. Hussien, and Aniekan Magnus Ukpong. Electrodynamics of topologically ordered quantum phases in Dirac materials. *Nanomaterials*, 11 (11), 2914 (2021). Ref. [1].

2. Musa A. M. Hussien, and Aniekan Magnus Ukpong. Quantum Phase Transition in the Spin Transport Properties of Ferromagnetic Metal-Insulator-Metal Hybrid Materials. *Nanomaterials*, 12 (11), 1836 (2022). Ref. [2].

Academic activities during my PhD

I have participated in the academic activities listed in the following:

1. 18 - 23 Sep. 2022, **Quantum Phase Transitions in Dirac Materials**, Oral presentation at the 1^{st} International Congress on Advanced Computational Modelling of Materials (CAMOM), University of Pretoria, In person, South Africa.

2. 22 - 25 Aug. 2022, **Magnetoelectric and proximity effects in ferromagnetic metal-insulator-metal hybrid materials**, Poster presentation at Psi-k Conference, SwissTech Convention, EPFL, In person, Switzerland.

3. 08 - 12 Aug. 2022, **Emergent quantum matter in artificial two-dimensional materials**, 31^{st} Jyväskylä Summer School, University of Jyväskylä campus, Online, Finland.

4. 01 Jul. 2022, **Advanced Magnetoelectric Nanocomposites and Their Applications**, Nanomaterials Webinar, Online, Switzerland.

5. 16 - 21 May 2022, **Machine Learning in Electronic Structure and Molecular Dynamics**, The Abdus Salam International Centre for Theoretical Physics (ICTP-EAIFR), In person training, Rwanda.

6. 09 - 10 Dec. 2021, **Electric-Field-Induced Quantum Phase Transition in Multilayer Heterostructures**, Postgraduate Research and Innovation Symposium (PRIS), University of KwaZulu-Natal, Oral presentation, Online, South Africa.

7. 18 - 19 Oct. 2021, **Spin Control in Twisted van der Waals Heterostruc-**

tures, Institute of Physics (IOP), CMD 29 Online Series, UK.

8. 23 - 27 Aug. 2021, **Spintronics and Magnetism on 2D Materials**, Online EPFL-ETHZ Summer School, Zürich.

9. 30 Nov. - 02 Dec. 2020, **Field-tunable Topological Quantum Phase Transitions in Dirac Materials**, The 14^{th} CHPC National Conference, Centre for High Performance Computing (CHPC), Micro-Talk (Poster), Online, South Africa.

10. 18 - 20 Nov. 2020, **African Physical Society (AFPS) International Conference**, The Abdus Salam International Centre for Theoretical Physics (ICTP), Online, Italy.

11. 16 Apr. - 29 May 2020, **Solid State Physics in Quarantine**, The Abdus Salam International Centre for Theoretical Physics (ICTP), Online, Italy.

12. 10 - 21 Jun. 2019, **1^{st} Southern African School on Electronic Structure Methods and Applications (SASESMA-2019)**, University of Pretoria, South Africa.

13. 17 Oct. 2019, **Strain Tunable Quantum Phase Transition in Bulk $\mathbf{Bi_2Se_3}$**, Postgraduate Research and Innovation Symposium (PRIS), University of KwaZulu-Natal, Poster Presentation, South Africa.

Dedication

To the soul of my father,

To my mother,

To my brother Mutasim,

To my wife,

To my son Rafi,
For their love and support.

Acknowledgements

First and foremost, I thank God almighty for his many blessings, which He has given me throughout this journey and for the success.

I would like to express my sincere gratitude and give warm thanks to my supervisor, Prof. Aniekan Magnus Ukpong for his guidance, help and support since 2019. His insightful thoughts, expertise in Theoretical and Computational Condensed Matter Physics and deep thinking in exotic physics have been a guiding beacon of my research work. I feel entirely different whenever I remember how I started in this field compared to what I look like now. No matter what I write about him, I will never give him enough credit for what He has taught me. He has been like a ray of light for me with his illuminating ideas.

I want to thank the following people for their assistance and support in the operation of some computational tools and for insightful discussions. In particular, Dr Arwa and Dr Gamar for their time teaching me Linux OS and electronic structure calculations. Dr Layla Martin-Samos for assistance with Quantum ESPRESSO. Prof. Jose Lado for developing the Quantum Honeycomb software and for his helpful comments on the code modifications. Dr Alexander Smogunov for helping me to establish a consistent material structure for the conductance calculations using the PWCOND package. Also, I would like to thank my teachers: Prof. Abdelnabi Ali, Prof. Elhadi Arbab, and Mr Mohammed (Telly), for advising me academically since the time of my undergraduate studies, and for giving me many opportunities, support, and encouragement in physics.

I am grateful to everyone who taught, helped, and encouraged me during my ed-

ucational journey. Also, the University of KwaZulu-Natal for the study opportunity, particularly the Physics Department at Pietermaritzburg campus. Many thanks the Ministry of Higher Education and Scientific Research of Sudan, Omdurman Islamic University, and the National Research Foundation (NRF) for funding. Thanks to the Center for High-Performance Computing South Africa for computing time on the Lengau Supercomputer and for providing computational software support under Research Program No. MATS0941.

Abbreviations

- QPTs: Quantum phase transitions
- TMDCs: Transition metal dichalcogenides
- DMs: Dirac materials
- DFT: Density functional theory
- pMTJ: Perpendicular magnetic tunnel junction
- TQPTs: Topological quantum phase transitions
- TMR: Tunneling magnetoresistance
- QCP: Quantum critical point
- MZMs: Majorana zero modes
- BEC: Bulk-edge correspondence
- CMP: Condensed matter physics
- SOC: Spin orbit coupling
- HK: Hohenberg and Kohn
- KS: Kohn-Sham
- GS: Ground state
- PP: Pseudopotential
- XC: Exchange-correlation
- PAW: Projector augmented wave

- TB: Tight-binding model
- LCAO: Linear combination of atomic orbitals
- QE: Quantum ESPRESSO
- TRS: Time-reversal symmetry
- BZ: Brillouin zone
- QSHE: Quantum spin Hall effect
- FDTD: Finite-difference time-domain
- PDOS: Projected density of states
- TI: Topological insulator
- BI: Band insulator
- SL: Single layer
- TCM: Transition contribution map
- PC: Parallel configuration
- APC: Anti-parallel configuration
- TODs: Topological order parameters
- TPDs: Topological phase diagrams
- CDW: Charge density wave

Contents

List of Figures

List of Tables

Chapter 1

Introduction

Dirac materials are condensed matter systems whose low-energy excitation spectrum favors the propagation of massless Dirac particles over conventional fermions. Weyl semimetals and two-dimensional materials such as graphene, transition metal dichalcogenides, and their heterostructures are examples of such systems. Low energy excitations in 2D-electron gas (2DEGs) materials like graphene, monolayer boron nitride, germanene, stanene, and their heterostructure multilayers, transition metal dichalcogenides (TMDCs), topological insulators, and d-wave superconductors, superfluids do not obey the Schrödinger-type Hamiltonian. Material with similar electronic properties share an overarching fundamental similarity because the Dirac-type Hamiltonian characterizes their fermionic excitations. This emergent behaviour in a condensed matter systems typifies the class of solid-state systems known as Dirac materials (DMs). The consequence is that their energy band extrema are located at corners of the first Brillouin zone (BZ) at points K and K'.

Thus, it is possible to control the intrinsic carrier transport by breaking the symmetry of the electronic structure using strategies like electrostatic gating, application of external disorder potentials, doping, among other possibilities. Specific symmetries of the material control collective excitations in DMs. Breaking the time-reversal, space-inversion, or spin-orbit coupling, symmetry can generate a finite Dirac mass in the dispersion spectrum. This creates a plethora of intriguing new symmetries in the electronic structure that manifest as emergent quantum phases

[8]. For example, a recent study shows a co-existence of type-I and type-II of topological surface states and 3D bulk Dirac fermions in a single d-orbital manifold of the TMDCs [9]. These quantum phases of matter are believed to exist at absolute zero only, and it is not yet well understood how their collective degrees of freedom can be stabilized at finite temperature.

Quantum phase transitions, which manifest as non-analyticities in the spatial or temporal evolution of the time-independent Hamiltonian of closed systems, is currently at frontiers of contemporary research in the non-equilibrium quantum dynamics of condensed matter systems. For instance, a novel topological quantum phase has been reported recently to have zero Berry curvature [10]. Research in topological physics traditionally focuses on characterising the effects that are generated on the pseudospin, valley quantum numbers, Berry phase curvature and Chern number of topological phases. This is done by quenching or ramping up a parameter of the Hamiltonian [11]. Unlike graphene, some other DMs possess a direct band gap making it trivial to control and tune any such emergent phases, and the underlying phase transitions. In TMDCs for instance, the Dirac-type dispersion gives rise to the $\pm\pi$-Berry phase at each valley [12]. Since the valley Berry phase originates from the electronic band structure, it is equally crucial to determine to what extent the Berry phase for the electrons wave functions is connected with emergent quantum phases in DMs.

In strongly-correlated electron systems such as d-wave superconductors, the electron-electron pairs (i.e. the Cooper pairs) that form through electron-electron correlations, and the electron-hole pairs (i.e. the excitonic pair) give rise to topologically nontrivial superconductivity [13–15]. Determining how Coulombic interactions like electron-ion attraction, electron-electron correlation, relativistic spin-orbit coupling, and electron-phonon coupling affects topological quantum phase transitions in DMs is central to understanding the physics. Insights from such underpinning understanding could also inspire a new range of exotic technologies. For instance, see [16–18].

In proximitized semiconductor-superconductor hybrid nanowires, localized zero-

energy modes of the Bardeen-Cooper-Schrieffer Hamiltonian manifest in condensed matter systems as a unique quantum phase known as Majorana zero modes (MZMs). Their propagation as chiral edge modes in topological superconductors yield exotic half-integer spin quasiparticles, which are uniquely their own antiparticles. Unlike bosons and fermions, MZMs are non-Abelian anyons and support braiding statistics in the fractional quantum Hall regime. This forms the technological basis for topological quantum computation using fault-tolerant quantum computers. Which of the braiding operation arises from the non-local encoding of quasiparticle states, making them insensitive to errors that happened due to the local perturbations.

The operations of braiding are protected-topologically insofar as the MZMs are exponentially pinned in the vicinity of zero energy when spatially separated. Since the symmetry of Majorana fermions protects conductance quantization against disorder, local perturbations and tunnel coupling variations [19], it is a subject of considerable scientific concern to realize the nature of the transition barriers among condensed phases that host MZMs in coexistence with any other localized zero-energy modes at absolute zero, such as the Andreev (and Shiba) bound states.

The artificially-stacked ferromagnetic metal-insulator-metal heterostructure is the most relevant multilayer material in this thesis. Its insulator layer, which also constitutes the tunnel barrier layer of the perpendicular magnetic tunnel junction (pMTJ) is a Dirac material. From a theoretical viewpoint, this hybrid material is crucial for designing spintronic and optoelectroinic devices based on the pMTJ architecture. Recent studies have shown that it gives a high fidelity performance in spin inversion and filtering.

Therefore, this thesis will focus on investigations of the underlying quantum phase transition in selected Dirac materials. It is shown that applying two external fields, such as an exchange field or Rashba SOC with a staggered potential in the underlying lattice, allows electronic transitions between trivial and topological quantum states. Also, it is shown that when a Dirac material is integrated into the perpendicular magnetic tunnel junction (pMTJ), the application of a perpendicular electric field is characterized by a spin-flip transition, which leads to a discontinu-

ous change from the half-metallic to full-metallic transport phase. The implications of these findings are discussed to show the relevance of the electronic transition in emergent technological applications in spintronics, optoelectronics, nanophotonics and plasmonics.

1.1 Aims and objectives of the thesis

In this thesis, the laws of quantum mechanics are applied using the computational methods implemented within density functional theory (DFT) to study the electronic ground-state and the emergent quantum phases and their topological properties in selected Dirac materials. The objectives of this thesis are:

- To understand the fundamental nature of the topological electron state in Dirac materials.
- To unravel the mechanisms of topological phase transitions and ways to tune them in Dirac materials.
- To propose models for understanding the emergent phenomena of collective phases and the effect of perturbative disorder potentials on Dirac materials.
- To characterize the effectiveness of an external field on the quantum phases observed in Dirac materials.
- To develop a reasonable interpretation of topological electronic states and their associated transport phases for emerging applications in spintronics and optoelectronics applications.
- To investigate the effects of incorporating a Dirac material as the tunnel barrier layer in symmetric perpendicular magnetic tunnel junctions under a symmetry-breaking field.

1.2 Thesis structure

This thesis is organized as follows: Chapter 2 presents a general introduction to the low-energy physics of Dirac matter and describes the origin of Dirac Materials.

Chapter 3 discusses the theoretical framework used in this thesis to solve the many-body problem. This computational framework includes the ab initio approach of solving the many-body Schrödinger equation within the Kohn-Sham ansatz of density functional theory and the tight binding model of the electronic structure on the the honeycomb lattice. These two approaches to the electronic structure calculation are combined to study the spin transport phenomenon in Dirac materials within the ballistic regime. Chapter 4 presents the computational techniques used to calculate the electronic ground-state of the many-body system, the method of renormalizing the low-energy electronic structure of bulk TaAs on the band structure of a graphene sheet, and the computational setup of artificial multilayer heterostructures. The results are presented and discussed in chapter 5. Finally, the conclusions are presented in chapter 6.

Chapter 2

Dirac Materials

This chapter introduces the concept of Dirac materials. It also presents the quantum mechanical origin of Dirac materials as the theoretical basis for understanding the low-energy physics of Dirac matter. Selected examples of Dirac materials are discussed to lay the theoretical framework for computational exploration of their underlying low-energy dispersion characteristics and the associated quantum phase transitions.

2.1 The origin of Dirac materials

The insightful contributions of Paul Adrien Maurice Dirac [20], Ettore Majorana [21], and Herman Klaus Hugo Weyl [22] to particle physics provided the first theoretical basis for describing electrons and some subatomic particles. Over the years, these foundational theories have also been used in condensed matter physics (CMP) to understand the low-energy excitation state of carriers in solids. This is valid when carrier transport is modelled as if the valence electrons are traveling in the regular periodically-repeated potential experienced by valence electrons due to the presence of the immobile ionic cores in a crystal, subject to Bloch's theorem.

Recently, quantum field theory (QFT) has emerged as the most accurate mathematical and conceptual framework in theoretical physics. It combines classical field theory, special relativity, and quantum mechanics [23]. QFT also provides the the-

oretical framework for describing the phenomenon of phase transition. It provides the tools required for developing a fundamental understanding of phase transition in a broad range of disparate systems. This includes spontaneous symmetry breaking transition, the evolution of magnetism in materials, the order-disorder transition in condensed matter systems, as well as in the early universe, and the behaviour of quarks. Quantum chromodynamics (QCD) [24], and quantum electrodynamics (QED) [25] are the first two completely developed quantum field theories. QCD describes the strong interactions between elementary particles while QED accurately describes the interactions between charged particles. In the first part of the research results reported in Chapter 5 of this thesis, tunable topological and trivial quantum phase transitions in Dirac materials have been considered. In the second part of the results, the trivial quantum phase transition from half-metallic to metallic transport of carriers in the ferromagnetic metal-insulator metal heterostructure is considered.

Nevertheless, Dirac developed his equation to elucidate an electron, which satisfies the relativistic dispersion relation:

$$E^2 = p^2c^2 + m^2c^4 \tag{2.1}$$

or it can be written as:

$$E = \pm\sqrt{p^2c^2 + m^2c^4}, \tag{2.2}$$

where E denotes the electron energy, p denotes the momentum, m and c represent the mass and light velocity, respectively, [20]. Equation (2.2) demonstrates the combination between the quantum state of a single particle and the relativistic effect. The solution of equation (2.2) suggests the existence of negative energy. It was later realized that this kind of energy is related to the new class of particles, known as anti-particles [20, 26]. This anti-particle shared the same mass as an electron, but had a dissimilar charge. The anti-particle of an electron discovered shortly after Dirac's prediction, is the positron. The Dirac wave function contains a four-component spinor for the electron, while the massless fermion has two Weyl spinors [22].

Figure 2.1 shows the difference between Schrödinger and Dirac Hamiltonian in terms of their low energy spectrum for quasi-particles. The finite band gap in an insulator could be tuned to disappear by breaking the symmetry of the ground state. This can be achieved through thermal or electrical excitation, creation of electron-hole pairs, and the application of an electric or magnetic field.

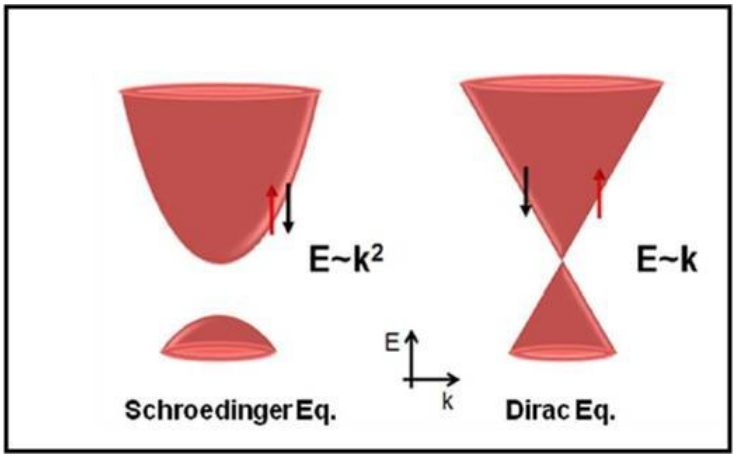

Figure 2.1: The low-energy excitation spectrum for the massive electrons obeying Schrödinger's Hamiltonian (H_S) on the left. The massless electrons possess a linear dispersion and follow Dirac Hamiltonian (H_D) on the right [3].

The quasi-particles in doped semiconductors or metals obey the following Schrödinger Hamiltonian:

$$H_S = \boldsymbol{p}^2/2m^*, \tag{2.3}$$

where m^* denotes the effective mass of fermions. Fermionic quasi-particle dispersion follows the Dirac-type Hamiltonian of the form:

$$H_D = c\boldsymbol{\sigma}.\boldsymbol{p} + mc^2\sigma_z, \tag{2.4}$$

where $\boldsymbol{\sigma} \equiv (\sigma_x, \sigma_y, \sigma_z)$ denotes the Pauli spin matrices. However, when $m \longrightarrow 0$ the gap will disappear [27], and the quasi-particle spectrum is characterized by a linear dispersion as shown in the right hand side of Fig. 2.1. This is quite unlike the parabolic dispersion observed in metals and semiconductors.

2.1.1 Two dimensional materials (2DMs)

Symmetry and dimensionality play significant roles in condensed matter phases. When a layered 3D material is exfoliated by thinning down to their mono-atomic layer boundaries, the material is scaled to its 2D form and the effect of quantum confinement on the electron state becomes important due to its reduced dimensions. This class of materials is called two-dimensional materials (2DMs). They have various new features that differ from their bulk analogues because electrons can only move freely along their 2D or a plane up to a few nanometers [28]. Since discovering graphene [29, 30], several studies have been dedicated to exploring a large number of 2D materials as shown in Fig. 2.2.

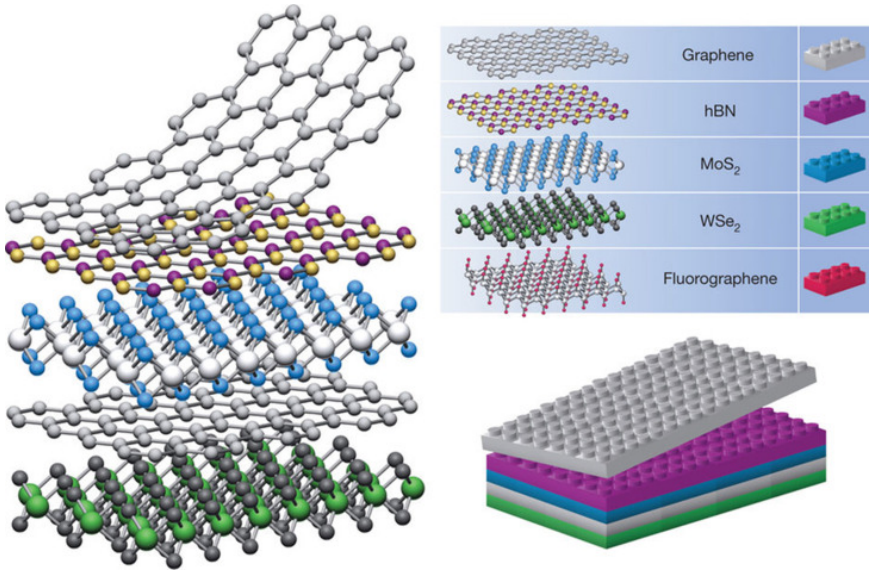

Figure 2.2: The facinating quantum world of two dimensional materials [4].

Insulating 2D materials like hexagonal boron nitride (h-BN) and transition metal dichalcogenide (TMDC) [31, 32] can be assembled into free-standing van der Waals multilayer heterostructures [see Fig. 2.2 (bottom right)]. They can also be incorporated into the tunnel barrier region to build a perpendicular magnetic tunnel junction by sandwiching them between two similar or dissimilar ferromagnetic leads. This offers unique possibilities for exploring new phenomena and interesting applications. For instance, spin magnetotransport with spintronic devices forms a domain for which a high tunability of the transport signatures is desirable to control

emergent carrier transport. This is because of their high-fidelity operation due to efficient spin inversion and filtering, especially when a suitable Dirac material is incorporated to improve the device robustness against thermal and oxidative stresses and heat dissipation effects.

The discovery of intrinsic 2D magnetic materials with high spin-polarization is important for the next generation of nanoscale MTJs. Thus, the fabrication and characterization of MTJs based on 2D materials has led to many unique characteristic properties. This is because pure spin current generated from pMTJs is highly sensitive to QPT-induced anisotropies. However, because neither the underlying anisotropies nor their coupling mechanisms are well-understood. Gaining insights into such phenomena is a vital step toward achieving a lower energy delay product [33].

Due to their wide band gap, the monolayers of hexagonal boron nitride and molybdenum disuphide MoS_2 [34] can suppress resonant tunneling from wave coupling via evanescent quantum states. Since their electronic band structure is dependent on thickness, it is possible to tune their carrier transport behavior from the semi-conducting state to metallic state. Furthermore, MoS_2 has a direct gap in the monolayer phase [35, 36]. This makes it attractive material for optoelectronic applications that require direct inter-band transitions. Combining 2D materials to build multilayers show new properties, and unique advantages in device technology due to the interplay of robust covalent intralayer bonding and the weak interaction of interlayers [37–40].

2.1.2 Graphene

In the far past, the scientific community believed that two-dimensional (2D) materials might not exist [41]. Theoreticians had predicted that the lower dimensional crystals are likely to disintegrate at low temperatures above 0 K. This is because of considerable atomic lattices displacements resulting from several sources of thermal fluctuations [42]. This prediction was strongly supported by some experimental results that suggest that the melting point of a thin-layered material reduces with

decreasing thickness [43, 44]. However, following the exfoliation and experimental characterization of the graphene sheet by Novoselov, et al in 2004, its mechanical robustness and thermodynamics stability demonstrate that the graphene sheet is an authentic 2DM. Figure 2.3 shows the schematic diagram of the exfoliation of graphene sheets from graphite. [29, 30].

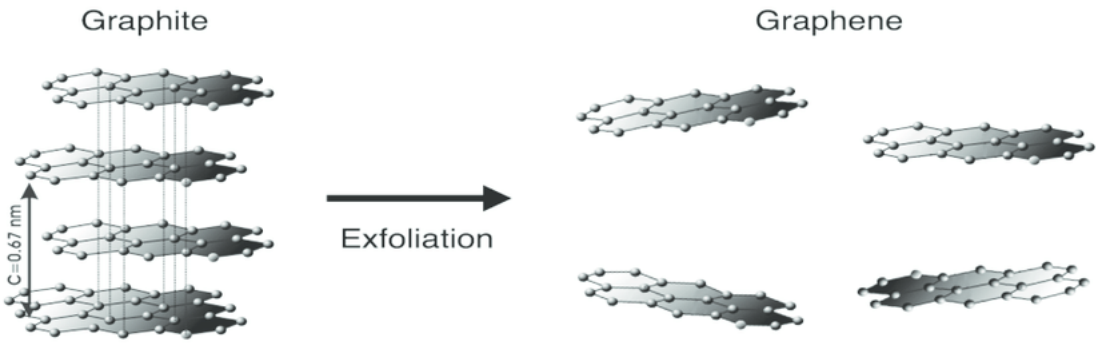

Figure 2.3: The exfoliation of graphene from Graphite [5].

Graphene is the thinnest and strongest material known. It is made of carbon atoms joined with three nearest neighbours in the form of a honeycomb lattice crystal structure of [45, 46], nanostructure [47]. It has prodigious properties that make it a fascinating material. Graphene has remarkable physical and chemical properties. This includes ballistic conductance, mechanical flexibility, non-ionic covalent bonding and excellent light absorption capabilities. Its high carrier mobility makes it a good conductor of heat and electricity. These impressive properties make it an attractive material for use in a wide range of applications. The potential applications of graphene are highly diverse. It can also be combined with other materials to create new devices with superior properties. The possible technological applications of graphene and its derivatives include: field effect transistors (FET) [48–50], integrated circuits [51, 52], sensors [53, 54], supercapacitors [55, 56], DNA sequencing [57], water treatment [58], antennas, flat-panel and touchscreen displays (for LCD or OLED electronics) [59], dye-sensitized solar cells [60] spin valves [61], amongst others.

The propagation of electrons in the graphene lattice follows ballistic dynamics. This makes the electrons to behave as if they have lost their mass and behave as

massless particles. Equivalently, this leads to a system of electrons that behave like quasi-particles. These massless particles are described by the Dirac equation for spin-1/2 particles [7, 62]. In 2005 Geim's group and others discovered anomalous quantum Hall effect (AQHE) samples of graphene that were obtained through cleavage method [63, 64]. The observation supports earlier theoretical predictions of the existence of the Berry phase in a system of massless particles [65]. These observations have spurred the search for signatures of similar exotic effects in other types of Dirac materials.

2.1.3 Tantalum Arsenide (TaAs)

In the new class of materials known as Weyl semimetals (e.g., TaAs, NbAs and Na_3Bi), the valence and conduction bands cross at specific points of the Brillouin zone known as Weyl nodes. These materials are considered to be the 3D analogs of graphene whenever time-reversal or structural inversion symmetry is broken. When the position of the Fermi level lies at such nodes (or close to them), the electrons can behave as relativistic Weyl fermions and exhibit a linear dispersion in reciprocal space. Such nodes exist in pairs that possess opposite chirality. These are characterized by integer topological charges of opposite sign associated with singular points of Berry curvature in momentum space.

Nevertheless, separated Weyl nodes are also carrier transport states with guaranteed topological protection. This is because any perturbation that does not violate the translational symmetry can only shift the position of the nodes without annihilating them. The consequence is the valence electrons in such materials exhibit peculiar properties such as magnetic monopole and anomalous non-conservation of a chiral current [66]. The surfaces of topological insulators host chiral surface states that are protected by the energy band gap in the bulk state [22, 67–71]. Theoretical and experimental studies supported by photoemission spectroscopy reveal the non-conserving inversion symmetry of the Weyl semimetal state in TaAs [66, 71–73]. The resulting transport signature shows a significant increase in mobility [74]. Transport through the underlying nontrivial electron states of Weyl semimetals is different

from transport through topological insulator. This is because the properties of the chiral state of Weyl semimetals are not sensitive to dimensionality.

In this thesis, the dimensional insensitivity is serves as the theoretical basis for the study of the carrier transport behaviors that emerge from the renormalization of the electronic structrure of bulk TaAs on the graphene lattice. The emergent massless fermions in TaAs will have lifted degeneracies at the nodal points and share the same transport signature as graphene from their energy spectrum. In addition, the symmetry breaking operation modulates the quasi-particles dispersion between Dirac to Weyl equation [22, 75–79]. This is because their low-energy quasi-particle excitation spectrum is similar to those of Dirac materials, and the strong spin orbit coupling that characterizes their electronic structure makes it promising for applications in spintronics [80, 81].

2.2 Carrier transport in Dirac Materials

Dirac matter is attracting research interest because it defines the unifying structure of the new category of materials called Dirac materials (DMs) [27]. The CMP has witnessed a sudden increase in materials with Dirac fermion-like low energy excitations [20], such as the superfluid phases of ^{3}He and ^{4}He [82, 83], high-temperature superconductors (d-wave), graphene [84], monolayers of some transition metal dichalcogenides and topological insulators [85–87]. The main similarity is that they all obey the Dirac-type Hamiltonian H_D instead of the Schrödinger Hamiltonian H_S. Also, their low-energy excitations act like massless Dirac particles. Also, DMs responsed to the effect of applied external fields. They control their low energy excitations via dimensionality, in addition to the intrinsic symmetries in each DMs [88].

An additional significant feature of Dirac electrons is that they allow ballistic conductance through the surface states of DMs, and this electronic property is controllable using an external magnetic field. These drive the possibilities of observing exotic phenomena and unique new properties in CMP through tunability of the electron states and breaking of the global symmetry of the transport state of DMs.

2.3 Quantum phase transitions (QPTs)

There are several occurrences of the phenomenon of phase transition in physical processes. Examples include the temperature-dependent changes in the phase of water, paramagnetic-ferromagnetic phase transition, the transition of metals to the superconducting phase, and the metal-insulator transition materials undergo an electronic phase change from a metallic to an insulating state as a function of applied external conditions, i.e., temperature, pressure, or doping [89]. The universe's birth passed via transition from a singularity point with a high density, pressure and temperature to today's world. However, the question that comes to our mind is whether the temperature is the primary and only parameter that drives phase transitions?. At zero temperature, the quantum fluctuations substitute thermal fluctuations, and the quantum phase transitions occur.

A classical phase transition (CPT) is characterized by a sudden, qualitative, change in the properties of a physical system when parameter, such as temperature, is tuned through a critical value. In the vicinity of such transitions, remarkable emergent behaviors can be observed. Such behaviors include universality, scale invariance and criticality. Such critical phenomena can be understood using theoretical concepts such as the renormalization group and associated effective field methods. The renormalization group relates a set of effective descriptions on a range of length scales, and also provides a framework for the calculation of physical observables using mean field approximations. Over the last thirty or so years, the field of quantum phase transitions (QPTs) has evolved to become a new research area [90]. The QPT occurs at 0 K as a distinct change from one ordered quantum state to another [91, 92]. In the mesoscopic transport of spin current, which is relevant to this thesis, the QPT denotes the change in the spin transport phase of carriers from one quantum state to another at zero-temperature. Since this change occurs at 0 K, the QPT is driven by quantum (rather than thermal) fluctuations. Hence, an equivalence to the transition state expected in a classical phase transition does not exist.

The phenomenon of quantum fluctuation can be attributed to the probabilistic nature of the ground state in a many-body solid determined quantum-mechanically

within the self-consistent field approximation. Since the phenomenon cannot be traced to the localized action of a change in the Hamiltonian, it cannot cause a change in the total energy the system. Thus, the causes of QPTs are distinctly different from the causes of quantum fluctuation. By contrast, the QPT is driven purely by quantum fluctuations [93]. Parameter changes that break the symmetry of the Hamiltonian will spontaneously drive the QPT.

For instance, consider that during the transport of spin angular momentum under an applied voltage, spin carriers will respond sensitively to the applied symmetry breaking fields in the presence of intrinsic quantum fluctuations. This response leads to non-local discontinuities, such as spin carrier de-population around the Fermi level and chiral anomalies, in the spin-dependent topology of the Fermi-surface. These lead to nontrivial effects that influence the spin-dependent tunneling with perpendicular magnetic tunnel junctions. These effects become important when the pMTJ is subjected to the effects of external bias potential, voltage drop, an external electric, or magnetic field during its in-service operation in a spintronic device.

2.3.1 Signatures of classical and quantum phase transitions

Consider that, the QPT only takes place at $T = 0$ K under quantum fluctuations. QPTs differ from CPTs because they only occur at a specific finite temperature T [89, 91, 94]. Adjusting a non-thermal control parameter (λ) of the Hamiltonian can drive the system towards the quantum critical point (QCP) at zero temperature. Otherwise, if the Hamiltonian drive has an explicit dependence on temperature, then any ensuing phase transition is purely classical. Examples of such parameters include external electric field, magnetic field, material type, and associated defect states, and sub-lattice disorder potentials. When the Hamiltonian is tuned through the parameter space λ, the electronic ground state of the many-body system is characterized by spontaneous non-conserving symmetry or a changing of topological invariant [89, 95].

Figure 2.4 describes the signatures of the phase transitions in condensed matter from the classical and quantum point of view in terms of temperature T and the

Hamiltonian parameter λ. The phase diagram shows two significant probabilities for the temperature $T > 0$ in the neighborhood of a QCP. Figure 2.4(a) shows the first type of probability. In this case the thermodynamic singularity is present only at zero-temperature at the critical point. This is the point where quantum fluctuations govern the dynamics of the system. Instead of varying the temperature at the critical point, a controlling Hamiltonian $H(\lambda)$ can be tuned, and all $T > 0$ features are analytic as a function of λ near $\lambda = \lambda_c$. However, the second probability is shown in Fig. 2.4(b). It shows a line of $T > 0$ K. This finite-temperature phase boundary denotes a second-order phase transition. The two phase boundaries terminate at the QCP where $\lambda = \lambda_c$ [91].

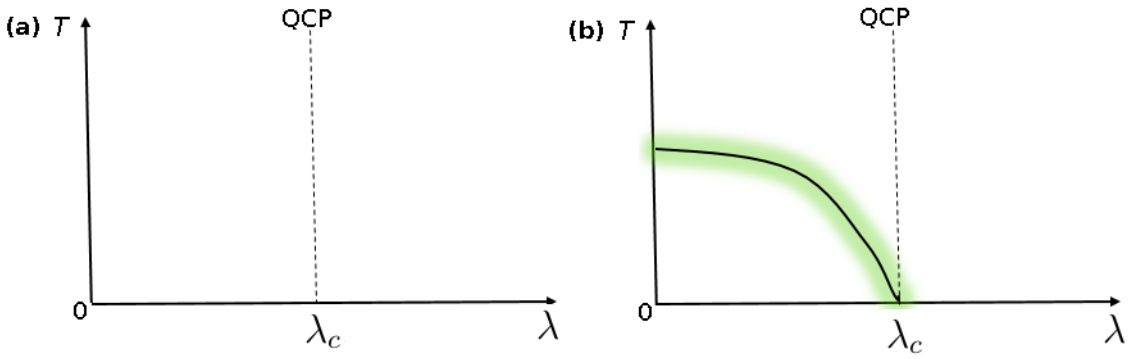

Figure 2.4: Phase diagrams of temperature (T) as the function of order parameter λ near quantum phase transitions. The quantum critical point is identified with a vertical dashed line at $\lambda = \lambda_c$ and $T = 0$, as the point where the order parameter reaches the critical value λ_c, at zero temperature. (a) The ordered phase exists at $T = 0$. (b) An ordered phase exists at finite temperature or $T > 0$. The shaded area denotes the critical region where thermal fluctuation takes place.

Whenever $T \neq 0$, there is a competition between the energy scales $k_B T$ ($\hbar\omega$) of thermal and quantum fluctuations, respectively. In this case ω defines the characteristic frequency of oscillation of the internal degrees of freedom of the system. It is inversely proportional to the correlation time. By contrast, quantum fluctuations control dynamical behavior of the system whenever the condition, $\hbar\omega = k_B T$, is satisfied. In this case, the critical quantum point corresponds to the value of the order parameter at $T = 0$. This is the point where separate quantum phases coexist. From the above conditions, a classical illustration of these principles are applied to critical degrees of freedom in the quantum dynamical system denoted by the spin

current. This concept works well in the shaded area in Fig. 2.4(b) [91]. Generally, the arguments of quantum mechanics do not work well in describing the criticality of the dynamical system at finite temperatures. However, quantum mechanics plays a significant role at zero temperature.

2.4 Topological quantum phase transitions (TQPTs)

Topological phases have attracted the scientific community's attention in the past decades. In condensed matter systems, the notion of topology characterizes the geometrical property wherein the dimensionality of space cannot be changed under continuous deformations. Topological phases are characterized by the topological invariant or any other non-local metric of the topological order. Thus, topological quantum phase transitions (TQPTs) occur only between two or more topologically-protected or nontrivial electronic phases. Topological order metrics remain unchanged by the inclusion of perturbation terms in the Hamiltonian, or by the introduction of a localized short-ranged disorder in the system. As such, metrics of topological order have become useful as topological quantum numbers in the characterization of emergent quantum phases in CMP. For instance, its beneficial use in distinguishing between the topological order of an electronic phase has been demonstrated recently [96–100]. Some of the materials that host various topological phases include topological insulators (TI), superconductors, TMDs and Dirac semimetals.

Figure 2.5 shows the electronic band structure of a system as a dispersion relationship between energy band states and the wave-vector $\boldsymbol{k}$ in the first Brillouin zone. The two gapped bands, in the left and right of Fig. 2.5, are characterized by non-inverted and inverted bands, respectively. The presence of the bandgap protects their topological edges. However, introducing spin-orbit coupling can tune the electronic state and change the system into the metallic state (see Fig. 2.5(b)) from the band insulator (see Fig. 2.5(a)). It is also possible to reopen another type of band gap, as seen in Fig. 2.5(c), due to the topological quantum phase transition.

The top of the valence band and the bottom of the conduction band are inverted in Figure 2.5(c) because of spin orbit interaction. The effect of the SOC in driving

the emergence of band inversion is intricately related to TQPTs. For instance, when the spin-orbit coupling strength is reduced, the topology of the inverted band can recover a trivial configuration through the gap closing mechanism. Thus, modifying the strength of the spin orbit interaction is a veritable method for controlling the topology of electronic bands and induce a QPT between two topological phases.

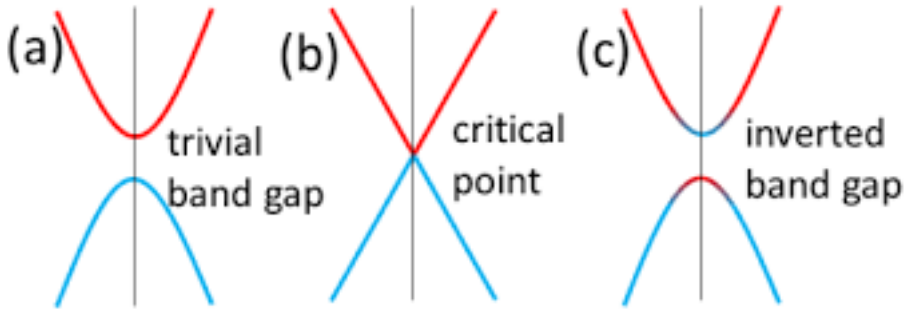

Figure 2.5: Topological quantum phase transition in the electronic band structure. (a) Ordinary band insulators, (b) closed band at a critical point, and (c) band-inverted insulators [6].

The distinction between topological phases with a bandgap cannot be adiabatically linked if the system changes between phases. Therefore achieving the TQPT without closing the energy band gap must be done through inversion of band topology. An experimentally-feasible way to explore such TQPTs is to find physical mechanisms and microscopic processes that can cause a discontinuous change in the underlying signature of a particular physical reaction. The signatures of TQPTs have also be investigated experimentally, using microscopic probes as electromagnetic field [101–103] and piezoelectric response [104].

Topological protection of the carrier transport state is essential for realizing energy-efficiency, and low-power consumption, in device applications. This is usually achieved through the minimization of Joule heating for heat dissipation during carrier transport. This is particularly essential for spintronic devices, data storage devices that operate on all-spin-logic, nanophotonic and nanopalsmonic devices , among others. Dirac materials [27] is a unique class of materials with candidates that can provide such quantum states. For this reason, their monolayers can be integrated into metamaterials and multilayers to ensure the presence of chiral quantum

states. The characteristic of the nontrivial quantum phase of carriers is that their topological edge states remain unchanged when they are subjected to perturbations like thermally-induced fluctuations, impurity states, localized disorder and long-raged interactions. Also, it is protected on graphene by bulk-edge correspondence [105–110].

It is argued in [1] that, when a Dirac material is integrated into the multilayer heterostructure [2], the intrinsic presence of the heterobilayer interface with a Dirac material, or a free surface, will lead to formation of chiral edge states due to bulk-edge correspondence of electron states. The emergence of topologically protected electron states is guaranteed through the bulk-edge correspondence principles. This principle enforces the one-to-one relation between the bulk and edge properties generated from bulk electron states and those from chiral edge states that are found mostly in topologically nontrivial systems, such as Dirac materials. The application of symmetry breaking fields to the electronic ground state of the equivalent electronic structure projected on the lattice of pristine graphene at 0 K is found to lead to distinct topological quantum phase. Topological phase diagrams are obtained to show discontinuities in the metrics of topological order quantized as the Z_2 topological invariant and the Chern number, C. The phase diagrams form the basis for understanding the TQPTs in Dirac materials.

Chapter 3

Theoretical Framework

This chapter presents the basic theoretical formulations necessary to find computational solutions to the electronic structure problem in a many-body system. The basic concept of density functional theory (DFT) is introduced as the primary theory employed in this thesis to calculate the physical properties from the ground state electron density. The tight-binding model for describing the properties of graphene and the transport phenomena in ballistic conductors is also described.

3.1 The many-body problem

CMP probes the fundamental properties of matter and their origins from the many-body interactions. However, the perspective is constantly changing with discoveries. Developing models that describe observed phenomena accurately while maintaining the capability to predict new properties is a fundamental challenge. One reliable way forward is to gain underpinning insights through efficient computations of the quantum many-body problem in model material systems. Thus, it is desirable for any such model to efficiently determine the optimized structure and physical properties from the ground-state electronic structure of many-body systems. Such materials range from single atoms to mesoscopic systems [111]. In 1926, Erwin Schrödinger derived his equation to define the quantum state of matter [112]. The Schrödinger equation became useful for enabling discussions of the relationship between the wavefunction and the total energy of a quantum system. The solutions of

the many electrons wavefunction required for the analysis of the electronic structure and properties of condensed matter phases via Schrödinger equation can be written as:

$$\hat{H}\psi(\boldsymbol{R},\boldsymbol{r},t) = E\psi(\boldsymbol{R},\boldsymbol{r},t), \tag{3.1}$$

where $\hat{H}$ denotes the Hamiltonian, E and $\psi(\boldsymbol{R},\boldsymbol{r},t)$ denote the total energy and the wave function of all electrons and nuclei, respectively. In this case, $\boldsymbol{R}$, and $\boldsymbol{r}$ denote the position vectors of nucleus and electrons, respectvely [113, 114].

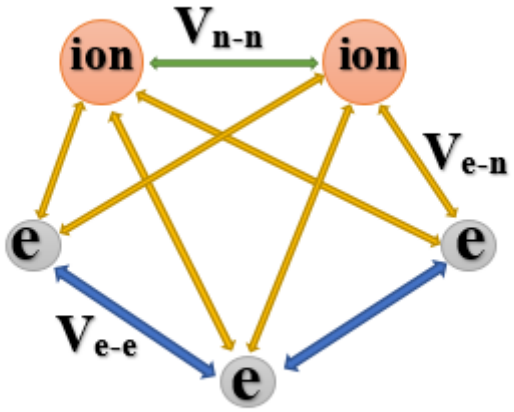

Figure 3.1: Schematic of the many-body interactions that must be solved in the electronic structure problem. This shows the interactions between nuclei-nuclei (V_{n-n}), electron-electron (V_{e-e}) and electron-nuclei (V_{e-n}).

Therefore, the Hamiltonian of N electrons that are interacting with one another, and with M nuclei [see Fig. 3.1] can be written as:

$$\begin{aligned}\hat{H} = &-\sum_{I=1}^{N}\frac{\hbar^2}{2M_I}\nabla_I^2 - \frac{\hbar^2}{2m_e}\sum_{i=1}^{N}\nabla_i^2 + \frac{1}{2}\sum_{I=1}^{M}\sum_{J\neq I}^{N}\frac{Z_I Z_J e^2}{|\boldsymbol{R}_I - \boldsymbol{R}_J|} + \frac{1}{2}\sum_{j\neq i}^{N}\sum_{i=1}^{N}\frac{e^2}{|\boldsymbol{r}_i - \boldsymbol{r}_j|} \\ &-\sum_{I=1}^{M}\sum_{i=1}^{N}\frac{Z_I e^2}{|\boldsymbol{R}_I - \boldsymbol{r}_i|},\end{aligned} \tag{3.2}$$

where I, i denote the set of nuclei and elctrons coordinates, respectively. However Z, M denote the charges and masses of nuclei, respectivly. Since $\hbar$, m and e are the basic constants [114–116]. Nevertheless, the Hamiltonian operator shown in

Equation (3.2) can be decomposed into five terms that correspond to contributions to the total energy:

$$\hat{H} = \hat{T}_n + \hat{V}_{n-n} + \hat{T}_e + \hat{V}_{e-n} + \hat{V}_{e-e}. \tag{3.3}$$

The Hamiltonian in Equation (3.3) is made up of contributions from the kinetic energy of nuclei $\hat{T}_n$ and electrons $\hat{T}_e$, the inter-nuclear repulsive potential nuclei $\hat{V}_{n-n}$ as well as the exchange potential between nuclei and electrons $\hat{V}_{e-n}$ as displayed in Fig. 3.1. The following expressions give the value of each of the contributions to the Hamiltonian:

$$\hat{T}_n = -\sum_{I=1}^{N} \frac{\hbar^2}{2M_I} \nabla_I^2, \tag{3.4}$$

$$\hat{T}_e = -\frac{\hbar^2}{2m_e} \sum_{i=1}^{N} \nabla_i^2, \tag{3.5}$$

$$\begin{aligned} \hat{V}_{n-n} &= \frac{1}{2} \sum_{I=1}^{M} \sum_{J \neq I}^{M} \frac{Z_I Z_J e^2}{|\boldsymbol{R}_I - \boldsymbol{R}_J|}, \\ \hat{V}_{e-n} &= -\sum_{I=1}^{M} \sum_{i=1}^{N} \frac{Z_i e^2}{|\boldsymbol{R}_I - \boldsymbol{r}_i|}, \\ \hat{V}_{e-e} &= \frac{1}{2} \sum_{j \neq i}^{N} \sum_{i=1}^{N} \frac{e^2}{|\boldsymbol{r}_i - \boldsymbol{r}_j|}. \end{aligned} \tag{3.6}$$

3.2 Born-Oppenheimer (BO) approximation

The solution of equation (3.1) for an interacting many-body system of particles would be a hassle and complex and needs an approximation [115, 116]. Thus, several approximations have been proposed to simplify the Schrödinger equation. Born and Oppenheimer proposed the first approximation to facilitate a solution through the implementation of a perturbative approach. It emerges from the large difference between mass of nuclei and electrons [117]. The main idea of this approximation is to decouple the wavefunction $\psi(\boldsymbol{R}_I, \boldsymbol{r}_i)$ into electrons $\psi_e(\boldsymbol{R}_I, \boldsymbol{r}_i)$ and nuclei $\psi_n(\boldsymbol{R}_I)$ such as:

$$\psi(\boldsymbol{R}_I, \boldsymbol{r}_i) = \psi_e(\boldsymbol{R}_I, \boldsymbol{r}_i)\psi_n(\boldsymbol{R}_I). \tag{3.7}$$

The Born-Oppenheimer (BO) approximation neglects the motion of the nuclei by considering them to be static. Using equation (3.1) and equation (3.7), the Hamiltonian for electrons and nuclei can be separated [111], and obtained independently as shown in the following equations:

$$\begin{aligned}\hat{H}_e\psi_e(\boldsymbol{R}_I,\boldsymbol{r}_i) &= \Big[\hat{T}_e + \hat{V}_{e-e} + \hat{V}_{e-n}\Big]\psi_e(\boldsymbol{R}_I,\boldsymbol{r}_i)\\ &= E_e\psi_e(\boldsymbol{R}_I,\boldsymbol{r}_i),\end{aligned} \tag{3.8}$$

and

$$\begin{aligned}\hat{H}_n\psi_n(\boldsymbol{R}_I) &= \Big[\hat{T}_n + \hat{V}_{n-n} + E_e\Big]\psi_n(\boldsymbol{R}_I)\\ &= E_n\psi_n(\boldsymbol{R}_I).\end{aligned} \tag{3.9}$$

The terms contained within the square bracket in the RHS of equations (3.8) and (3.9) denote the Hamiltonian of the electron and nuclei, respectively.

The nuclei wave function is obtained by solving the time-dependent Schrödinger equation of the form:

$$i\hbar\frac{\partial}{\partial t}\psi_q(\boldsymbol{R},t) = \Big[-\sum_{I=1}\frac{\hbar^2}{2M_I}\nabla_I^2 + V_{n-n}(\boldsymbol{R}) + \tilde{V}_q(\boldsymbol{R})\Big]\psi_q(\boldsymbol{R},t) \tag{3.10}$$

with

$$\tilde{V}_q(\boldsymbol{R}) = E_q(\boldsymbol{R}) + \sum_I \frac{\hbar^2}{2M_I}\left\langle\psi_q|\nabla_I^2|\psi_q\right\rangle. \tag{3.11}$$

The second term in the above equation describes the diagonal correction of the energy levels. Due to the coupling between electrons and nuclei degrees of freedom, the BO correction involves ignoring the diagonal term. Thus, for the nuclei system, the time-dependent Schrödinger equation can be written as:

$$i\hbar\frac{\partial}{\partial t}\psi_q(\boldsymbol{R},t) = \Big[-\sum_I\frac{\hbar^2}{2M_I}\nabla_I^2 + V_{n-n}(\boldsymbol{R}) + E_q(\boldsymbol{R})\Big]\psi_q(\boldsymbol{R},t). \tag{3.12}$$

The solution of the Schrodinger equation for the wave function of the many-body system is connected to Ehrenfest theorem [118]. This connection provides the mechanism for determining the average value of different operators. For instance, the expectation value of the rate of change of the position and momentum operators

are given in terms of their commutation relationships with the Hamiltonian in the following equations:

$$\frac{\mathrm{d}}{\mathrm{d}t}\langle \boldsymbol{R}\rangle = \frac{1}{i\hbar}\langle[\boldsymbol{R}, \hat{H}]\rangle + \langle\frac{\partial \boldsymbol{R}}{\partial t}\rangle = \frac{1}{M}\langle\hat{P}\rangle, \tag{3.13}$$

and

$$\frac{\mathrm{d}}{\mathrm{d}t}\langle \hat{\boldsymbol{p}}\rangle = \frac{1}{i\hbar}\langle[\hat{\boldsymbol{p}}, \hat{H}]\rangle + \langle\frac{\partial \hat{\boldsymbol{p}}}{\partial t}\rangle = \frac{1}{M}\langle-\nabla\hat{V}\rangle. \tag{3.14}$$

Incorporating equations (3.13) and (3.14) into Newtons equation of motion for the expectation value of the position $\langle \boldsymbol{R}\rangle$ leads to the force F on the electronic system, given by:

$$M\frac{\mathrm{d}^2}{\mathrm{d}t^2}\langle \boldsymbol{R}\rangle = \langle-\nabla\hat{V}\rangle. \tag{3.15}$$

By introduces the classical nuclei approximation to BO described in equation (3.12), one can find:

$$M\frac{\mathrm{d}^2}{\mathrm{d}t^2}\boldsymbol{R} = -\nabla\hat{V} = -\nabla\Big[V_{n-n}(\boldsymbol{R}) + E_q(\boldsymbol{R})\Big], \tag{3.16}$$

where $E_q(\boldsymbol{R})$ denotes potential energy surface (PES).

The change in electronic energy is connected to the Hellman-Feynman force theorem [119–121] for an external parameter of the Hamiltonian, generically denoted by λ. The expectation value of the total energy with respect to parameter λ is given as:

$$\frac{\partial E_q(\lambda)}{\partial\lambda} = \langle\psi_q(\boldsymbol{R})|\frac{\partial\hat{H}}{\partial\lambda}|\psi_q(\boldsymbol{R})\rangle\,. \tag{3.17}$$

The force on the I^{th} nuclei can be written as:

$$M\frac{\mathrm{d}^2}{\mathrm{d}t^2}\langle \boldsymbol{R}\rangle = -\langle\psi_q(\boldsymbol{R})|\frac{\partial\hat{H}}{\partial\boldsymbol{R}_I}|\psi_q(\boldsymbol{R})\rangle - \langle\frac{\partial V_{n-n}}{\partial\boldsymbol{R}}\rangle. \tag{3.18}$$

The numerical combination of the above equations to describe the dynamical evolution of the electronic structure of a many-body system is known as first-principles or ab-initio molecular dynamics [113, 115]. The solution to the stationary state problem can be used to determine the lowest energy (or ground state) of a system of atoms, and the optimum structure of a condensed matter system, by imposing the stationary condition, $M\frac{d^2}{dt^2}\boldsymbol{R} = 0$. At equilibrium, this condition corresponds to

a vanishing force, where,

$$\langle\psi_q(\boldsymbol{R})|\frac{\partial\hat{H}}{\partial\boldsymbol{R}_I}|\psi_q(\boldsymbol{R})\rangle + \langle\frac{\partial V_{n-n}}{\partial\boldsymbol{R}}\rangle = 0. \tag{3.19}$$

This procedure is known as geometry optimization [113].

3.3 The electron density function

Electron density represents the measure of the probability of finding an electron in a particular position around an atom. Broadly, an electron is more likely to exist in regions with high density. So the N-atom many electron wave function takes the form:

$$\psi(\boldsymbol{r}\sigma) = \psi(\boldsymbol{r}_1\sigma_1, \boldsymbol{r}_2\sigma_2, ..., \boldsymbol{r}_N\sigma_N), \tag{3.20}$$

where σ_i denotes the spin of the i^{th} electron. The wave function of complex system should be normalized [115, 122, 123]. In other words, normalizing the wave function. This means finding the proper form of ψ as:

$$\langle\psi|\psi\rangle = \sum_{\sigma_1...\sigma_N}\int d\boldsymbol{r}_1\int d\boldsymbol{r}_2...\int d\boldsymbol{r}_N|\psi(\boldsymbol{r}_1\sigma_1, \boldsymbol{r}_2\sigma_2, ..., \boldsymbol{r}_N\sigma_N)|^2 = 1. \tag{3.21}$$

That ensures that the probability that the particle is found somewhere in space equals 1. This is generally known as the normalization condition for the wavefunction [124, 125]. Also, one essential parameter for classifying particles is their spin or intrinsic angular momentum. For electrons, the wave function must be antisymmetric of interaction between two-electron labels i and j. Alternatively, is to build it for a system of similar particles to reflect the demand that particles are almost identical.

$$\psi(\boldsymbol{r}_1\sigma_1, ..., \boldsymbol{r}_i\sigma_i, ..., \boldsymbol{r}_j\sigma_j, ..., \boldsymbol{r}_N\sigma_N) = -\psi(\boldsymbol{r}_1\sigma_1, ..., \boldsymbol{r}_j\sigma_j, ..., \boldsymbol{r}_i\sigma_i, ..., \boldsymbol{r}_N\sigma_N). \tag{3.22}$$

The electron density $n_\sigma(\boldsymbol{r})$ of a specific state can be described as the number of

electrons N per unit volume in the position $\boldsymbol{r}$ for that status, therefore:

$$\sum_{\sigma} \int n_{\sigma}(\boldsymbol{r}) d\boldsymbol{r} = N. \tag{3.23}$$

According to the theory of quantum mechanics for a normalized wave function $|\psi\rangle$, the probability of finding electrons can be written as:

$$n(\boldsymbol{r}, \sigma) = N \sum_{\sigma_j = \sigma_2}^{\sigma_N} \int d\boldsymbol{r}_2 \int d\boldsymbol{r}_3 ... \int d\boldsymbol{r}_N |\psi(\boldsymbol{r}\sigma, \boldsymbol{r}_2\sigma_2, \boldsymbol{r}_3\sigma_3, ..., \boldsymbol{r}_N\sigma_N)|^2. \tag{3.24}$$

The corresponding operator $\hat{n}(\boldsymbol{r})$, which yields the electron density of spin state σ at point $\boldsymbol{r}$ can be written as:

$$\hat{n}(\boldsymbol{r}, \sigma) = \sum_{i=1}^{N} \delta(\boldsymbol{r}_i - \boldsymbol{r}) \delta(\sigma_i - \sigma). \tag{3.25}$$

3.4 Density functional theory (DFT)

The birth of density functional theory (DFT) from quantum mechanics is considered a pioneer work for solving many-body problems. DFT is utilized in physics, chemistry and materials science to calculate the electronic structure of many-body interacting systems like atoms, molecules and solids at the ground state (GS) level. It is dependent on two theorems devolped by Hohenberg and Kohn (HK) as well as Kohn and Sham (KS) [126, 127]. This section provides the DFT framework for calculating the total energy of the system. In addition to introducing the basic idea of some approximations used to find unknown functional.

3.4.1 The Hohenberg-Kohn theorems

Hohenberg and Kohn made a significant step toward modern density functional theory in 1964. They proved that the total energy construction for a system could be illustrated in electron density. This concept is connected to the previous proposals of the Thomas-Fermi model. Atoms were located in homogenous electron gas and simulated as a system under a positive potential [128, 129]. Here with HK theorem

includes two central parts as the following:

Theorem 1. "The external potential $V_{ext}(\boldsymbol{r})$ is a unique functional for $n(\boldsymbol{r})$, since, in turn $V_{ext}(\boldsymbol{r})$ reforms $\hat{H}$, in othor words the full many particle ground state GS is a unique functional of density $n(\boldsymbol{r})$" [122].

Although $V_{ext}(\boldsymbol{r})$ and $V'_{ext}(\boldsymbol{r})$ are disimilar potentials, however, they yield the same ground state GS density $n_0(\boldsymbol{r})$. Therefore from the principle of variation (cf. Ref. [114]), which obeys the following:

$$\begin{aligned} E_0 < & \langle \psi' | \hat{H} | \psi' \rangle \\ < & \langle \psi' | \hat{H}' | \psi' \rangle + < \langle \psi' | \hat{H} - \hat{H}' | \psi' \rangle \\ = & E'_0 + \int n_0(\boldsymbol{r})[V_{ext} - V'_{ext}] d\boldsymbol{r}, \end{aligned} \tag{3.26}$$

then

$$\begin{aligned} E'_0 < & \langle \psi | \hat{H}' | \psi \rangle \\ < & \langle \psi | \hat{H} | \psi \rangle + < \langle \psi | \hat{H}' - \hat{H} | \psi \rangle \\ = & E_0 - \int n_0(\boldsymbol{r})[V_{ext} - V'_{ext}] d\boldsymbol{r}. \end{aligned} \tag{3.27}$$

Nevertheless, incorporating above equations (3.26) and (3.27) shows obvious discrepancy as follow:

$$E_0 + E'_0 < E_0 + E'_0. \tag{3.28}$$

Theorem 2. "A global function $F_{HK}[n]$ for the energy $E[n]$, the functional that conveys the exact ground state energy of the system, conveys the lowest energy if the input density is the real ground density $E[n]$"[122]. Applying the Hamiltonian of electrons in equation (3.8), therefore the functional energy of Hohenberg-Kohn can be defined as:

$$\begin{aligned} E[n] = & \langle \psi[n] | \hat{H} | \psi[n] \rangle \\ = & \langle \psi[n] | \hat{T} + \hat{V_{e-e}} | \psi[n] \rangle + V_{ext}[n], \end{aligned} \tag{3.29}$$

and applying variational principle gives:

$$\begin{aligned} E[n] &< (F[n] + V_{ext}[n]) \\ &= F[n] + \int n(\boldsymbol{r}) V_{ext}(\boldsymbol{r}) d\boldsymbol{r} \\ &= E_0[n_0(\boldsymbol{r})]. \end{aligned} \tag{3.30}$$

Since the $(e-e)$ interaction and the operator of kinetic energy $\hat{T}$ are included as functional terms of density only. Consequently, $F[n]$ should be a global functional of the density and based only on the electron density,

$$F[n] = \langle \psi[n] | \hat{T} + \hat{V}_{e-e} | \psi[n] \rangle \,. \tag{3.31}$$

According to variational principle the driving of this functional obtains its minimum for the exact density $n(\boldsymbol{r})$ coinciding to $V_{ext}(\boldsymbol{r})$. Since of any density $n'(\boldsymbol{r})$ for particuler $V_{ext}(\boldsymbol{r})$ can get:

$$\begin{aligned} E[n'(\boldsymbol{r})] &< \langle \psi' | \hat{H} | \psi' \rangle \\ &= F[n'(\boldsymbol{r})] + \int V_{ext}(\boldsymbol{r}) n'(\boldsymbol{r}) d\boldsymbol{r} \\ &> \langle \psi | \hat{H} | \psi \rangle \\ &= E[n(\boldsymbol{r})]. \end{aligned} \tag{3.32}$$

Then the mathematical foundation of the DFT from a principle of Hohenberg and Kohn (HK) theorems is finding the F[n]. This is guarantee obtaining the solution for the whole Schrödinger wave equation of many-body [113, 122, 126, 130]. The external potential usually refers to the electron-nuclei interaction. Therefore, the ground-state can be determined via the electron density of a system instead of its complete many-body wavefunction.

3.4.2 The Kohn-Sham Method

A year later, from the reported HK theorems, KS proved a method that makes density functional theory workable. According to quantum physics and particu-

larly DFT, the difference between the two methods is Kohn-Sham technique treated many-electron as one-electron. Nevertheless, Schrödinger wave equation considered whole electrons. The formulation of DFT lends itself to finding good approximations to the actual ground state GS. Kohn and Sham suggested that the true ground state can be characterized by the density of the ground state of the reference system for non-interact particles. Also, the contribution of Hamiltonian is selected to contain an effective local potential $\upsilon_s(\boldsymbol{r})$ and the kinetic energy operator affecting on the electron [113, 115].

$$\hat{H} = \sum_i \Big(- \frac{\hbar^2}{2m_e} \nabla_i^2 + \upsilon_s(\boldsymbol{r}_i) \Big). \tag{3.33}$$

The GS electron density in a many-body system is obtainable by solving the time independent Schrodinger equation for a single-particle. This is given by:

$$\hat{H}\psi_i = E_i \psi_i. \tag{3.34}$$

This is equivalent to the expression:

$$\Big[- \frac{\hbar^2}{2m_e} \nabla^2_{(\boldsymbol{r})} + \upsilon_s(\boldsymbol{r}) \Big] \psi_i = E_i^{KS} \psi_i. \tag{3.35}$$

The total energy E_{KS} of the interacting system is defined as:

$$E_{KS} = T_s[n] + \int \upsilon_{ext}(\boldsymbol{r}) n(\boldsymbol{r}) d\boldsymbol{r} + E_H[n] + E_{xc}[n]. \tag{3.36}$$

The exchange-correlation energy (E_{xc}) is given by:

$$E_{xc}[n] = \langle \hat{T} \rangle - T_s[n] + \langle V_{int} \rangle - E_H[n]), \tag{3.37}$$

where $T_s[n]$ denotes the kinetic energy term for non-interacting particles. The contribution from $E_{xc}[n]$ to the total energy is not known in exact form. Hence, so it must be approximated. $E_H[n]$ denotes the Hartree energy [113, 115, 130]. Thus, all terms in the KS equation are written explicitly except $E_{xc}[n]$ [122]. By introducing the variational principle and considering the orbital ψ_i to be orthonormal

$\langle\psi|_i\,|\psi\rangle_j = \delta_{ij}$, the above KS equation can be expressed as:

$$\Big[-\frac{\hbar^2}{2m_e}\nabla^2_{(\boldsymbol{r})} + \int \frac{n(\boldsymbol{r}')}{|\boldsymbol{r}-\boldsymbol{r}'|}d\boldsymbol{r}' + \upsilon_{xc}[n] + \upsilon_{ext}(\boldsymbol{r})\Big]\psi_i(\boldsymbol{r}) = E_i^{KS}\psi_i(\boldsymbol{r}). \tag{3.38}$$

Alternatively, it can be expressed as:

$$\Big[-\frac{\hbar^2}{2m_e}\nabla^2_{(\boldsymbol{r})} + V_{KS}(\boldsymbol{r})\Big]\psi_i(\boldsymbol{r}) = E_i^{KS}\psi_i(\boldsymbol{r}), \tag{3.39}$$

where

$$V_{KS}(\boldsymbol{r}) = \int \frac{n(\boldsymbol{r}')}{|\boldsymbol{r}-\boldsymbol{r}'|}d\boldsymbol{r}' + \upsilon_{xc}[n] + \upsilon_{ext}(\boldsymbol{r}), \tag{3.40}$$

inculde XC potential υ_{xc} which is the functional derivative of the exchange energy $E_{xc}[n]$ with respect to the electron density $n(\boldsymbol{r})$ [115, 122, 130].

$$\upsilon_{xc}(\boldsymbol{r}) = \frac{\partial E_{xc}[n]}{\partial n(\boldsymbol{r})}. \tag{3.41}$$

The total energy at GS density of the many-body interacting particles is calculated exactly by solving the KS equation (3.39) through the self-consistent cycle. The calculation begins with a guess of an initial set of orbitals to use for calculating the electron density $n(\boldsymbol{r})$. This is followed by constructing the effective potential $V_{KS}(\boldsymbol{r})$ until a self-consistent cycle is achieved. In the last few decades, the KS formalism of DFT is the most prominent method used to calculate the exact electronic GS of a many-body solid [130]. The practical implementation of DFT calculations requires a transformation of the problem of the electronic structure theory formulated above into an equivalent computational problem.

The aim of the computational task is to determine the XC functional that accurately approximates the exchange-correlation energy contribution $E_{xc}[n]$ to the total energy. This is based on the variational principles for obtaining the XC functional dependence of the unknown part of the system's total energy. Since the exact analytical form of the XC energy $E_{xc}(\boldsymbol{r})$ is unknown, it must be approximated [115]. The approximations for E_{xc} are made in the form of XC functional. The simplest approximations are the semi-local exchange-correlation functionals because they are

only dependent locally on the electronic charge density $\rho(\boldsymbol{r})$ and its gradient $\boldsymbol{\nabla}\rho(\boldsymbol{r})$. The most basic functional is the local density approximation (LDA), where $E_{xc}(\boldsymbol{r})$ is approximated point by point in real space by the exchange-correlation energy of the homogeneous electron gas of density $\rho(\boldsymbol{r})$. The first careful step in DFT calculations is functionalizing the XC energy with an accurate approximation. There are several XC functionals available for use in DFT calculations. This ranges from local functionals such as local density approximation (LDA), the generalized gradient approximation (GGA) to hybrid functionals such as the Heyd-Scuseria-Ernzerhof functional (HSE06), etc. [131–136].

3.5 *Ab initio* modeling of materials

3.5.1 Bloch's theorem and plane wave basis

The infinite number of electrons in a condensed matter system makes the Schrödinger equation for many particles quite complex to solve. However, in 1928 Felix Bloch invented the theory that allows the electrons in the unit cell to be described using the Schrödinger equation [137, 138]. The theory states that the electronic wave function ψ in the periodic potential can be defined as a product of the plane wave (PW) and the function of lattice periodicity as written below [139]:

$$\psi_{\boldsymbol{k}}(\boldsymbol{r}) = e^{i\boldsymbol{k}.\boldsymbol{r}} u_{\boldsymbol{k}}(\boldsymbol{r}) \tag{3.42}$$

where $\boldsymbol{k}$ denotes the wave vector in the first BZ, $\boldsymbol{r}$ denotes the position vector of periodicity. The function $u_{\boldsymbol{k}}(\boldsymbol{r})$ is the periodic lattice function, which is constant under translation.

$$u_{\boldsymbol{k}}(\boldsymbol{r} + \boldsymbol{R}) = u_{\boldsymbol{k}}(\boldsymbol{r}), \tag{3.43}$$

where $\boldsymbol{R}$ denotes the transilation vector.

Using Fourier series, the periodic function $u_{\boldsymbol{k}}(\boldsymbol{r})$ can be written as:

$$u_{\boldsymbol{k}}(\boldsymbol{r}) = \sum_{\boldsymbol{G}} c_{\boldsymbol{G},\boldsymbol{K}} e^{i\boldsymbol{G}.\boldsymbol{r}}, \tag{3.44}$$

where $\boldsymbol{G}$ denotes the reciprocal vector defined by:

$$\boldsymbol{G}.\boldsymbol{b} = 2\pi m. \tag{3.45}$$

Here, $\boldsymbol{b}$ denotes the translation vector in the crystal lattice, and m is an arbitrary constant. So, the Kohn-Sham orbitals expressed as:

$$\psi_{\boldsymbol{k}}(\boldsymbol{r}) = \sum_{\boldsymbol{K},\boldsymbol{G}} c_{\boldsymbol{K},\boldsymbol{G}} e^{i(\boldsymbol{K}+\boldsymbol{G}).\boldsymbol{r}}. \tag{3.46}$$

Substituting the plane waves shown in (3.46) into K-S equation (3.39) yields the secular equation below:

$$\sum_{\boldsymbol{G}} \left[\frac{\hbar}{2m}|\boldsymbol{K}+\boldsymbol{G}|\delta_{\boldsymbol{G}\boldsymbol{G}'} + V_{KS}^{\sigma}(\boldsymbol{G}-\boldsymbol{G}')\right] c_{i,\boldsymbol{K}+\boldsymbol{G}'} = E_i c_{i,\boldsymbol{K}+\boldsymbol{G}'}, \tag{3.47}$$

where $V_{KS}^{\sigma}(\boldsymbol{G}-\boldsymbol{G}')$ describes the Fourier transform of the Kohn-Sham barrier. A criterion for a finite number of $\boldsymbol{G}$-vectors can be defined by an energy cut-off E_{cut}. This determines the vectors $\boldsymbol{G}$ that are accounted for in the Fourier expansion and the accuracy of the computation is determined by fixing the PW cut-off energy:

$$\frac{1}{2}\left|\boldsymbol{K}+\boldsymbol{G}\right|^2 < E_{cut}. \tag{3.48}$$

The choice of number of PWs to be used in a DFT calculation is determined by the Bloch wave vector $\boldsymbol{K}$. If $\boldsymbol{K}$ is known, the solution of the many-body quantum state of the electron is numerically set within the proper plane wave basis. In equation (3.48), the cut-off energy sets a limit for the maximum length of the $\boldsymbol{G}$ vectors leading to a finite matrix representation for the Hamiltonian. This truncation of the expansion in a plane waves basis makes the kinetic energy term to be less than the cut-off energy. This difference in energy representation can introduce errors in the total energy of some systems. In practical calculations, this error is reduced by increasing the cut-off energy.

3.5.2 Reciprocal space and Brillouin zone (BZ)

The significance of the BZ stems from the representation of waves in the periodic medium. Felix Bloch showed that solutions of the electron state on a periodic lattice can be characterized by the behavior plane waves in the BZ [137]. Once the eigenvalues of the Kohn-Sham equation are calculated, it is straightforward to determine the total energy of the many-body system. Such eigenvalues are obtained self-consistently from the k-dependence of the Hamiltonian. The first Brillouin zone can be sampled by mapping out a continuous set of points in reciprocal ($\boldsymbol{k}$) space. These Brillouin zone points are represented by k-points. Integration over the Brillion Zone are necessary to compute that total energy within the DFT framework. An integration over the first Brillouin zone must be converted into a summation over discrete points in k-space. For instance, the calculation of the density for points of the BZ takes the following form:

$$n(\boldsymbol{r}) = \sum \int_{BZ} F(\boldsymbol{k}) d^3\boldsymbol{k}, \tag{3.49}$$

where $F(\boldsymbol{k})$ denotes the periodic function. Hence, in the case of a periodic system, the integral must be approximated, by a sum over a discrete number of k-points. Such k-points denote the points in the first Brillouin zone at which the DFT calculations are performed to determine the electronic state in a solid system. This implies that the set of K-points to use in a DFT calculation must be chosen carefully to improve numerical accuracy of the calculation and in a way that reduces computational workload.

In practice, making use of a dense k-point grid reduces errors in the self-consistency calculations. The tetrahedra method [140, 141] is considered the most effective method for integrating over the BZ. It splits the volume of the BZ into non-overlapping small tetrahedra. The easy integration technique is to sample the BZ with a limited k grid, such as a Monkhort-Pack mesh [142]. This gives a uniform grid of points in the BZ for DFT calculations and is considered an unbiased way of selecting a set of k-points for sampling the BZ. In addition, providing a sets of irre-

ducible points in the BZ provides an effective tool for integrating periodic functions. Therefore, with a better (or dense) k-point grid, the accuracy of the discrete sum in equation (3.49) approaches the integral. Nevertheless, for some properties, the size of the k-point grid needed to gain good convergence can become quite large.

3.6 Pseudopotentials

The success of the nearly free electron (NFE) approximation in describing simple metals confirmed that the combined presence of strong and localized quantum objects such as core shells and nuclear potentials creates an effectively weak periodic perturbation in a many-body solid. This is equivalent to a lattice of smooth ionic potentials which slightly repel the valence electrons from the immediate vicinity of the nuclei. Phillips and Kleinman [143] first showed that the requirement of orthogonality of the valence states to the inner core states pushes the outermost maximum of the valence wave functions away from the core region.

Inside the core region, the orthogonality requirement acts like a repulsive potential which tends to cancel the attractive nuclear potential felt by the valence electrons. As such, their combined effect can be well approximated by a relatively weak repulsive potential, or pseudopotential (PP). The valence electron wavefunctions are smoothened and need fewer plane waves in their expansion. In the DFT technique, a pseudopotential or effective potential is used to provide an approximate. In solid systems, the external valence electrons dominate most system properties. Such as electric and magnetic rather than core shell electrons [144, 145]. So PP replaces the core electrons and the strong potential between ions with a slight pseudopotential. This approximation simplifies the calculations because it treats the ions as frozen in their atomic arrangement [145].

The primary application in electronic structure problem is to replace the strong Coulomb potential of the nucleus and the effects of the tightly bound core electrons by a PP. This denotes an effective ionic potential that acts on the valence electrons. This concept is crucial for the plane-wave method of calculating the total energy since the alternative full Coulomb potential of the electron-ion interaction decays

too slowly to be accurately represented by a small number of Fourier components. The PP method has been developed as an extension of the orthogonalized plane waves (OPW) method. The OPW method was introduced by Convers Herring in 1940 [146] to construct valence electron states that are orthogonal to the core electron states using plane waves as the basis. An OPW function is constructed by orthogonalizing the wave-function with respect to the core states. In this case, the orthogonality of the OPW state is guaranteed by hermiticity of the electron state projection operator, P. This makes the projected electron states to satisfy the conditions satisfied by proper eigenstates of the Hamiltonian.

The PP approximation is based on an ansatz which separates the total wave function into an oscillatory (or all-electron) part denoted by $\Psi_{All-electron}$ and a smooth part, denoted by the so-called pseudo wave function, Ψ_{Pseudo}. In practice, this method treats the core electron states as known functions. Generally, the functions are taken from tight-binding calculations that are performed using atomic orbitals. This has the advantage of reducing the time required for the total energy to converge. Figure 3.2 shows a schematic representation of the PP method. The electrons are partitioned into the core and valence regions by the cut-off radius. The pseudo wavefunction (Ψ_{Pseudo}) does not oscillate as much as the all-electron wavefunction ($\Psi_{All-electron}$) in the core region. This means that far fewer plane waves to describe compared to the all-electron wavefunction. Ψ_{Pseudo} applies to a large number of systems because it is a smooth function. In the valence region, Ψ_{Pseudo} matches with $\Psi_{All-electron}$ while the potential V_{Pseudo} also matches the all-electron potential $V_{All-electron}$.

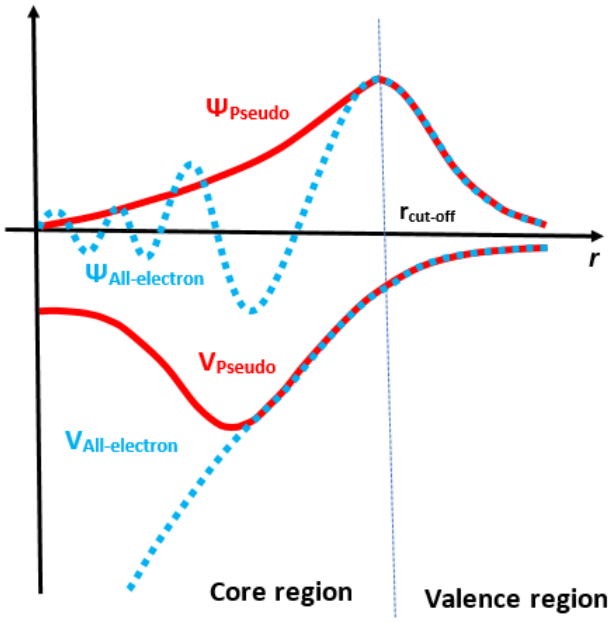

Figure 3.2: Schematic description of the pseudopotential method. The dashed blue line above (or below) the horizontal r-axis denotes the all-electron wavefunction (or the all-electron potential), and the solid red lines above (or below) the horizontal r-axis represents the pseudo wavefunction (or the pseudo potential). The strong all-electron potential, and the weak pseudopotential are also shown in corresponding lines and colors.

There are several approaches to the generation of PPs. However, the starting point for generating norm-conserving potentials is given by Hamann, Schluter, and Chiang [147] in the following requirements:

1. All-electron and pseudo valence eigenvalues must agree for the chosen atomic reference configuration.

2. All-electron and pseudo valence wavefunctions ($\Psi_{All-electron}$ and Ψ_{Pseudo}) must be matched beyond a chosen core radius $r_{cut-off}$.

3. The logarithmic derivatives of the all-electron and pseudo wavefunctions agree at $r_{cut-off}$.

4. The integrated charge density inside the core region $r_{cut-off}$ for each wavefunction must agree. This is known as the norm-conservation condition.

5. The first energy derivative of the logarithmic derivatives of the all-electron and pseudo wavefunctions must agree at $r_{cut-off}$, and therefore for all $r \geq r_{cut-off}$.

As indicated in Figure 3.2, one of the key constraints is that the requirement that a PP should coincide with the actual potential of the system outside the core region. This constraint is guaranteed by Requirements 1 and 2. The smoothness requirement on the pseudo wavefunction is guaranteed in Requirements 3. The norm conservation condition in Requirements 4 ensures that the core electron region has the correct charge density. Requirements 5 ensures that the PP will provide adequate description of the given ion in a quantum system. However, suppose that the wavefunction obtained with the PP differs from the actual one in the core region. This means that their respective charges will be distributed differently among the core and valence regions, resulting in their norms being different. This charge difference is called orthogonality hole [148], and should be corrected. Apart from the fact that the PP model is a separate area of research in electronic structure theory, addressing the orthogonality hole problem is complicated and will not be considered in this thesis.

3.6.1 The projector augmented-wave (PAW) method

There are different types of PPs in the literature. These range from the norm-conserving ones where Ψ_{Pseudo} and $\Psi_{All-electron}$ are identical outside the cut-off radius and their eigenvalues agree for the chosen atomic reference configuration to the ultrasoft one which relaxes the norm-conservation condition to allow calculations to be performed with the lowest possible cut-off energy for the plane-wave basis set. Nevertheless, to allow for more efficient computations of the electronic structure within DFT, the PP method and the linear augmented PW methods have been generalized in the projector augmented wave (PAW) method [149–151].

The PAW method allows for a significant reduction in the number of wave functions that must be calculated. This is because the pseudo potentials only must be calculated and tabulated once for each type. As discussed by Richard Martin in [152], the PAW method is a general approach to solution of the electronic structure problem that reformulates the OPW method by adapting it to modern techniques for calculation of total energy, forces, and stress within DFT. Just as in the $ultrasoft$

PP method [153], the PAW formalism introduces projectors and auxiliary localized functions. The PAW approach also defines a functional for the total energy that involves auxiliary functions, and it uses advances in algorithms for more efficient solution of the generalized eigenvalue problem in a many-body system. The main difference is that the PAW method keeps the full all-electron wavefunction in a form that is like the general OPW formalism because the full wavefunction varies rapidly near the nucleus. All integrals are evaluated as a combination of integrals of smooth functions extending throughout space plus localized contributions evaluated by radial integration over muffin-tin spheres, as in the augmented plane wave (APW) method.

The wavefunction of all-electron (AE) in the PAW approach is transformed from pseudo wavefunctions $|\psi_n^\alpha\rangle$. By employing the linear map operator τ [154], it could be written as:

$$|\psi_n^\alpha\rangle = \tau|\overset{\sim}{\psi}^\alpha\rangle = |\overset{\sim}{\psi}^\alpha\rangle + \sum_i (|\phi_i\rangle - |\overset{\sim}{\phi}_i\rangle)\langle\tilde{p}_i|\overset{\sim}{\psi}_n^\alpha\rangle, \tag{3.50}$$

where $|\overset{\sim}{\psi}_n^\alpha\rangle$ denotes the variational pseudo wave-function. $|\phi_i\rangle$ and $|\overset{\sim}{\phi}_i\rangle$ represent the partial pseudo and all electron (AE) wavefunctions. The index i denotes the sites of ions [154] since the valence electrons can only experience the screened Coulomb potential due to the core electrons. A basis set of plane waves for the valence electron wavefunctions can be built from the atomic wavefunctions. However, when it is used to perform an AE calculation, the core electron states will also be included. Inclusion of core-states result in time-consuming calculations. When the calculations are performed using the PAW basis functions, a much lower cut-off energy is required leading to faster AE calculations. These make the PAW scheme a popular approach for practical DFT calculations in CMP.

3.6.2 Spin-orbit coupling (SOC)

In quantum physics, the relativistic interaction between the spin and angular momentum of an electron is known as spin-orbit coupling (SOC). As discussed exten-

sively by Taylor, et al [155], it is important to consider the fundamental question of when it constitutes a valid approximation to ignore relativistic effects when the electronic band structure of a solid is calculated within DFT. Consider that the Fermi energy of a metal, i.e., given by the energy difference between the lowest and highest filled conduction band state, is of the order of a few electron volts. This energy is far smaller than the rest-mass energy of the electron by about 1×10^{-5}, it may appear physically intuitive to always neglect such effects. However, it is crucial to note that the potential wells are very deep near the nuclei of heavy atoms, and that a small change in energy can cause significant qualitative differences in the electronic band structure in an insulating material (e.g., a semiconductor) whose energy band gap is small.

Thus, it is physically intuitive to start the consideration of the effects of the SOC on the electronic band structure within the Dirac theory of the relativistic electron [20]. This is because the Dirac equation,

$$\left(\beta mc^2 + c\sum_{n=1}^{3} \alpha_n p_n\right) \psi(x,t) = i\hbar \tfrac{\partial \psi(x,t)}{\partial t}, \tag{3.51}$$

which describes the motion of a relativistic electron in terms of a four-component wavefunction, also obeys Bloch's theorem. Thus, a wave number K can be associated with each electron state. This makes it possible to recast the OPW method in terms of an orthogonalization of the four component plane waves to the four-component tight-binding core states. The Dirac equation also has the periodicity of the lattice, just like Schrodinger equation. In the non-relativistic limit, the electron and positron parts of the Dirac equation can be separated by means of the Foldy-Wouthuysen transformation (F-W) [156, 157] to give an expression that is analogous to Equation (3.1). The F-W transformation gives a two-component wavefunction that describes only the electron. The most important terms contained in the Hamiltonian after the F-W reduction of the Dirac equation are given by

$$\begin{aligned} H = \frac{1}{2m}\left(\mathbf{p} - \frac{e}{c}\mathbf{A}\right)^2 - \frac{1}{8m^3c^2}\mathbf{p}^2 + V(\boldsymbol{r}) - \frac{e}{mc}\mathbf{S}.\boldsymbol{\nabla} \times \mathbf{A} \\ + \frac{1}{2m^2c^2}\mathbf{S}.\left[\boldsymbol{\nabla}V(\boldsymbol{r}) \times \left(\mathbf{p} - \frac{e}{c}\mathbf{A}\right)\right] + \frac{\hbar^2}{8m^3c^2}\boldsymbol{\nabla}^2 V. \end{aligned} \tag{3.52}$$

This reduced Hamiltonian contains a correction to the electronic kinetic energy because of a symmetry-breaking field denoted by the vector potential $\mathbf{A}$ and two additional terms that involve the spin angular momentum $\mathbf{S}$. However, since relativistic effects usually contribute a small amount to the total energy of a Bloch electron, it is often possible to treat them as a perturbation of the nonrelativistic band structure. The fact that the electron wavefunction has two components is consistent with the electron possessing a degree of freedom corresponding to a spin angular momentum $\mathbf{S} = \pm 1/2\hbar$ which can point either up or down.

In the following, current understanding of the dynamics of a relativistic electron is summarized from the viewpoint of quantum field theory. Firstly, the negative-energy states that were encountered by Dirac is not because of time reversal symmetry but because of the negative solutions of the Dirac equation. Dirac assumed erroneously that matter is stable because all (or almost all) the negative-energy states are filled. Secondly, Dirac's interpretation of antimatter is untenable in today's high-energy physics. This is partly because it is now well-known that there are charged elementary bosons like the $W+$ with a distinct antiparticle, the $W-$, and the Pauli's exclusion principle does not apply to bosons. As noted by Steven Weinberg [158], the current understanding is that the solutions of the Dirac equations are not a relativistic generalization of probability amplitudes like the Schrödinger wavefunction, as Dirac had thought. Instead, the positive-energy solutions are matrix elements $(\psi_0, \psi_x\psi_1)$ of the quantized electron field ψ_x between various one-electron statesψ_1 and the vacuum ψ_0, while the negative-energy solutions are matrix elements $(\mathrm{C}\psi_0, \psi_x\psi_1)$ of the electron field between the vacuum and various positron states. These current understanding have important implications on the dynamics of relativistic electrons in Dirac materials.

In Section 3.9, the modified Hamiltonian in Equation (3.52) is used as the theoretical basis for exploring the emergence of topological quantum phases of free electrons in Dirac materials. By applying a time-dependent vector potential as the absorption kick to the 0 K, electronic structure topological phase diagrams are obtained. Signatures of near-field electrodynamics are also investigated using

TDDFT to unravel a collective transport phase that behaves like a quantum-fluid.

The non-relativistic formulation of the KS method discussed in Section 3.4.2 relies on the Hamiltonian given in equation (3.8). This Hamiltonian does not include SOC [159]. In an interacting many-body system the SOC Hamiltonian $\hat{H}_{SO}$ is given by [160]:

$$\hat{H}_{SO} = \frac{e\hbar}{4m^2c^2}\hat{\boldsymbol{\sigma}}.\Big[\mathbf{E}(\boldsymbol{r}) \times \hat{\mathbf{p}}\Big], \tag{3.53}$$

where $\hat{\boldsymbol{\sigma}}$ is the Pauli spin matrices, and $\mathbf{E}(\boldsymbol{r})$ denotes electric field at the position $\boldsymbol{r}$ of electron. $\hat{\mathbf{p}}$ denotes the momentum operator. However, the potential of electrons can be written as:

$$\mathbf{E}(\boldsymbol{r}) = \frac{1}{2m^2c^2}\frac{1}{r}\frac{dV}{dr}. \tag{3.54}$$

To include the spin-orbital effect within Hamiltonian of many-body system, equation (3.8) is re-written as:

$$\hat{H}_e = \hat{T} + \hat{V}_{e-e} + \hat{V}_{e-n} + \hat{H}_{SO}. \tag{3.55}$$

In practical calculations, the SOC is included self-consistently by using relativistic pseudo-potentials. In this case the SOC is treated as a first-order perturbation of the spin state using relativistic PAW potentials. SOC lifts Kramers degeneracies by splitting electron states that are degenerate when it is not included. Further relaxation of the structure due to the inclusion of SOC is ignored in the calculations presented here.

The inclusion of SOC in DFT calculations is important for gaining insights into magnetism and emergent spin signatures [160]. The role of SOC in breaking of time-reversal and orbital symmetries are significant factors in the emergence of topological quantum phases of the electron and their associated phase transitions. It is shown in the results section, how SOC can change the transport character from the energy dispersion spectrum, especially around the Fermi level. In addition, it causes emergent phenomena such as anisotropy in magnetism, magnetic damping [161, 162], relaxation of spin [163], and exotic anomalous Hall effect [164].

3.7 Tight binding approximation

In the following analyses, the dynamics of the nuclei is neglected. Dynamics of the electronic degrees of freedom are completely decoupled from ionic dynamics. This approximation is valid since the electron are moving faster than the more massive ions. The resulting adiabatic dynamics is consistent with the BO approximation. To apply the Schrödinger picture to the wave dynamics of charge (or spin) carriers in a Dirac material, it is important to note that the Hamiltonian of the electronic system is analogous to equation (3.13). The electronic Hamiltonian will generate the time evolution of the quantum state of the electrons. Given the state function of the electronic system at an initial time $t = 0$, then the unitary time evolution of the quantum state at time t is

$$\psi(\widetilde{\boldsymbol{r}}, t) = U(t)\psi(0), \tag{3.56}$$

where

$$U(t) = e^{-i\hat{H}t/\hbar} \tag{3.57}$$

if the Hamiltonian does not depend on time.

However, to study the nonadiabatic dynamics of an electronic system using a time-dependent Hamiltonian, the tight binding model of graphene is introduced in the following. This is a necessary first step for understanding time dependent DFT in the tight binding approximation using the linear combination of atomic like orbitals. This allows for insights into the full-dimensional dynamics of molecules, clusters and macroscopic solids that include any type of couplings in the adiabatic regime. Examples of the couplings, which serve as ground state symmetry-breaking fields, include spin-orbit coupling, magnetic field, electric field, and electromagnetic fields, such as the coupling of monochromatic light (e.g., a laser field) to the magnetic (or electric) dipole moment in materials.

The tight-binding (TB) model allows more effective systems to be treated, with thousand of atoms in the lattice as a semi-empirical method. The central idea of the

TB model was formulated by Slater and Koster [165] based on the postulation that the basis set of eigenstates for a complex system is atomic-like and hence localized. In the computational modeling of materials, the TB (or the linear combination of atomic orbitals (LCAO)) method can be use in calculating electronic band structure and Bloch state of the electrons just as with *ab initio* calculations performed within DFT. However, the TB model requires fitting the parameters of the electronic structure to available experimental data on relevant physical properties of the material under consideration, or fitting them to results of accurate *ab initio* calculations when no reliable experimental data exist. For this reason, the set of parameters generated from the tight binding model of given a material are not transferable to other materials.

Nevertheless, the TB model is easy to generate for materials whose bonding electron states are dominated by the hybridization between valence electrons that are located in the s and p orbitals. Tight binding calculations are far easier to perform compared to ab initio calculations when implemented in the two-centre approximation to the multicentered integrals that appear in the Hartree-Fock theory of solids [166]. This is because only nearest neighbor hopping terms are considered. The consequence is that the computation of the electronic structure is done faster, but at the expense of the accuracy of valence orbital ranges and chemical bond lengths.

3.8 The tight binding model of graphene

Graphene is the single-atom thick two-dimensional plane of graphite. The carbon atoms are arranged in a hexagonal lattice or honeycomb structure as shown in Figure 3.3. each carbon atom is bonded strongly to three other carbons in the plane of the monolayer. Its strong σ-bonds arise from s-p hybridization and the C-C bonds show no ionicity. The unit cell of the graphene lattice can be described in terms of two inter-penetrating triangular sublattices. Thus, modelling of the nearest neighbour hopping of an electron from the reference carbon in terms of parameter t ignores the contribution from the intra-sublattice hopping that would have been expected from

the two sublattices. Thus, only one nonzero matrix element t, is used in to describe the nearest-neighbor hopping [167].

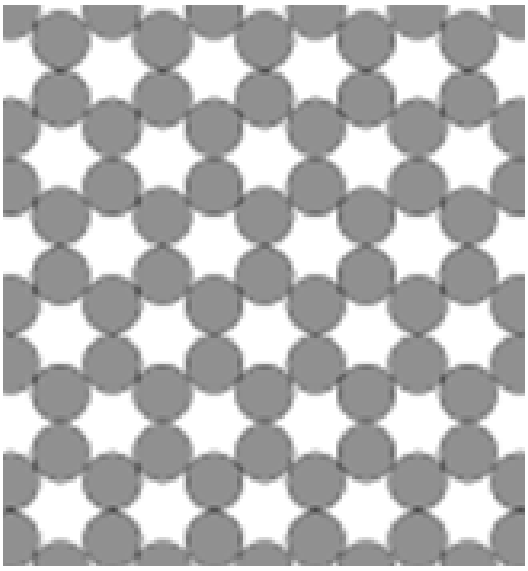

Figure 3.3: The hexagonal (honeycomb) lattice of graphene.

Generally, the TB model Hamiltonian of the honeycomb lattice can be written as [168]:

$$\hat{H} = -t \sum_{\langle i,j \rangle} \left[\hat{a_i^\dagger} \hat{b_j} + \hat{b_j^\dagger} \hat{a_i} \right], \tag{3.58}$$

where t denotes the hopping amplitude. For graphene, $t \simeq 2.7$ eV [169]. This parameter corresponds to the matrix element of the kinetic energy operator. The terms in the angle bracket $\langle i, j \rangle$ denotes the nearest neighbors hopping between sub-lattice sites A and B, while, $\hat{a}_i^\dagger(\hat{a}_i)$ denotes the corresponding operator for creation(annihilation), respectively. The sum over nearest neighbors given by:

$$\sum_{\langle i,j \rangle} \left[\hat{a_i^\dagger} \hat{b_j} + \hat{b_j^\dagger} \hat{a_i} \right] = \sum_{i \in A} \sum_{\boldsymbol{\delta}} \left[\hat{a_i^\dagger} \hat{b_{i+\boldsymbol{\delta}}} + \hat{b_{i+\boldsymbol{\delta}}^\dagger} \hat{a_i} \right], \tag{3.59}$$

where δ denotes position vectors of the nearest neighbors which is given by δ_1, δ_2, and δ_3. The summation over all the vectors δ combined the TB Hamiltonian of graphene in (3.58) given by:

$$\hat{H} = \frac{-t}{N/2} \sum_{i \in A} \sum_{\boldsymbol{\delta},k,k'} \left[e^{i(\boldsymbol{k}-\boldsymbol{k'}).\boldsymbol{r}_i} e^{-i\boldsymbol{k'}.\boldsymbol{\delta}} \hat{a_{\boldsymbol{k}}^\dagger} \hat{b_{\boldsymbol{k'}}} + H.c. \right], \tag{3.60}$$

where $N/2$ defines the number of sublattice sites A. The Hamiltonian can take the form:

$$\hat{H} = \sum_{\boldsymbol{k}} \boldsymbol{\psi}^{\dagger} h(k) \psi, \tag{3.61}$$

where the Hamiltonian is expressed in terms of the nearest neighbor hopping parameter t, in unit of energy, as a matrix with its elements given as shown in the following equations:

$$\boldsymbol{\psi} \equiv \begin{pmatrix} \hat{a}_{\boldsymbol{k}} \\ \hat{b}_{\boldsymbol{k}} \end{pmatrix}, \tag{3.62}$$

$$\boldsymbol{\psi}^{\dagger} = \begin{pmatrix} \hat{a}_{\boldsymbol{k}} & \hat{b}_{\boldsymbol{k}} \end{pmatrix}, \tag{3.63}$$

and

$$h(k) \equiv -t \begin{pmatrix} 0 & \triangle_{\boldsymbol{k}} \\ \triangle^{*}_{\boldsymbol{k}} & 0 \end{pmatrix}, \tag{3.64}$$

where

$$\triangle_{\boldsymbol{k}} \equiv \sum_{\boldsymbol{\delta}} e^{i\boldsymbol{k}.\boldsymbol{\delta}} [168]. \tag{3.65}$$

The eigenvalues of the above matrix representation are $\varepsilon_{\pm} = \pm t\sqrt{\triangle_{\boldsymbol{k}} \triangle^{*}_{\boldsymbol{k}}}$, and can be computed by re-writing $\triangle_{\boldsymbol{k}}$ in the form:

$$\triangle_{\boldsymbol{k}} = e^{i\boldsymbol{k}.\boldsymbol{\delta_1}} + e^{i\boldsymbol{k}.\boldsymbol{\delta_2}} + e^{i\boldsymbol{k}.\boldsymbol{\delta_3}}. \tag{3.66}$$

The energy levels are expressed as:

$$\varepsilon_{\pm}(\boldsymbol{k}) = \pm t \sqrt{1 + 4\cos\left(\frac{3}{2}k_x a\right)\cos\left(\frac{\sqrt{3}}{2}\right) + 4\cos^2(\frac{\sqrt{3}}{2}k_y a)}. \tag{3.67}$$

Alternatively, equation (3.67) can be expressed as:

$$\varepsilon_{\pm}(\boldsymbol{k}) = \pm t\sqrt{3 + f(\boldsymbol{k})}, \tag{3.68}$$

where

$$f(\boldsymbol{k}) = 2\cos\left(\sqrt{3}k_y a\right) + 4\cos\left(\frac{3}{2}k_x a\right)\cos\left(\frac{\sqrt{3}}{2}k_y a\right). \tag{3.69}$$

Figure (3.4) shows the energy-momentum dispersion relation for electrons in graphene as predicted in the nearest-neighbour TB model. Here, the conduction and valence bands touch at the Fermi level ($E = 0$ eV) at the time-reversal symmetric points K and K′ in the first Brillouin zone. The electronic ground state in graphene, when determined from first principles calculation with DFT can be used to benchmark the TB model when there are not external applied fields. Insofar as the semimetallic band structure is correctly reproduced in both approaches, the transport character in both model calculations support the ballistic transport of electrons. Herein, the ground state electronic structure in bulk tantalum arsenide (TaAs) is determined and combined with external field-dependent tight-binding calculations of the low-energy band dispersion in graphene to study the emergence of topologically ordered quantum states in the carrier transport model in Dirac materials. This allows the study evolution of graphene band structure with changes in the topological order parameters is employed here to study the dependence of the magnitude of the emergent bandgap on-field tuning parameters.

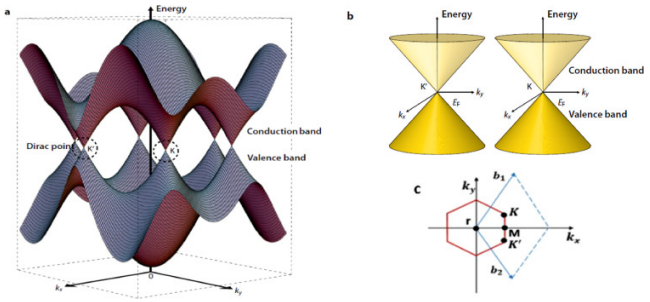

Figure 3.4: The energy-momentum dispersion relation of nearest-neighbor for graphene. (a) Zero energy states, and (b) the bands touch each other at the Dirac points. (c) Graphene Brillouin Zone [7].

3.9 Time dependent DFT in the LCAO basis

Time-dependent density-functional theory (TDDFT) is based on the linear response formalism used to compute the excited states of electronic systems. It describes the electronic properties and dynamics of a many-body system in the presence of time-dependent potentials. Examples of such potentials include the electric, magnetic, or electromagnetic field. The first derivation for TDDFT was presented in 1984

by Runge and Gross [170] for describing time-dependent systems. In the linear-response regime, a good choice for time dependent DFT calculations is the real-time (RT) propagation (TDDFT). The RT-TDDFT method uses the same ground state electron density as input information, just as the LR-TDDFT for computing response functions for perturbations of short duration. It incorporates nonlinear spectral information for long initial perturbations. Also, in RT-TDDFT, the TDKS wavefunction is propagated in time by integrating the TDKS equations numerically [171]. Therefore, by dealing with the electronic structure as an independent quantum system whose perturbed Hamiltonian depends on time, all relevant details about the physics of the system are included in its time expansion operator matrix elements.

The RT-TDDFT calculations performed in this study are based on the numerical implementations of the localized atomic basis set of the projector augmented wave (PAW) method in the grid-based projector augmented waves GPAW code [172, 173]. In the LCAO-based DFT implementation [174], the Kohn-Sham pseudo wave functions

$$\psi(\boldsymbol{r}) = \sum_{\boldsymbol{\mu}} \widetilde{\phi}(\boldsymbol{r}) c_{\mu n}, \tag{3.70}$$

are expanded onto a set of atomic-localised orbitals $\widetilde{\phi}(\boldsymbol{r})$, where the time-independent electron density is:

$$n(\boldsymbol{r}) = \sum_{\boldsymbol{occ}} |\psi(\boldsymbol{r})^* \psi(\boldsymbol{r})|. \tag{3.71}$$

Since the corresponding time independent density matrix (or propagator) can be written as:

$$\rho_{\mu v} = \sum_{n} c_{\mu n} f_n c_{vn}^*, \tag{3.72}$$

with $c_{\mu n}$ as variational parameters, one can extract the pseudo density from density matrix as:

$$\widetilde{n}(\boldsymbol{r}) = \sum_{\mu v} \widetilde{\phi}(\boldsymbol{r})^* \widetilde{\phi}(\boldsymbol{r}) \rho_{\mu v} + \sum_{a} \widetilde{n}_c^a(\boldsymbol{r}). \tag{3.73}$$

The atomic-like basis functions are constructed as products of numerical radial

functions $\varphi_{nl}(r_\mu)$ and spherical harmonics $Y_{lm}(\hat{\boldsymbol{r}}_{\boldsymbol{\mu}})$, where

$$\widetilde{\boldsymbol{\phi}}(\boldsymbol{r}) = \widetilde{\boldsymbol{\phi}}\Big(\boldsymbol{r}_{\boldsymbol{\mu}} + \boldsymbol{R}_{\boldsymbol{\mu}}\Big) = \varphi_{nl}(r_\mu)Y_{lm}(\hat{\boldsymbol{r}}_{\boldsymbol{\mu}}), \tag{3.74}$$

where the position of nucleus μ is denoted by $\boldsymbol{R}_{\boldsymbol{\mu}}$. The major difference between the LCAO and PW approaches to DFT is that the variational parameters of the eigenvalue problem are the coefficients c_{vn} instead of the real space wave function. The eigenvalue problem that must be solved computationally through direct diagonalization of the Hamiltonian matrix is given by:

$$\sum_v H_{\mu v}c_{vn} = \sum_v S_{\mu v}c_{vn}\varepsilon_n. \tag{3.75}$$

To get the coefficients c_{vn} here, ε_n denotes the energies when the Hamiltonian $H_{\mu v}$ and the overlap matrix $S_{\boldsymbol{\mu} v}$ are known.

The RT-TDDFT calculations are based of the real-time propagation of the localised LCAO functions atomic-localised orbitals $\widetilde{\phi}(\boldsymbol{r})$ as described by Kuisma, et al. [175]. The action of the PAW operator $\hat{T}$ on the all-electron wave function,

$$\boldsymbol{\psi}(\boldsymbol{r}, t) = \hat{T}\widetilde{\boldsymbol{\psi}}(\widetilde{\boldsymbol{r}}, t) \tag{3.76}$$

transforms the Hamiltonian unitarily, such that:

$$\Big[\hat{T}^\dagger\Big(-i\frac{d}{dt} + \hat{\mathrm{H}}_{\mathrm{KS}}\Big)\hat{T}\Big]\psi(\widetilde{\boldsymbol{r}}, t) = 0. \tag{3.77}$$

This leads to the following matrix eigenvalue problem expressed as a first order differential equation:

$$-i\mathrm{S}\frac{d}{dt}\mathrm{C(t)} = \mathrm{H(t)C(t)}, \tag{3.78}$$

where C, S, and H are dense matrices of linear Hermitian operators. This is solved numerically using the semi-implicit Crank-Nicolson method to propagate the wavefunctions for C(t) in the predictor-corrector scheme.

The signatures of the near-field quantum electrodynamics in small clusters of

some Dirac materials are calculated at energies where topological quantum phase transitions are expected to occur

3.10 Quantum transport in ballistic conductors

This section presents theoretical model of electron scattering in quantum transport. Several techniques have been developed to study the transport of carriers in atomic conductors. This includes the method of nonequilibrium Green's functions combined with localized basis sets [176–179]. An alternative method involves the use of an independent system of wavelet basis to determine the Green's function [180]. In addition, the scattering method was used to investigate the resistance of atomic wires for both small and large bias [181]. The scattering of electrons has been proposed as the solution to the scattering problem for an open quantum system. A significant advantage of this method is that the scattering amplitude is based on the Landauer-Büttiker formula for relating the ballistic conductance to the total transmission coefficient at the Fermi energy.

In the ballistic transport regime, the electronic transport across nanoscale devices has no scattering among the electrodes [176]. However, the resistance can be high in the contacted regions. This is because the moving electron medium, is scattered by atoms of the contact since it behaves as impurities. Graphene and carbon nanotube manifest ballistic conductance. Quantum point contact devices that contain sub-micrometre scale lengths of these materials exhibit quantized conductance plateaus as a function of applied bias voltage. Insights into the transport character can be obtained by applying scattering theory of transport as a fundamental framework to explain the electrical conductance [182]. The two leads (electrodes) are connected to the nanocontact scatter region as shown in Fig. 3.5. Left (L) and right (R) leads are conductors, and act like reservoirs of charge (or spin) carriers so that the current flow can be defined as:

$$I = \frac{2e}{h} \int T(E) \Big[f_l(E) - f_R(E) \Big] dE, \tag{3.79}$$

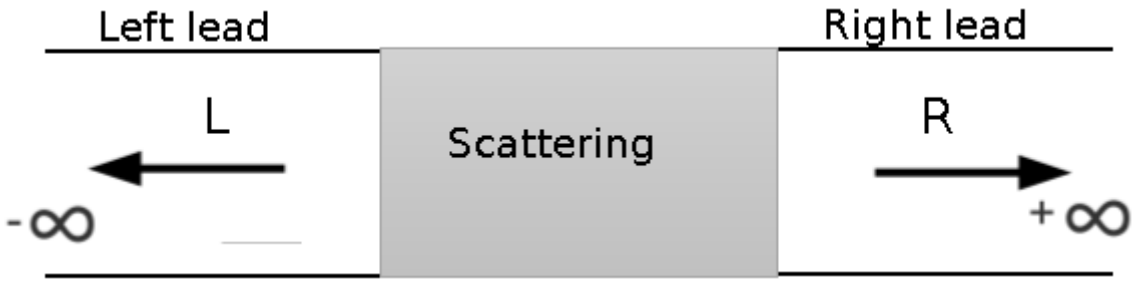

Figure 3.5: Open quantum system scheme, with the three regions left lead (L), scattering, and the right lead (R).

where $T(E)$ denotes the transmission, f denotes the Fermi Dirac distribution function, and h is the Plank's constant. At zero temperature, the current (I) is given by:

$$I = \frac{2e}{h} \int T(E) dE. \tag{3.80}$$

Using the Landauer-Büttiker formula, the spin conductance is given by [183, 184]:

$$G_\sigma = \frac{e^2}{h} \sum_{\boldsymbol{k}_\parallel} T_\sigma(\boldsymbol{k}_\parallel, E_F), \tag{3.81}$$

where $\boldsymbol{k}_\parallel$ defines the parallel component of the wave vector resolved along the plane of the 2D Brillouin zone.

Chapter 4

Computational Details

This chapter presents the details of the computational experiments performed in this thesis. The method of numerical renormalization group is introduced as the formal computational framework that are permits a systematic investigation of the changes that are inherent in the scale-dependent view of a physical system. This is used as basis for the qualitative understanding of the approach to the renormalization of carrier transport properties of Dirac materials on the tight-binding model of pristine graphene.

First-principles calculations are performed to determine the electronic structure in bulk TaAs. The method of implementing the renormalization of the electronic structure of bulk TaAs on the honeycomb lattice using a TB model of graphene is presented. The carrier transport state of the bulk TaAs on the field-dependent transport equivalent on the TB model of pristine graphene is used to track the emergence of topological phases.

Lastly, the computational set-up of the symmetric Co(111)/hBN/Co(111) and Co(111)/MoS_2/Co(111) multilayers and the method used to apply a perpendicular electric field to these architectures are presented.

4.1 First-principles calculations of the ground state in TaAs

Tantalum Arsenide (TaAs) crystallizes in the body-centered tetragonal crystal structure. Its crystal symmetry belongs to space group I41 md (No. 109). The lattice constants are a = b = 3.37Å, c=11.56Å [185]. State-of-the-art *ab initio* electronic structure calculations were performed within DFT using the plane wave self-consistent field code of the QUANTUM ESPRESSO (QE) package [186]. The interactions between ions and valence electrons are described using the projector augmented wave (PAW) potentials [149]. It treats the exchange-correlation interaction was accounted for in the Generalized Gradient Approximation as parameterized by Perdew-Burke-Ernzerhof (PBE) [135]. The cut-off of 45 and 270 Ry the kinetic energy and charge density expansions in the plane-wave basis. The $8\times8\times8$ uniform Monkhorst-Pack k-points mesh are used to reach convergence of total energies and Hellman-Feynman forces within 10^{-12} eV and 10^{-3} eV/Å, respectively. The Brillouin zone (BZ) is sampled with a much denser k-points mesh of $24 \times 24 \times 24$ [142]. The electronic states were populated using a Methfessels-Paxton (MP) smearing scheme using a width of 7.35 mRy [187]. The optimized unit cell of bulk TaAs is used to perform collinear magnetization calculations without spin-orbit coupling. In contrast, the non-collinear calculations were performed using fully relativistic pseudopotentials to incorporate SOC effect. The inclusion of SOC lifts Kramers' degeneracy by spin-splitting of of electron states that are degenerate without the SOC.

The field-theoretic equations used in the renormalization group (RG) analysis of massless Dirac fermions in graphene by Yusuke Nishida [188] are adopted in this study. By coupling the electronic structure to a supercritical Coulomb potential to mimic the effect of disorder, different regimes from weak, moderate to strong Coulombic electron-electron interactions and weak quenched disorder in graphene are explored. This is physically plausible because the competition between strong Coulombic interactions between electrons and a weak quenched disorder in graphene drives the emergence of quantum phase at 0 K. This is computational strategy is motivated by theoretical predictions of the one-loop renormalization calculation in graphene by Foster and Aleiner [189]. The one-loop RG calculation of the weak-

coupling shows that the following possibilities with graphene: (i) Coulomb interactions are irrelevant in the absence of disorder from the RG perspective because the clean Dirac description of the non-interacting ground state is stable. (ii) when a generic disorder is introduced to break the symmetry of the ground state, the noninteracting, clean Dirac fixed point (i.e., time-reversal symmetric BZ point KK′) becomes unstable. In this case, the system flows toward strong disorder and interaction coupling. This framework allows for the renormalization of the carrier transport state of any Dirac material onto an equivalent electronic band structure of the pristine graphene. Findings of the Yusuke Nishida RG analysis are also tested by analyzing the induced charge and current densities, as signature of the near field electrodynamic in the radiation-reaction approximation of the RT-TDDFT.

To study the emergence of topological quantum phases, electronic ground state in bulk TaAs is renormalized on the electronic structure of the graphene sheet within the TB model. Effects of the application of an external drive field to the rescaled graphene GS are investigated. This method allows for the analysis of the emergence of trivial equilibrium bands into non-equilibrium topological bands as a function of the external field intensity. The energy values utilized in the numerical computation are scaled by the hopping parameter t, which has different scales for different materials. In addition, the near-field electrodynamics calculations were performed on dimers and small clusters of TaAs and graphene to gain insight to the interaction between see the light materials from the nanoscale and the response of charge carrier to light during ballistic transport.

4.1.1 Van der Waals multilayer heterostructures

Herein the multilayer heterostructures of Co(111)/insulating Dirac materials/Co(111) were modelled to construct symmetric pMTJs via material physical stacking of monolayer materials using procedures analogous to those used recently to study multilayers [190–192]. The monolayer DMs such as hexagonal boron nitride (h-BN) and molybdenum disulfide (MoS_2) were placed as tunnel barriers. The semi-conducting h-BN layer has a wide bandgap. It used to raise graphene's conductivity, and it has

been employed in spintronic devices [193–196]. However, MoS_2 is a layered material with a direct bandgap suitable for a tunnel barrier in perpendicular magnetic tunnel junction (pMTJ) [197, 198].

The calculation of ballistic conductance using the PW basis is performed using the PWCOND code of the QE suite. The pMTJ model includes lead regions of Co(111) and scattering regions of monolayer hBN, or MoS_2. The equilibrium lattice constants of the system are separately relaxed. Using the supercell model of 2×2 in xy-plane with enough vacuum of 15 Å to avoid the interaction between nearest neighbour slabs. The obtained optimized lattice constants are: Co(111), 5-layers (5.0176 Å), h-BN, monolayer (5.112 Å) and MoS_2, monolayer (6.381 Å). To construct multilayers, the atomic simulation environment software [199] is used to put them together layer by layer.

In addition, scalar relativistic pseudopotentials are used to describe the exchange-correlation energy with non-empirical spin-density van der Waals density functional correction (svdw-DF2) [200–202]. Cutoff limits of 80 and 450 Ry were set for the kinetic energy and charge density expansions in the plane waves basis, respectively. The Monkhorst-Pack k-point grid of $6 \times 6 \times 1$ is utilised to sample the BZ [142]. A denser mesh of $18 \times 18 \times 1$ k-points is used for calculating the density of states (DOS). Electron states were populated using the Marzari-Vanderbilt cold smearing of a width of 0.0074 Ry [203].

4.1.2 Density of states (DOS)

The number of electrons N that occupy states in volume per energy unit E is known as the density of states (DOS). Its magnitude is given by: $N(E)\delta E$. It is essential to describe the electronic properties of the quantum system by interpreting the contribution of orbitals in energy level in the range $(E; E + \delta E)$. It can also be used to classify the electronic transport phase of a material [204]. The general formula of DOS can be understood from the dispersion relation between energy E and wave-vector $\boldsymbol{k}$ as:

$$E = \frac{\hbar^2}{2m}k^2. \tag{4.1}$$

The general definition of the total density of states in three dimensions is written as:

$$D(E) = \frac{1}{2\pi^2}.\left(\frac{2m}{\hbar^2}\right)^{\frac{3}{2}}.E^{\frac{1}{2}}. \tag{4.2}$$

The lower density of states describes the disappearing occupying states. However, high DOS represents the availability of states to occupy. Although DFT systematically underestimates the bandgap of some phases, such as semiconductor and insulator, it successfully reproduces the shape of the DOS. Also, topological effects significantly impact the electronic signatures that appear in the DOS in condensed matter systems. Such signatures include the appearance of van Hove singularities (or kinks) in the DOS. The wavevectors at which such singularities or kink states occur in k-space are often referred to as critical points of the Brillouin zone. However, this critical point, which influences the optical absorption properties of the material is not related to the critical points observed in phase diagrams.

4.1.3 Charge transfer at interfaces

The charge density difference (CDD) is used to define the charge transfer [205] and determine the electrons density excess and lack at the interface. Therefore, the interactions between Co(111) leads and tunnel barrier regions was obtained by computing the charge distribution at the interface. The proximity effects induced magnetoelectric couplings were determined using the electronic density of the ground-state. The interfacial charge transfer $\triangle\rho(\boldsymbol{r})$ due to the covalent bonding and proximity effects in the multilayer heterostructures were determined using the expression [206]:

$$\triangle\, \rho(\boldsymbol{r}) = \rho_{Het}(\boldsymbol{r}) - \rho_{Co}(\boldsymbol{r}) - \rho_X(\boldsymbol{r}), \tag{4.3}$$

where $\rho_{Het}(\boldsymbol{r})$ denotes the charge density in the multilayer, $\rho_{Co}(\boldsymbol{r})$ indicates the charge density when the atoms in the barrier region have been deleted, and all Co atoms are maintained in their positions as in the unit cell of the multilayer. However,

$\rho_X(\boldsymbol{r})$ denotes the charge density calculated for the monolayer tunnel barriers when all Co atoms have been deleted from the supercell model of the multilayer and all atomic positions in species $X = MoS_2$ (or hBN) are kept.

4.2 Ballistic carrier transport

Figure 3.5 the schematic of the open quantum system of the mesoscopic structure of the multilayer system in the pMTJ. This structure is used in computational experiments to imitate the ballistic transport behavior of the pMTJs when it is connected to metallic electrodes. Applying a small bias on those leads will cause charge (or spin) carriers to flow leading to measurable transport properties. Herein, the spin tunneling probabilities, quantum conductance and tunneling magnetoresistance were calculated. The open quantum system (Fig. 3.5) is made of three central regions. These are the scatter region (S), the left (L) and right (R) leads, respectively. It is assumed that two spin-polarized (i.e. spin-up, and spin-down) electrons pass ballistically through the barrier, each elastic scattering occurs in the scattering area, a wire consisting of one atom or a molecule [176].

Leads L and R are considered to be semi-infinitely linked to far away electron reservoirs. Therefore, the conductance of the system over the scattering zone was determined via the Landauer formula, $G = \frac{2e^2}{h}T$ [183, 184]. The quantum transport properties were calculated using the field theory that has been implemented in the PWCOND code of the QE package [176, 207] with open boundary conditions. The dense $60 \times 60 \times 1$ k-mesh was used to calculate the wavevector-dependent spin transmission spectrum.

For simulating the transmission of spin carriers in pMTJs, the spin degree of freedom is considered to be conserved during the tunneling process with respect to the z-axis of spin quantization. This axis also corresponds to the direction of collinear magnetization in the determination of tunneling magnetoresistance (TMR). The TMR signal was calculated using: is $TMR = \frac{G_P - G_{AP}}{G_{AP}} \times 100\%$ where G_P and G_{AP} denote the conductance for the parallel (P) and anti-parallel (AP) alignments of the leads, respectively. Nevertheless, $G = \frac{e^2}{h}(T^{\uparrow} + T^{\downarrow})$, where $T^{\uparrow}$ and $T^{\downarrow}$ denote

the majority-spin and minority-spin conductance obtained in the parallel or anti-parallel configurations at Fermi level. The constant $\frac{e^2}{h}$ denotes the conductance quantum.

4.3 Effect of applied electric field on the ground state

Symmetry place a central role in physics. At 0 K, breaking the crystal symmetry that controls Bloch states nature will lead emergent new phases. These emergent quantum phases can undergo transitions at 0 K when an external perturbing potential couples to the electronic ground state to break the intrinsic symmetry. For instance, in the existence of time-reversal symmetry, the orbital magnetic moment and Berry curvature of the Bloch states must vanish unless inversion symmetry is broken [208]. Space inversion and time reversal are the two fundamental symmetries that are applicable to all crystalline materials [209, 210]. In the bulk TaAs and stacked hetero structures studied herein, the corresponding structural inversion symmetry is already broken. However, time-reversal symmetry of the electron state are explicitly broken in the calculations using SOC, electric field, magnetic field and electromagnetic field. Each of these field couples to the ground state of the graphene when applied, and behaves as a disorder potential of tunable intensity.

Various methods are used to apply the external electric field, depending on the system under study. Herein, a sawtooth potential is added to the bare ion Coulomb barrier to apply the perpendicular electric field to the heterostructures. The self-consistent loop for calculating the total energy of each structure is converged at the adjusted potential. However, the local system is not re-optimized at each new finite electric field. The applied electric field is given in Hartree atomic units (a.u.), where 1 Hartree a.u. $= 51.4220632 \times 10^{10}$ V/m. Applying electric field through pMTJ along the z-axis leads to the breaking of inversion symmetry of the ground state. This therefore introduces an additional term to the Hamiltonian, H^0. The expectation value of H^0 is the total energy obtained from the DFT, whereas the additional term is the Rashba spin-orbit Hamiltonian (H_R) associated with the electric field. The

additional term is given by:

$$H_R = \frac{\lambda_R}{2}(\boldsymbol{p} \times \hat{\boldsymbol{z}}).\boldsymbol{\sigma}, \tag{4.4}$$

where $\boldsymbol{\sigma}$ and λ_R denote the Pauli spin matrices and magnitude of the SOC, respectively, and λ_R is proportional to the applied electric field. The resulting k-space Hamiltonian, $H = H^0 + H^{\boldsymbol{k}}$, where $H_{\boldsymbol{k}} = \frac{\lambda_R}{2}(\boldsymbol{k} \times \hat{\boldsymbol{z}}).\boldsymbol{\sigma}$ characterizes a group of Bloch electrons, that move adiabatically as a wavepacket in a non-degenerate band of index n with a total energy E_n. The wavepacket was treated to enclose a range of quantized wavevectors smaller than the volume of the Brillouin zone. This implies that the dimension of the travelling disorder waves is far larger than the lattice constant in real space [211].

4.4 The effective Hamiltonian of graphene

The generic Hamiltonian of Equation (3.60) for a honeycomb lattice is used to characterize the carrier transport model equivalent of a Dirac material on the graphene band structure. The effective Hamiltonian of graphene is defined in this model as the sum of the following five terms:

$$\begin{aligned} H = & -t \sum_{\langle i,j\rangle\alpha} c^{\dagger}_{i\alpha} c_{j\alpha} \\ & + i\frac{\lambda_{SO}}{3\sqrt{3}} \sum_{\ll i,j \gg \beta} \nu_{ij} c^{\dagger}_{i\alpha} \sigma^{Z}_{\alpha\beta} c_{j\beta} \\ & + i\lambda_R(E_Z) \sum_{\langle i,j\rangle\alpha\beta} c^{\dagger}_{i\alpha} \big(\boldsymbol{\sigma} \times \hat{\boldsymbol{d}}_{i,j}\big)^{Z}_{\alpha\beta} c_{j\beta} \\ & - l \sum_{i\alpha} \mu_i E_Z c^{\dagger}_{i\alpha} c_{i\alpha} \\ & + M \sum_{i\alpha} c^{\dagger}_{i\alpha} \sigma^{Z} c_{i\alpha}. \end{aligned} \tag{4.5}$$

In this case, $c^{\dagger}_{i\alpha}$ ($c_{j\alpha}$) denote the of creation (annihilation) operators of an electron with spin polarization α at site i, and the sums over $\langle i,j\rangle$ and $\ll i,j \gg$ run over all the nearest or next nearest neighbour hopping sites. The terms of the effective

Hamiltonian in the above equation are explained as follows: the first term denotes the nearest-neighbour hopping (H^{hc}) with unit energy t. It takes the value $t \simeq 2.7$ eV [212]. The second term represents the intrinsic spin-orbit (H^{SO}), while the third term denotes Rashba spin-orbit (H^{R}) associated with nearest neighbour hoppings induced by external electric field E_z [213–215]. The fourth term is the staggered sub-lattice (H^{ST}) induced by the electric field E_z, while l denotes the buckling height of the lattice, and $\mu_i = \pm 1$. The last term denotes the magnetic exchange interactions (H^{M}) [169, 213, 216].

Consequently, signatures of the near-field electrodynamics of a Bloch electron that propagates in a 2D Dirac material will be influenced by the applied uniform drive field [217–221]. Field-dependence of the changes in such signatures is realized from the tight-binding formalism of graphene [220], and used herein as a sensitive probe of phase changes at zero temperature. The exchange field M is due to the coupling of the graphene sheet to a ferromagnet. It is achieved in multilayers that integrate a ferromagnetic slab in stacked hybrid materials [190–192]. Alternatively, when ferromagnetic atoms are deposited on the graphene. The vector operation $\boldsymbol{\sigma} \times \hat{\boldsymbol{d}}_{i,j}$ yields a spin matrix of zero diagonal and non-zero off-diagonal elements so that hopping from site i to j leads to the flipped-spin configuration.

4.5 Renormalizing the TaAs ground-state to the equivalent TB model of graphene and emergence of topologically-ordered phases

Probing topological quantum phase transitions (TQPTs) remains a fundamental challenge due to the lack of local order parameters. The tractability of quantum phases is achieved herein by studying the topological order that emerges through the projection of the DFT ground state in TaAs on the graphene lattice using the TB model. This is due to the similarity between their semi-metallic carrier transport character at zero temperature. Thus, and equivalence principles is adopted. It must be noted however, that the implied equivalence of the zero temperature ground state does not imply any similarity between their local atomic structures, bonding

chemistry or crystal lattice symmetry.

The QUANTUM HONEYCOMB software is used to calculate the transport and topological properties of quantum materials within the TB model [222]. This is performed by keeping the scaling parameters that reproduce the transport properties of the TaAs band structure with SOC on the graphene lattice. The correct low energy dispersion was reproduced with the hoping parameter of energy $t = 2.05$ eV. The scaling parameters such λ_R, λ_{SO}, μ, and E_Z are different for all materials and are defined in terms of t. In this context the renormalization parameters of the band structure are obtained with $\lambda_R/t = 0.04t$ and $M/t = 0.06t$.

The result of the renormalization strategy is equivalent to the considerations of the Kane-Mele model [223, 224], for a bulk system, with an additional exchange field term. Then, parameter fit to the bandgap in the Kane-Mele model corresponds to the bandgap in TaAs with SOC from DFT calculations. This mapping could generalize the analyses to all Dirac materials in carrier transport from the low-energy band dispersion. This parameter fitting is justifiable because the nature of the transport signature in Dirac material depends precisely on the low-energy excitation of carriers close to the Fermi level. Nevertheless, the magnitude of each scaling parameter (i.e., t, μ, and λ) used to characterize carrier transport differs for each Dirac material.

One of the main goals of research in modern CMP is to gain useful insights into the zero-temperature transport phase in quantum materials. By extension, it is desirable to understand the emergence of topological order from the action of any symmetry-breaking operation with applied fields, and to understand how to control and tune the transition between such topological quantum phase (TQPs). The exfoliation of graphene in 2004, and the surge in the number of related 2D materials discovered so far has led to proposals of a plethora of new research directions in the theoretical physics of quantum materials. Thus, 2D materials are considered as the best candidate for realizing quantum phase transitions via applied external fields or by stacking them to construct multilayers. This due to the complex interplay between their unique band topologies and the quantum confinement. Therefore,

characterizing how they react to electromagnetic fields is necessary for optical and optoelectronic applications.

Since the Hamiltonian in Equation (4.5) is written as a combination of the Rashba spin-orbit coupling effect, magnetic exchange field, and external electric field, calculations were performed using Quantum Honeycomb to drive topological phase changes and to derive the topological phase diagrams. These zero temperature phases are characterized by the pair of metrics of topological order. These are the topological invariants Z_2 and the Chern number C. Their discrete jumps distinguish transitions between different topologically ordered phases [225, 226]. These topological invariants are related to the Berry connection $A^{(j)}$ of the j^{th} band for a 2D crystalline system, where $A^{(j)}$ is defined as:

$$A^{(j)}(\boldsymbol{k}) = i\langle \upsilon_j(\boldsymbol{k})|\Delta_j \upsilon_j(\boldsymbol{k})\rangle, \boldsymbol{k} = (k_x, k_y), \tag{4.6}$$

and the Berry curvature $\Omega^{(j)}$ is given by:

$$\Omega^{(j)}(\boldsymbol{k}) = \Delta_j\langle \upsilon_j(\boldsymbol{k})|\Delta_j \upsilon_j(\boldsymbol{k})\rangle. \tag{4.7}$$

Thus, the integration over the Brillouin zone (BZ) give us Chern number of j^{th} band and can be written as:

$$C^{(j)} = \frac{1}{2\pi}\int_{BZ}(\boldsymbol{k})d\boldsymbol{k}. \tag{4.8}$$

The non-zero Chern number informs whether something topologically is happening in the wavefunction. Also, allows to distinguish between different topological phases. It is an intrinsic property of the band structure and has various effects on the carrier transport of the system [210, 227]. The role of the SOC in lifting the degeneracies of bulk bands in these calculations confirms that the spin is a good quantum number in this formalism.

Chapter 5

Results and Discussion

This chapter presents the results and discussion of the research outlined in this thesis. This chapter is based on the results and discussions presented in Refs. [1] and [2]. These include the structural properties of the bulk TaAs and the heterostructures. It discusses how external fields break the symmetry of the ground state and induce quantum phase transition. Also, it describes the interaction between light and matter, particularly when the bulk systems are reduced to atomic nanocluster. Furthermore, their responses to the electromagnetic field are presented and discussed.

5.1 Dirac material systems: bulk tantalum arsenide and graphene

5.1.1 Convergence test for bulk TaAs

The fundamental procedure in density functional theory calculations is to acquire suitable $ecutwfc$ and k-points for the crystal system under study. Figure 5.1 shows the convergence test of the cut-off energy and k-points for the bulk TaAs. It is obtained by adjusting their values through self-consistency calculation until the difference between the lowest total energy becomes very small. Also, it is a characteristic function for a plane-wave basis set where a single parameter controls the accuracy of computed results compared to a localized basis set. The cutoff value of 45 Ry and the k-points mesh of size $8 \times 8 \times 8$ give good convergence of the minimum total

energy are shown in Figs. 5.1(a) and 5.1(b), respectively. These convergence test calculations gave the values that were used to perform DFT calculation to determine the total energy of the GS.

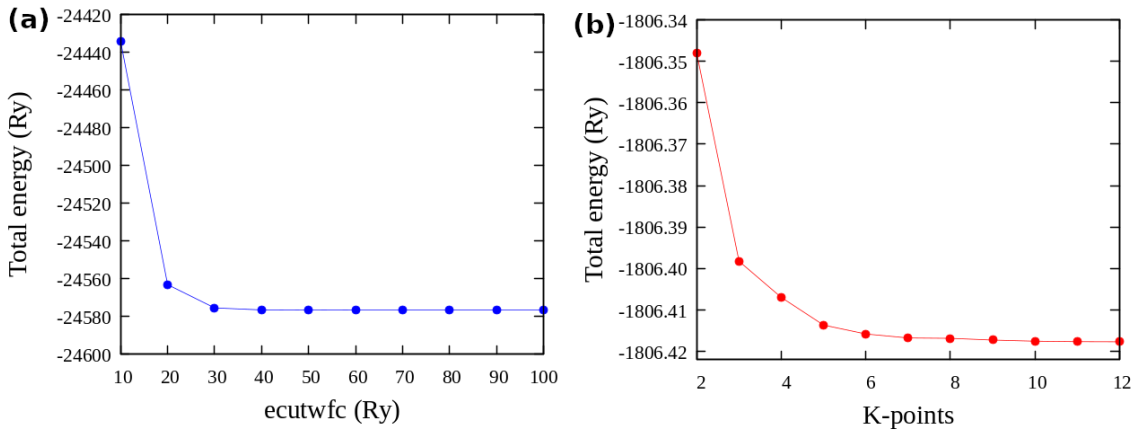

Figure 5.1: Convergence test of the (a) ecutwfc and (b) k-points for bulk TaAs.

5.1.2 Structural properties of bulk TaAs

Figure 5.2 shows the optimized structure of bulk TaAs, wherein the unit cell and its associated Brillouin zone are illustrated. The calculations show that the body-centred tetragonal unit cell is the most stable structural phase of TaAs. Also, this electronic structure converged to the correct non-magnetic ground state where the total magnetic moment was 0 μ_B, as expected. The lattice constants and internal coordinates of TaAs were fully relaxed, yielding lattice constants of a = b = 3.4347 Å, c = 11.6409 Å in good agreement with experimental values of a = b = 3.37 Å, c = 11.56 Å [228, 229]. This optimized structure was used as the input charge density for the self-consistency cycle to solve the Kohn-Sham (KS) equation in the collinear magnetic ground state calculations.

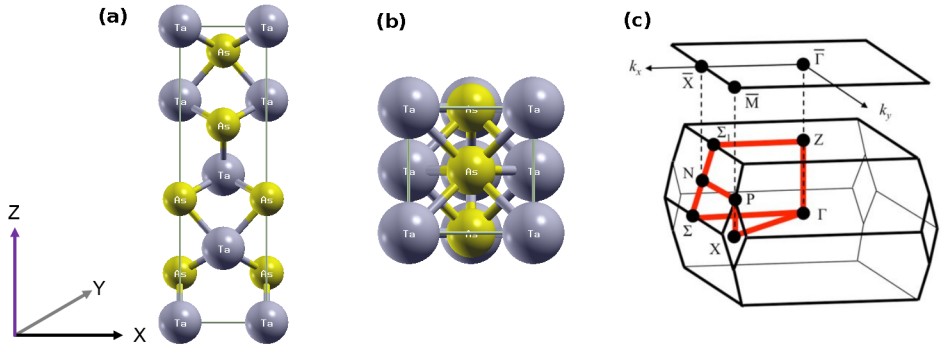

Figure 5.2: Optimized structure of the bulk TaAs, and its Brillouin zone. (a) Body-centred tetragonal unit cell. (b) Top view of TaAs unit cell. (c) Brillouin zone sampling path (red lines) through the high-symmetry points (black dots) for the bulk and surface, respectively.

5.1.3 Ground state electronic properties

Band structure

Figure 5.3 shows the band structures of bulk TaAs (top panels) and graphene sheet (bottom panels). In the absence of spin-orbit coupling (SOC), Fig. 5.3(a) indicates that the conduction and valence bands of TaAs intersect each other through the Σ-N-Σ_1 path in the Brillouin zone, as anticipated in a semimetal system. However, when SOC is introduced (see Fig. 5.3(b)), the band structure is wholly gapped along the path through the high symmetry points in the Brillouin zone. Band inversions are observed points Σ, N, and near to point Σ_1 along the Σ_1-Γ direction. At these points, the spin-orbit coupling brings the bottom of the conduction band below the top of the valence band and opens a gap at the band crossings. Furthermore, the inclusion of SOC induces the appearance of Weyl points that are shifted away from the high-symmetry points in reciprocal space. The bands degeneracies are also lifted. This is observable as the doubling of the number of distinct bands available in both valence and conduction bands. There is also a small change in the relative energy and position of the bands. This splitting of band energy levels show that the doubly-degenerate bands observed in the absence of SOC is lifted. This observation excludes pair of Kramers point N, which remain doubly degenerate - even when SOC is applied. The topological features of the TaAs band structure agrees with other

previous studies done on the same system [72, 230, 231]. According to Yan et al, the Weyl semimetallic nature of the bulk TaAs distinguishes it from graphene via the linear dispersion around the Weyl points [71]. Nevertheless, a finite band gap has been opened when the SOC is applied.

On the other hand, Fig. 5.3(c) shows the band structure of graphene sheet from the tight-binding (TB) model. Similar to TaAs, in the absence of SOC, graphene yields a zero-gap in the energy spectrum and a gapped band structure in the presence of SOC (see Fig. 5.3(d)). This electronic character is consistent with the semi-metallic transport signature as anticipated for pristine graphene. It is vital to affirm that the function of the SOC is to lift the Kramers degeneracies that arise in electronic states when SOC is ignored. However, The magnitude of the intrinsic SOC is extremely small to result in any measurable bandgap in the band structure of graphene. The invariance of the SOC under time-reversal symmetry signifies that additional fields that can break the symmetry of the electronic structure must be applied to the electronic states to change the bandgap in bulk TaAs. These additional fields are phenomenological, and they were simulated as magnetic exchange field M, external electric field E_Z and Rashba SOC (λ_R). The strength of SOC in graphene is weak when compared with other 2D materials such as germanene and silicene. Due to its low buckled structure, it presents a lower staggering potential with significant divergences in electron dynamics.

5.1.4 Effect of external fields on the band structure of TaAs mapped on graphene

Renormalization is a simple computational approach analyzing the occurrence of some physical model when the scale changes. Herein it is used to show how external drivers can be employed to tune the electronic band structure between trivial to non-trivial and vice versa, as a computational strategy for testing the formal hypothesis of the renormalizing group technique.

Figure 5.3(d) illustrates how the bandgap of a graphene sheet is affected by application of external fields. For instance, an applied Zeeman exchange of $M/t =$

$0.06t$, and a Rashba SOC of $\lambda_R/t = 0.04t$, result in an induced small bandgap. This is similar to what was observed with bulk TaAs when the SOC was introduced in its electronic band structure. Figure 5.3(b) emphasizes that the magnitude of this induced bandgap precisely corresponds to the SOC-induced bandgap in TaAs. This supports the foundation of the renormalization strategy for the ground state.

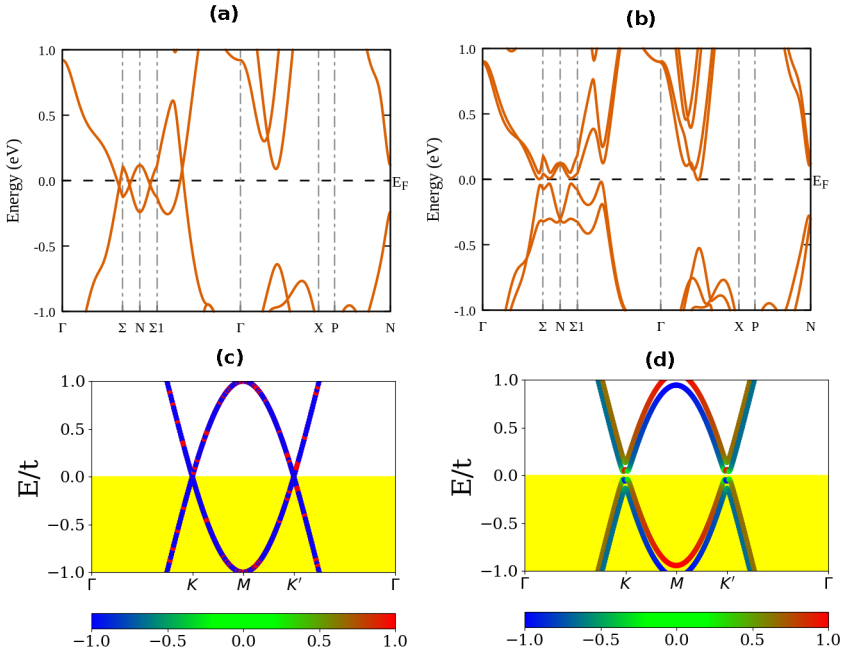

Figure 5.3: Electronic structure from DFT of the bulk TaAs in the (a) absence, and (b) presence of the SOC, respectively. The dashed horizontal line denotes the Fermi level. (c) The corresponding band structure of bulk TaAs renormalized to the graphene sheet in the absence of SOC. (d) In the presence of SOC, at $\lambda_R/t = 0.04t$ and exchange field $M/t = 0.06t$. The Fermi level is located at $E/t = 0$ eV, where t indicates the rescaled unit of energy. The color bars in (c) and (d) represent the value of the spin texture in units of S_Z, where $\hbar = 1$ [1].

Figure 5.3(a,c) shows the drive field lifts the degeneracy at the high symmetry points. The valence and conduction bands touch when time-reversal and spatial inversion symmetries are protected at generic points in the k-space that are not necessarily high-symmetry points. As anticipated, the ground state band structure shows semimetallic transport nature without SOC since the bands at Brillouin zone points K and K′ connect each other. Therefore, the presence of the SOC accurately characterizes the band structure of TaAs as supported by the induced small bandgap. With an equivalently small band gap in from the DFT band spectrum (see Fig.

5.3(b,d)). Spin orbit coupling again, removes the degeneracy of the electronic states, and this gives extremal spin textures, i.e., $S_Z = \pm 1$. However, the band structure does not sensitivity to spin due to the weak SOC in graphene [232].

In addition, Fig. 5.3(a) reveals that two of the four TaAs bands intersect at the Fermi level in the BZ. These bands the two bands that are modeled by the graphene band crossings at points K and K′ (see Fig. 5.3(c)). Therefore, the transport signature of TaAs around the Fermi level perfectly resemble the emergent transport character of the tuned graphene. Tuning the 2-band TB model with such field control parameters provide exceptional transport signatures in the honeycomb lattice. This confirms that the renormalization process accurately captures the effects of the SOC on the carrier transport character of the DFT ground state in TaAs. As mapping, the 3D TaAs structure onto the 2D structure is valid when they share the transport character and size of band gap. To functionalize the renormalization method, it is used here to follow the emergence of quantum phases an using TaAs as a model of Dirac materials.

5.1.5 Topological phase diagrams

The importance of topological phase diagrams (TPDs) is to delineate regions of topological and trivial phases and to identify unique TQPs. Herein, TPDs are combined with the electronic band structure plots to interpret the dispersion relation. This yields deeper insights into the low energy excitations of carriers. The topological numbers used to characterize quantum phases are topological invariant (Z_2) and the Chern number (C). The condition when $Z_2 = 1$ indicates a non-trivial quantum phase like the topological insulator phase. However, $Z_2 = 0$ implies a trivial phase like a common insulator. Order parameters are employed to illustrate the emergence of non-local topological order and determine the associated TQPs.

The bulk-edge correspondence principle accurately keeps the chiral edge states predicted in a graphene ribbon structure. According to the effective theory of low-energy excitations, the Hamiltonian that characterizes the carrier dynamics can be

given by:

$$h_{\pm,0}(\boldsymbol{k}-\boldsymbol{k_0}) = E_0(\boldsymbol{k}-\boldsymbol{k_0})\sigma_0 + V_x q_1 \sigma_x + m_0 \sigma_z, \tag{5.1}$$

where σ denotes the Pauli matrices. The mass m defines the tuning parameter for the topological phase transitions [233]. For instance, the phase transition between the quantum spin Hall (QSH) and the band insulator (BI) emerges when the sign of m term in equation (5.1) is reversed. It is characterised only by Z_2. Both time-reversal and inversion symmetries ensure that the order-parameter C, disappears. The electronic character near the transition point between two quantum phases tends to enhance field-dependent reactions. The neighborhood of such points on a phase diagram can be tractable using topological numbers, wherein the transition between different topological phases are described by the Z_2 and C order parameters. Their integral form for the electronic phase quantifies the topological order and a discontinuous change in their values signals a topological quantum phase transition. As the intensity of the external driving grows to the critical point spontaneously, the Hamiltonian of the electronic system spontaneously breaks the symmetry. Therefore, the phase could change from a trivial to a non-trivial phase and vice versa. Since Z_2 and C are good quantum numbers vital in distinguishing the quantum states of matter at 0 K, such as topological or trivial phases, they can be used to map topological phase diagrams to identify topological phase transitions (TQPTs) .topological phase diagrams and the corresponding band structures are interpreted to show that the TQPT points are tunable by applying global symmetry-breaking fields.

Figures 5.4 - 5.7 show different TPDs and the band structure around the Fermi level as response functions of the changes in topological order parameters (Z_2, C). The TPDs describe the dependence of the topological order parameters on the intensity of the different fields, such as Rashba SOC (λ_R/t) and the Zeeman exchange (M/t). Also, the band structures are characterized as variations of field drivers at distinct regions where topological phase transition occurs. For example, Fig. 5.4 shows the topological invariant phase diagram [Fig. 5.4(a)], and the band structure [Fig. 5.4(b) and (c)] corresponding to the pairs of the topological order parame-

ters (TOPs), denoted by the pair of parameter (Z_2, C), are shown as a functional dependence on the intensity of the Rashba SOC and the Zeeman exchange fields. Fig. 5.4(a) signifies the spectral response of the Z_2 invariant derived as a variation of λ_R/t with M/t. In Fig. 5.4(a), the phase diagram is colour-coded to show a large region of distinct values of the TOP for distinguishing between trivial (green), and non-trivial (blue) quantum phases.

As the drive field intensity is increased, additional quantum phases emerge [see Fig. 5.4(a)]. Different band topologies characterize these additional quantum phases. For instance, their low-energy dispersion spectra and spin textures are dissimilar. Fig. 5.4(b) and (c) also shows that the change in the TOPs is accompanied by corresponding changes in the spin texture of the electronic transport phase during the TQPT. For illustration, Figs. 5.4(b) and (c) show the region around the Fermi level within the energy window ±1.0 eV. It is for band structures that correspond to the pair of TOPs (Z_2, C) equivalent to (1,2) and (0,0), respectively. Similarly, Fig. 5.4(b) and (c) shows that the changes in the TOPs is also accompanied by corresponding changes in the spin texture of the electronic transport phase during the TQPT. The are the discrete points of the TPD, wherein a discontinuous change in the TOP modifies the electronic state manifold either from one topological phase to another (see Fig. 5.4(b)) or from a topological to a trivial phase (see Fig. 5.4(c)).

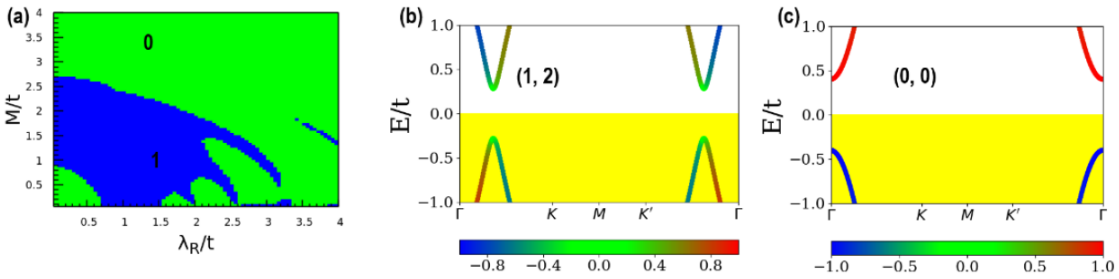

Figure 5.4: Effect of the Rashba SOC and the Zeeman exchange fields on the topological invariant phase diagram (a) and the band structures [(b), and (c)] of the electronic phases that correspond to topological order parameter pair, (Z_2, C). The phase field is color-coded green to denote Z_2=0, while color blue denotes Z_2=1 (a). The graphene band structure around the Fermi level in electronic phases wherein the topological order parameter pair (Z_2, C) is equivalent to (1,2) and (0,0) as an independent TQPT from phase fields wherein Z_2 is (b) 0, or (c) it is equal to 1.

To comprehend the fundamental differences between the band structures in Figs. 5.4(b) and (c), it is essential to note that the reference energy $E/t = 0$ eV denotes the Fermi level. Also, the yellow-shaded region of the band structure corresponds to the valence band. The blue, red, and green regions in all band structures represent the up spin ($\uparrow\uparrow$), down spin ($\downarrow\downarrow$), and chiral edge states. Since all available valence band states are occupied, the energy bands are described by different characteristic energy dispersions around the Fermi level. Therefore, the low-lying conduction and valence bands are displayed with an intrinsic spin texture (denoted by the colour bar in Figs. 5.4(b) and (c)). The spin textures that characterize electron states in the trivial band structure (Fig.5.4(c)), are different from the ones in the topological band structure [see Fig. 5.4(b)].

In Fig. 5.4(c), electron states possess opposite spin textures. The conduction and valence bands states are exclusively endowed with a positive, and negative spin textures, respectively. The topological band structure [see Fig. 5.4(b)] is characterized by a mixed spin-state texture. In this case, the Dirac dispersions around the Fermi level are characterized by spin-texture reversal when time-reversal symmetry is enforced on the electron state. This observation is consistent in valence and conduction electron states although the character of carrier dispersion is invariant with the band manifold. The spin textures in the two channels are very different despite their observed similarities since spin is an eigenstate of the Hamiltonian under broken time-reversal symmetry.

Figure 5.5 shows the Chern number phase diagram [Fig. 5.5(a)] and the band structure for each of the unique electronic phases identified with pairs of TOPs. Distinct electronic phases are labelled by integer Chern numbers -1, 0, 2 and 3, respectively, and their TQPTs yield three unique electronic structures shown in Figs. 5.5(b-d). Figs. 5.5(b) and (c) denote a minimally gapped electronic phase, with similar low-energy dispersions except that the energy of both of the conduction and valence band states are slightly shifted at the $\Gamma-$point, despite the similarity in their low-energy dispersion profiles. Nonetheless, their electronic phases are nontrivial since they correspond to the TOPs of (0,3), and (0,-1), respectively. By contrast,

Fig. 5.5(d) shows the TOPs of (1,2) in the electronic phase. The corresponding band structure has a large $\Gamma-$point gap (at least 2 eV). It is important to note that a fourth, albeit trivial, quantum phase of the electron state also exists in the ground-state manifold [see Fig. 5.5(a)]. This manifests as an independent subset of the Chern number phase diagram.

One way to understand the (0,0) electronic phase is by noting that the perturbation of the ground state by an internal (or external) field also varies the eigenfunction spectrum of the Hamiltonian. The resulting phase transitions are, therefore, either topological or trivial. As discovered recently by Chen et al. [234] in an anisotropic antiferromagnetic spin-1 biquadratic model, symmetry protection in both trivial and quantum phases play a significant role in electronic phase transitions. The authors discovered that the quantum phase transitions between the symmetry-protected trivial phases belong to the Gaussian universality class with central charge of $c = 1$. In contrast, quantum phase transitions from the symmetry-protected trivial phases to the dimerized phase belong to, instead, the Ising universality class with central charge of $c = \frac{1}{2}$. QPTs between the two trivial (0,0) phases imply symmetry protection in the models.

In the case discussed in this thesis, contrast, symmetry-breaking causes any of the possible transitions from the trivial (0,0) to either (0,3) or (0,-1) topological phases. It must also be considered that symmetry breaking perturbations by the external field induces a modification of the local curvature of the associated Berry phase. This agrees with the findings of Li et al. have showed that internal fields control the QPT in the trivial phase found on the graphene torus [93]. Thus, insofar as the QPT between the two trivial (0,0) is concerned, the Chern number is unchanged under the constraining effect of an internal or external field unless the renormalization flow takes the system towards a TQPT point.

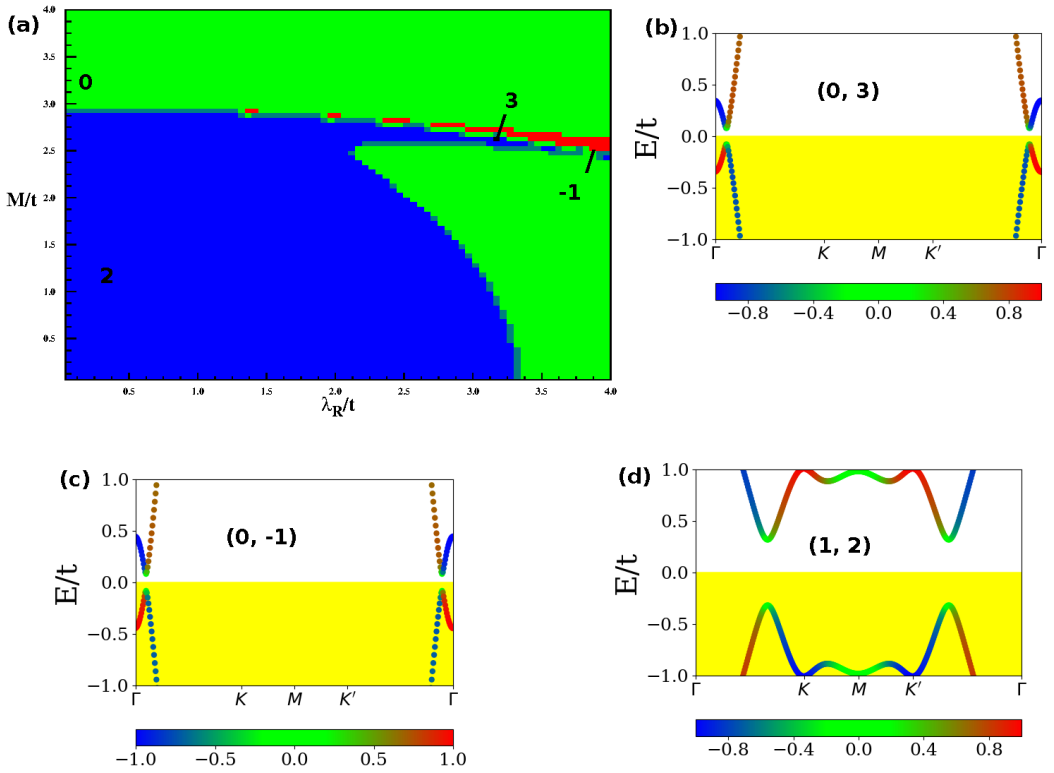

Figure 5.5: Chern number phase diagram obtained as a functional dependence on the intensity of the Rashba SOC and Zeeman exchange fields (a). The phase field is color-coded green to denote $C = 0$, blue to denote $C = 2$, red to denote $C = -1$ and black to denote $C = 3$. The band structure around the Fermi level in electronic phases wherein the topological order parameter pair (Z_2, C) is equivalent to (b) (0,3), (c) (0,-1), and (d) (1,2).

In the following discussion, the influence of the staggered sublattice potential, μ, on the ground-state electronic structure is explored. This action emanates from the buckled structure of the honeycomb structure, although the magnitude of μ in graphene is small unlike in other 2D forms of Dirac materials. To understand the following analyses, consider that the, the honeycomb lattice representation of the Haldane model has four phases, three non-trivial with $C = +2$, and one trivial insulator phase with $C = 0$, respectively [223]. Figure 5.6 demonstrates the effect of the staggered sublattice potential μ on the Z_2 phase diagram of the Haldane model in the honeycomb lattice [235]. The distinct TQPTs of the phase diagram are clear from the parameter space of the Hamiltonian. These are associated with systematic changes in the topological order parameters and the dispersion character from the band structure. The response of the ground state to a small change in the

sublattice potential μ is described via sensitivity of the TOPs and its effects on the electronic. The findings reveal that a facile electronic switch is available on these when using a symmetry-breaking field as the micro-probe of the electronic structure. The approach of breaking the ground state symmetry using the sub-lattice potential μ guarantees the presence of the presence of edge states are tunable from the energy dispersion. This offers a route for direct control of topological phases of matter through the use of metamaterials, multilayers, surfaces, edges, and atomic clusters.

Figure 5.6(a) illustrates the topological invariant Z_2 phase diagram obtained for $\mu_1 = 0.1t$. This again reveals two regions of phases denoted by $Z_2 = 0$ (green) and Z_2 =1 (blue), respectively. However, Fig. 5.6(b) depicts the adjusted band structure of the (0,0) trivial electronic phase at $0.1t$. A small bandgap marks the band structure at the K and K' points of the BZ. Again, the energy dispersion's nature is different from the band structure of the analogous electronic phases. It is found that, μ has particularly impacted energy dispersion without changing the underlying topological order of the electronic phase since the pair of order parameters (0,0) are unchanged. Nevertheless, Fig. 5.6(c) indicates that the band structure of the electronic phase that undergoes the TQPT has changed. Physically, this change can occur under the distortion of the unit cell due to the change is sub-lattice potential μ_1.

Fig. 5.6(d) shows the phase diagram of the topological invariant Z_2 when the staggered potential is set to $\mu_2 = 0.3t$. Similarly, Figs. 5.6(e,f) describe the complementary band structures at the specific region in the phase diagram. It found that this value of the sublattice potential causes a transition between trivial and topological phases. The non-zero Chern numbers (see Figs. 5.6(c,e,f)) ensure the presence of edge states (indicated by the green color) due to the topological index theorem [236].

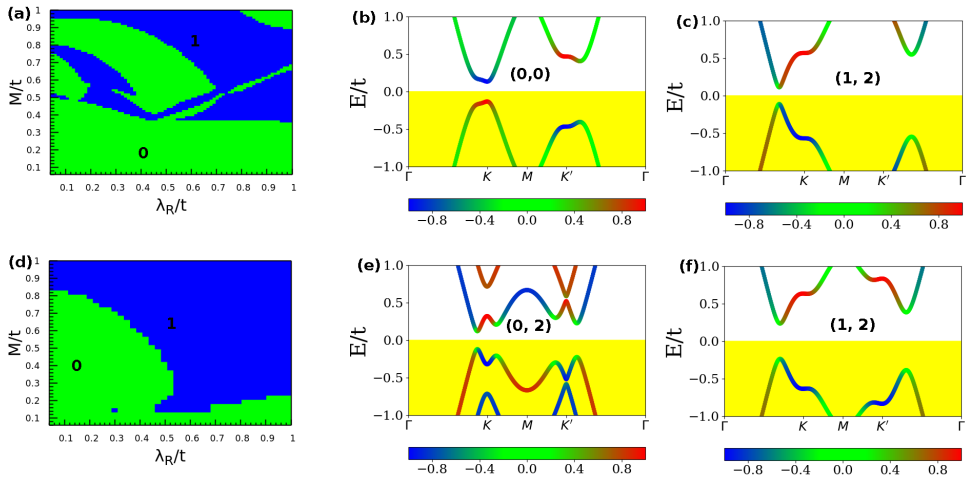

Figure 5.6: (a) Effect of a fixed staggered sublattice potential of $0.1t$ on the topological invariant phase diagram of the Haldane model on the modified honeycomb lattice. The associated band structure of specified electronic phases in phase fields is indicated by the (b) blue, and (c) green colors. (d) A similar plot at a fixed staggered sublattice potential of $0.3t$. The band structures are associated with the two-phase regions denoted by colors (e) blue, and (f) green. The color bars in (b,c) and (e,f) denote the expectation value of the spin texture in units of S_Z, where $\hbar$ =1 [1].

The zero Chern number is associated with the trivial insulator phase in the Haldane model. It can only vary when it bisects another band at the transition region. Therefore, the transport signature for the emergent electronic phase must be either metallic, or semi-metallic without a gap. Thus, the opening of the KK'-points bandgap forms the topological insulating phase from the trivial band insulator phase. Thus, when the Fermi level is positioned within the gap region, the case where $C \neq 0$ means that bands must arise below the Fermi energy. This suggests that both the integer quantum Hall and gapless edge states must coexist in the existence of the disorder.

To understand the susceptibility of the electronic states to the underlying material, the Chern number phase diagram for two different intensities of the staggered potential μ was analysed. The staggered sublattice potential has been fixed to retain the character of the previous discussion. Figure 5.7 shows the Chern number phase diagram at staggered potentials of $\mu_1 = 0.1t$ (see Fig. 5.7(a)) and $\mu_2 = 0.3t$ (see Fig. 5.7(b)). Also, the band structures for certain quantum phases at the distinguished

Chern numbers are also provided, for comparison. The results reveal that the adjustment of Rashba SOC independently induces a narrow bandgap in the BZ path of all the band structures in Fig. 5.7. This suggests that the strength of the applied field recreates a significant function in the ground state at the TQPT. However, the intensity evolutions do not possess any other consequence once the phase transition has emerged.

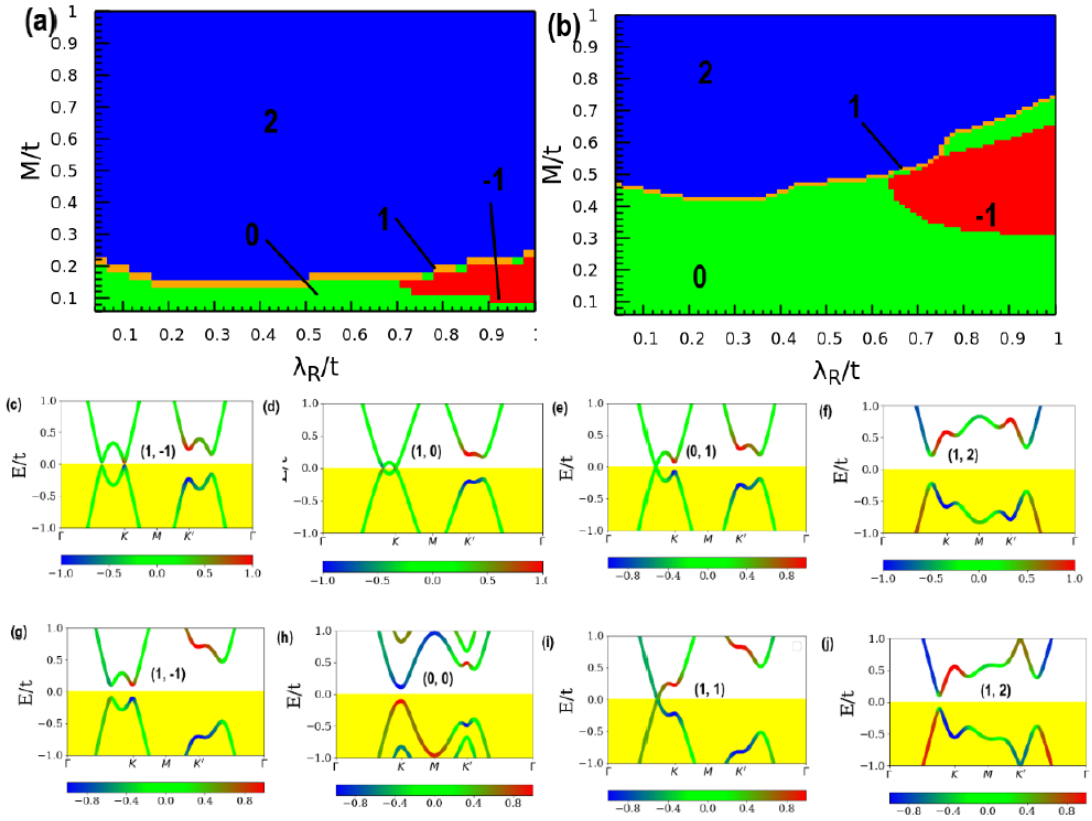

Figure 5.7: Chern number phase diagram as the function of staggered sublattice potential (a) $\mu_1 = 0.1t$, and (b) $\mu_2 = 0.3t$. Where the green color denotes C = 0, blue denotes C = 2, red denotes C = -1 and yellow denotes C = 1, respectively. The band structure derived for unique quantum phases at $0.1t$ are plotted for Chern numbers: (c) -1, (d) 0, (e) 1 , (f) 2. The corresponding band structure for unique quantum phases at $0.3t$ are plotted for Chern numbers: (g) -1, (h) 0, (i) 1, (j) 2, respectively. The color bars in (c) to (j) denote the expectation value of the spin texture in units of S_Z, where $\hbar$ =1 [1].

The Chern number phase diagram in Fig. 5.7(a,b) exhibits sensitivity to the changes in the Rashba SOC. For instance, the regions of the topological Chern phase widen and values of the Chern number are adjusted. This characteristic response

is systematic, and it is found when the effective Hamiltonian emphasizes transport a unique carrier transport, in the presence of a modification in the SOC parameter under the driving field. Figures 5.7(c-f) indicate that the Kramers degeneracy is lifted at the KK′ points in the energy spectrum. An equivalent routine has also adjusted the topological invariant Z_2 as a function of Rashba λ_R/t and Zeeman field M/t with a fixed value of electric field of $E_z/t = 0.5t$.

The analysis highlights that the transition between trivial and non-trivial phases emerged, and the bandgap rises when the field intensity grows. However, the increase in the Rashba field systematically reduces the bandgap. Resulting in a gapless band structure in the vicinity of K and K′. This explains the capability to adjust an ordinary insulator into a non-trivial insulator by changing electric field intensity since the Chern number for both suits is $C = 2$. Also, the findings in Figs. 5.4-5.7 reveal that if the values of Z_2 and C are non-zero. All the topological phenomena anticipated in the quantum Hall transport signature will be detectable, including the presence of the edge states. Also, fixing the staggering potential is an interior field condition that reaches the tunability of the SOC-induced various phases from the band structures, such as, the semiconducting, insulator, and metallic.

5.2 Van der Waals multilayer heterostructures

5.2.1 Convergence test

As mentioned in Section 5.1.1, convergence testing is a crucial strategy in scientific computing that will always be performed to provide appropriate input crystal structure and tuning parameters for principles calculations performed based on DFT. Figures 5.8(a,b) and Figs. 5.8(c,d) illustrate the convergence tests for the cutoff limit for kinetic energy expansion in the plane waves basis, and the k-points mesh for Co(111)/hBN/Co(111) and Co(111)/MoS_2/Co(111), respectively. The results show that a suitable BZ sampling is achieved in reciprocal space when the k-points mesh and the cutoff energy for both multilayers have a nearly equal number of $6 \times 6 \times 1$ and ecut of 80 Ry.

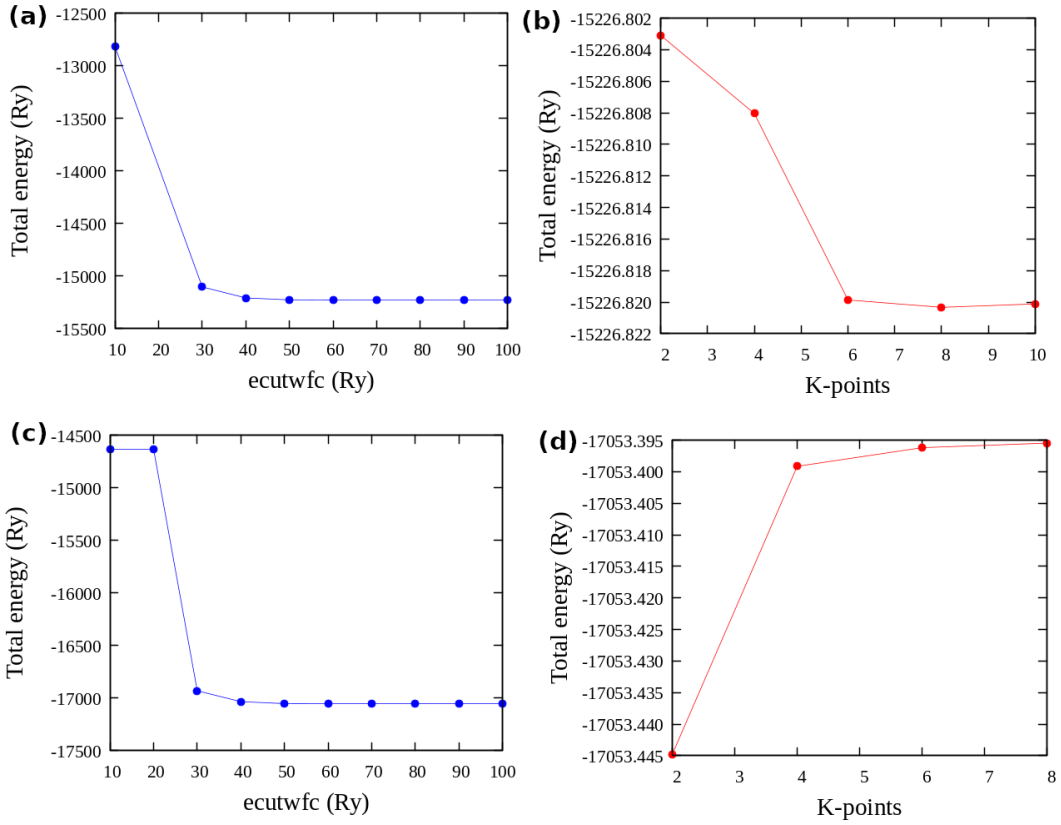

Figure 5.8: Convergence tests of the multilayer stacks, for (a) cut-off energy, and (b) k-points of Co(111)/hBN/Co(111), (c) cut-off energy, and (d) k-points for Co(111)/MoS_2/Co(111) heterostructure.

5.2.2 Structural properties

Figure 5.9 describes the construction of artificially constructed hybrid materials and the optimized structure of the Co(111)/hBN/Co(111) and Co(111)/MoS_2/Co(111) stacks in the cubical unit cell. The central (green) zone of the structures represents the scattering region, which is made of a monolayer of either hBN or 2H-polytype of MoS_2. However, the orange zone in Fig. 5.9(a) illustrates the right (R) and left (L) leads, which are made of five layers of fcc Co(111) surface. Therefore, pMTJs derived in this measurement geometry are symmetric because both leads are created from surface slabs of the same material. The results demonstrate that the interlayer distance between the Co(111) slab and hBN layer is $d_{Co(111)/hBN} = 3.38$ Å. This distrance is the same for the top and bottom leads. These results agree well with the other studies [190, 192, 237, 238].

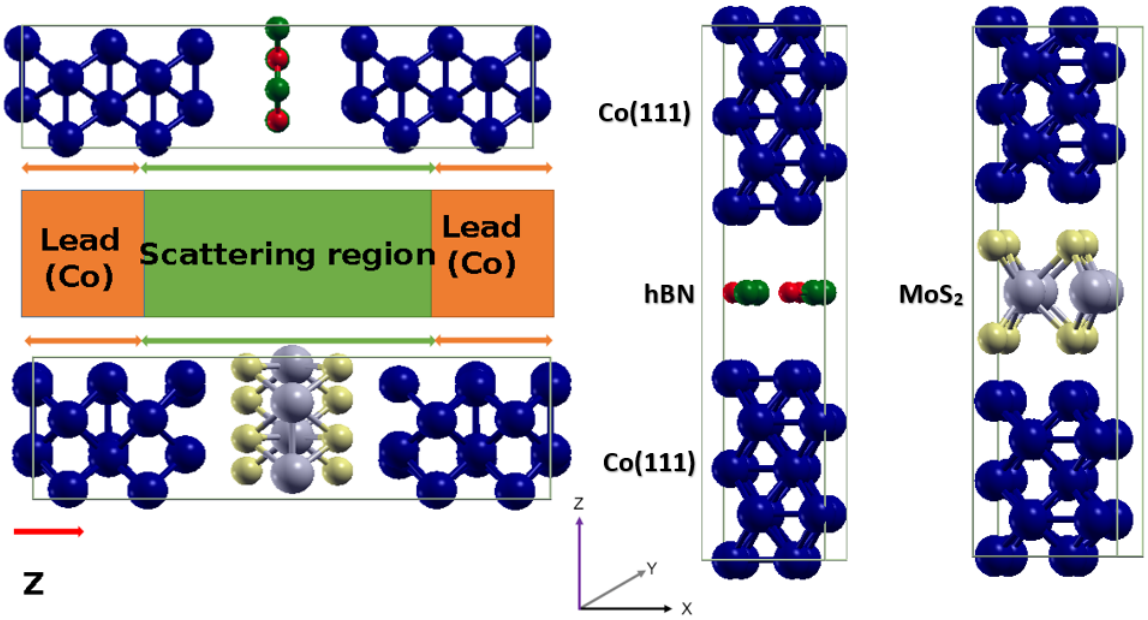

Figure 5.9: The optimized unit cell for the local structures and the schematic diagram of the pMTJ showing two similar leads and a central scattering region. (a) Co(111)/hBN/Co(111) stack. (b) B (N) atoms are displayed in green (red), respectively. (b) Co(111)/MoS_2/Co(111) heterostructure. (c) Mo (S) atoms are illustrated in grey (yellow), respectively. The vector Z denotes the spin transport direction [2].

The interlayer distance between Co(111) and the upper layer S atoms of the MoS_2 layer is $d_{Co(111)/MoS_2}$ = 2.28 Å. This also agrees well with other investigations [205, 238–240]. This shows that the electronic system is satisfactorily set up for the DFT computations of the lowest ground state. Furthermore, the interatomic spaces are similar for both metallic electrodes of the symmetric heterostructure. The length of the metallic Co-Co bonds is unaffected because of the invariance between the local structure in the fixed (bottom) and free (top) layers. Houari et al. [241] suggest that at equilibrium, the ground state in metallic cobalt is ferromagnetic and that the hcp phase was better stable than the fcc phase. Nevertheless, the computed nearest-neighbour distances are discovered here to be slightly lower than the 2.54 Å distance anticipated in the stable but nonmagnetic fcc phase.

5.2.3 Magnetic properties

Magnetic moments

Figure 5.10 illustrates the distribution of magnetic moments (m) at the ground state (GS) (blue circle) and for various intensities of the electric field (black and red). The GS spin moments reveal the slightest variations close to the average, irrespective of the type of barrier material. When the electric field intensity is raised, the local relaxation of the m demonstrates a strong sensitivity to the material of the tunnel region. When the material of the tunnel region is hBN, this is illustrated in the field-dependence of the evolution of the local magnetic moments in the bottom (reference) layer (see Fig.5.10(a)). A similar field-effect is also observed in the local moment when the barrier region is monolayer MoS_2. However, these zero-temperature fluctuation in local moments have no effect on quantum phase transition for the case where MoS_2 is the barrier. Nevertheless, in the top (free) layer (see Fig.5.10(b)), the applied field yields variations in localized m and breaks the symmetry of the ground state. The increase of field intensity from zero to 0.1 and 0.3 a.u. cause instabilities in magnetic moments in the range of -1.80 and -1.97 μ_B in the reference layer as displayed in Fig. 5.10(a). The field-induced instabilities resemble the variations in magnetic moments seen in the anti-ferromagnetic state with opposing spin directions. However, the variations of spin magnetic moments in the free layer is between 0.71 to 1.81 μ_B. This is similar to the variation in magnetic moments seen in a ferromagnetic state along the direction parallel to the direction of spin quantization. This presents a substantial layer-dependent instabilities when the hBN monolayer is incorporated in the tunnel barrier region.

At an intensity of 0.1 a.u., the spin moments of N atoms grew from 0.005 μ_B to 0.092 μ_B. Then it drops to -0.051 μ_B at a strength of 0.3 a.u. as seen clearly in the bottom panel of Fig.5.10(a). The application of a perpendicular electric field significantly contributes to the strength of electronic coupling [190]. The interfacial charge transfer between the Co-hBN heterobilayer is therefore mediated by the strong magnetization from Co-layers. This leads to polarization in the nonmagnetic

atoms of the hBN layer.

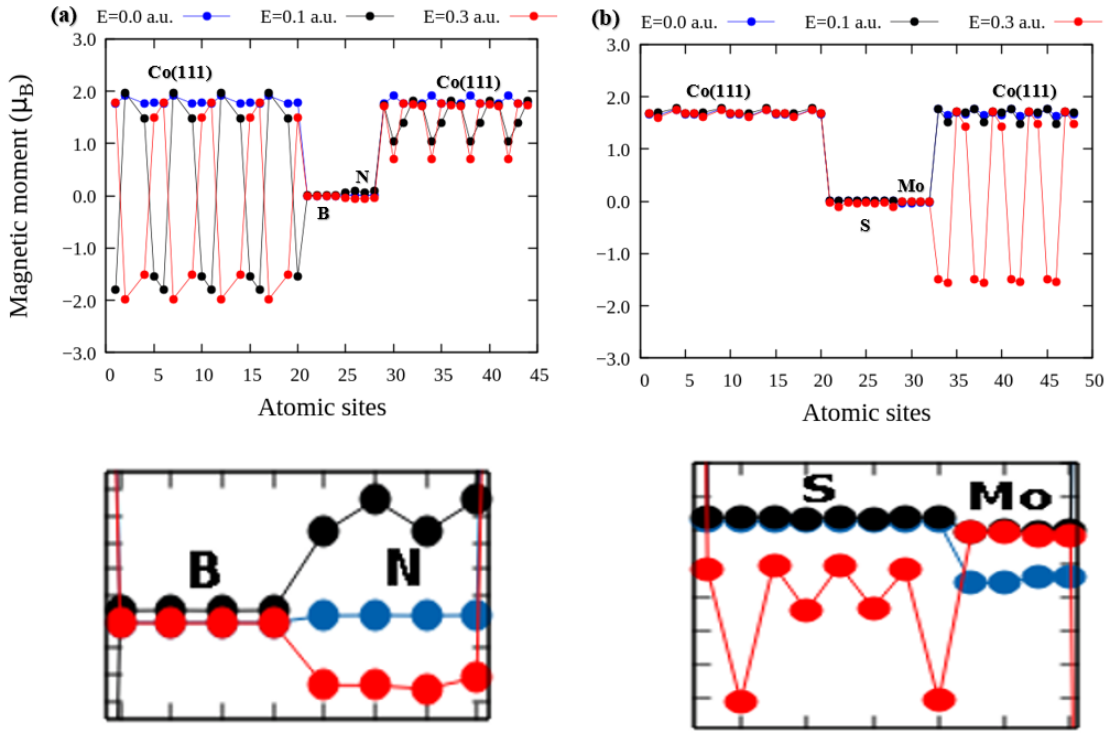

Figure 5.10: Magnetic spin moments (in μ_B) per atomic site of, (a) Co(111)/hBN/Co(111), and (b) Co(111)/ MoS_2/Co(111) interfaces. The colors (blue, black, and red) show the magnitudes of the electric field (in a.u.) as a function of the magnetic moment. The corresponding lower panels illustrate the zoomed-in image of the central region of the magnetic tunnel junction to show distributions of localized magnetic moments in monolayer hBN and MoS_2, respectively [2].

Figure 5.10(b) demonstrates the behaviour of spin moments under the influence of an electric field when the barrier is monolayer MoS_2. At zero-field, the magnetic moments of S (Mo) atoms are 0.006 (-0.031) μ_B, respectively, as in the zoomed-in bottom panel. At a field strength of 0.1 a.u., the magnetic moments rise to 0.0083 μ_B in S-atoms and starts to be polarized. The Mo-atoms stay unpolarized when the field intensity is increased to 0.3 a.u. The findings reveal that the reference layers are unchanged, and the significant changes in magnetic moments arise in the free layer at a high field of 0.3 a.u. (see Fig. 5.10(b)). The zoomed-in panel of Fig. 5.10(b) shows spin fluctuations in Mo and S atoms and and suggests a weak magnetic exchange between Mo and Co atoms. The analysis of the induced spin fluctuations shows the response of the ground state as the electric field intensity grows. The field-induced

changes lead to strong polarization in the monolayer barriers. This is attributed to the magnetocelectric couplings from the proximity effect in the hetero-bilayer interfaces within the lead - barrier - lead heterostructure.

Magnetization reversal and magnetic ordering energy

In this section, analysis of the response of the magnetic moments to changes in the intensity of the applied electric field is presented in term of changes in magnetization. Table 5.1 shows the electric field effects on the ground state energy ($\triangle E$), and the collinear magnetization (M) relative to the direction of the quantization of spin. Table 5.1 shows that the magnitude of the magnetization is sensitive to the material of the tunnel region. The total magnetization of the P (or AP) configuration simultaneously decreases (or increases) nonlinearly with an increase in the amplitude of the applied field for both tunnel barrier materials. In the parallel spin orientation, both barrier models show a net decrease in magnetization as the applied field is increased to 0.3 Hartree a.u. In the anti-parallel direction, the magnitude of magnetization reversed as the applied electric field is increased.

The magnetic ordering of the ground state of the multilayer heterostructure is also sensitive to the applied electric field. It decreases as applied field increases. The decreasing total magnetization observed in the P-configuration with monolayer hBN is more pronounced in the AP-configuration as a sign change in the magnetization. The observed negative magnetization shows a reversal of magnetization through proximity effects. This is a unique feature of the spin-flip transition necessary to realize a non-volatile 180° magnetization reversal in the spin-transport phase. The energy of magnetic ordering is calculated as $\triangle E = E(AP) - E(P)$, where $E(AP)(E(P))$ denotes the lowest total energy for AP(P) magnetic alignments, respectively.

Results of the pMTJ model that includes a hBN barrier show that $\triangle E$ drops as the electric field increases. It is found that as the electric field increases in intensity, the total magnetization (M) in the P (AP) alignment drops (increases), respectively. When the field reaches its critical value of 0.1 a.u., magnetic ordering

energy $\triangle E$ decreases below 0 eV. This is equivalent to the electric field causes the quantum phase transition (QPT). It is shown in Section 5.2.4 that this QPT leads to the dynamical stability in the tunnel magnetoresistance (TMR) signal. On the other hand, for pMTJs-based on MoS_2 barrier, the $\triangle E$ exhibits a contrasting trend compared to the hBN barrier. $\triangle E$ increases fast as field intensity increases before suddenly decreasing drops to -1.95 eV at field strength 0.3 a.u.

Table 5.1: Field effects on the ground state energy ($\triangle E$), magnetization (M) per cell (in μ_B) for spin aligned parallel (P), and antiparallel (AP) to the quantization axis.

Electric	Field	Co(111)/hBN/Co(111)			Co(111)/MoS_2/Co(111)		
(a.u.)	10^{10} (V/m)	$M(P)$	$M(AP)$	$\triangle E$ (eV)	$M(P)$	$M(AP)$	$\triangle E$ (eV)
0.0	0.0	62.6	-0.03	0.0	62.34	-0.57	0.0
0.01	0.51	62.5	0.32	-0.004	62.49	-0.48	0.002
0.1	5.14	18.3	4.31	-2.59	62.33	-0.28	0.038
0.3	15.43	28.0	12.25	-1.49	61.14	61.13	-1.95

Notwithstanding the nature of the tunnel barrier material, the data in Table 5.1 has shown a predominantly negative magnetization (M) as the intensity of the applied field is increased. This field-induced flipped-magnetization is a proximity effect that arises from changes in magnetic ordering energy, polarizations, and fluctuations in the local magnetic moments. These underlying signatures provide evidence of electric field mediated magneto-electric coupling in multilayers, without an explicit application of a magnetic field agrees with previous studies [242, 243]. The findings of recent experiments [244–246] support the insight generated from the theoretical and computational analyses presented in this thesis, that the magnetic moments that have appeared in the nonmagnetic layer is due to the proximity effect coupling in the magneto-electric signature of pMTJs in the interface. Others studies show the manipulation of magnetization reversal via the applied electric field found in ferromagnetic (FM) heterostructures [243, 247–249], anti-ferromagnets (AFM) in collinear [250] and noncollinear magnetization [251].

Electronic density of state (DOS)

The density of state provides a way to describe how the available energy states of a system are filled. This mechanism allow to specify the carrier transport state. Examples of such state include the insulating, semiconducting or metallic transport character identifiable from the band gap between the conduction and valence band. Herein, Figs. 5.11 and 5.12 show the effect of the applied electric field on the projected density of states (PDOS) for the two different models of pMTJs. Figure 5.11 demonstrates the effect of the applied field on the PDOS of the system based on the hBN barrier (top panels), as well as the PDOS of the barrier (bottom panels). At the ground state, Fig. 5.11(a) reveals that the spin-minority channel has ~ 40 of electronic states per eV/unit cell and vanishes in the spin-majority channel near the Fermi level. This is similar to the half-metallic transport phase.

At zero-field, the *d*-orbitals of Co atoms dominate the donation of DOS in the lowest unoccupied and highest occupied levels regardless of the barrier layer. However, at a field intensity of 0.1 a.u., the half-metallic state evolves into the metallic state as in Fig. 5.11(b). Consequently 0.1 a.u. characterise the critical point of the electric field in which the QPT expected to occur. This is due to the change in the population of the spin-majority channel of Co atoms from insulator to full-metallic state as seen in Figs. 5.11(a,b). Fig. 5.11(d,e,f) shows that at zero-field and the finite-field, the PDOS of the barrier (B and N atoms) contribute minimal electron states the electronic density of states near the Fermi level compared to Co.

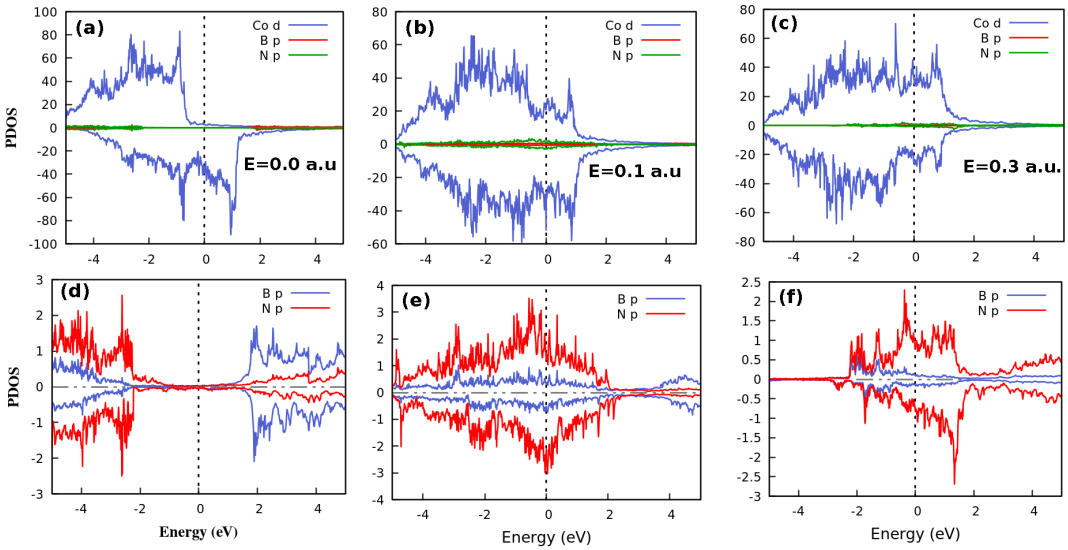

Figure 5.11: Top panel: Effect of applied electric field on the spin-polarized electronic DOS of hBN-based pMTJ. Bottom panel: The PDOS of hBN shows p-orbitals of B and N atoms. At the electric field of (a,d) 0, (b,e) 0.1, and (c,f) 0.3 a.u., respectively. Positive and negative PDOS denote spin-up and spin-down channels, respectively. The vertical dashed lines denote the Fermi level (E_F) [2].

Figures 5.11(d,e,f) also show that the finite field signature of hBN barrier model changes into the metallic from an insulating state. This is attributed to orbital hybridization. Moreover, the p-orbital of N and B atoms govern the distribution of states near the Fermi level. The p-orbitals of B atoms states in the spin-up at zero-field. Also, the transport signature at high field intensity (0.3 a.u.) remains metallic. The DOS of atoms within the the barrier region correlate with the local spin magnetic moments for the N atoms. Here the p-orbitals of the N atoms show comparatively stronger electronic response to the changes in applied field intensity. Crucially, the combined occurrence of extremal fluctuations in the localized magnetic moments on the N atoms (of the barrier (see Fig. 5.10(a)) as well as observation of similarly extremal p-orbital DOS at applied field intensity of 0.1 Hartree a. u. (see Fig. 5.11(e)) is not a random coincidence. In Section 5.2.4, it is shown that this is the critical intensity of the applied field in the underlying quantum phase transition.

Figure 5.12 illustrates the effect of the electric field on the DOS of the pMTJ based on the MoS_2 barrier (top panels). The DOS for the barrier layer is shown in the bottom panels. The PDOS at zero and finite fields are shown in Figs 5.12(a)-(c).

The d-orbital of Co governs the states at various field strengths. Overall, the half-metallic state characterizes the carrier transport signature in each case, as observed in Figs. 5.11(a,b,c). Thus, the applied electric field has no notable effect on carrier transport when MoS_2 is the tunnel barrier, unlike with the hBN barrier.

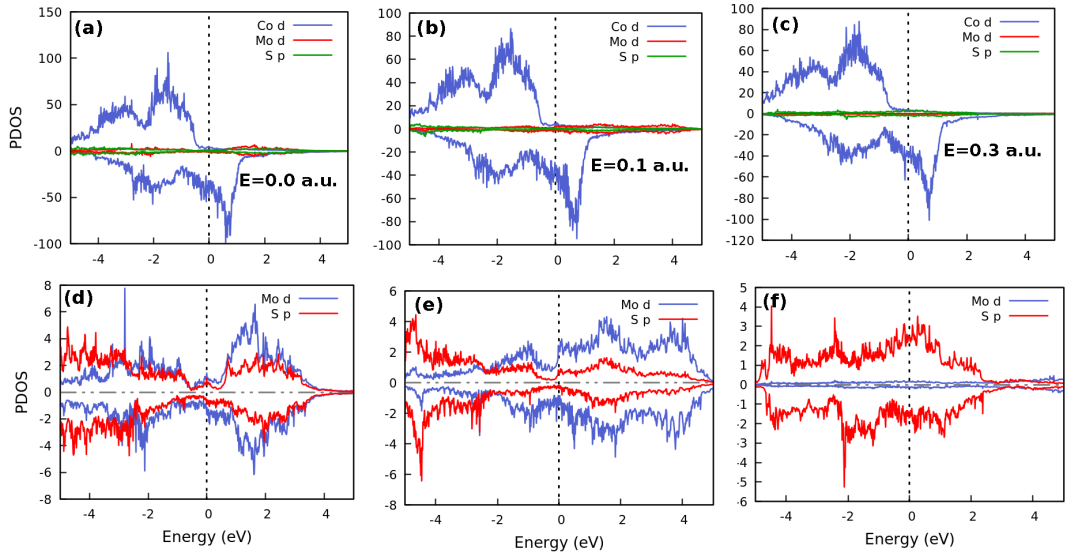

Figure 5.12: Top panel: Effect of applied electric field on the spin-polarized orbital-resolved electronic DOS of MoS_2 based pMTJ. Bottom panel: The PDOS for MoS_2 shows Mo d-orbital and S p-orbital. At the electric field of (a,d) 0, (b,e) 0.1, and (c,f) 0.3 a.u., respectively. Positive and negative PDOS denote spin-up and spin-down channels, respectively. The vertical dashed lines indicate the Fermi level (E_F) [2].

Consequently, the barrier systems respond differently to the applied field, particularly at the critical field. For example, for the hBN barrier, p-orbitals of N atoms control the states while the d-orbital of Mo atoms governs the states when MoS_2 is in the barrier. However, at 0.3 a.u., the metallic nature is controlled by the p-orbital of N and S atoms [see Figs. 5.11(f) and 5.12(f)]. The p-orbital of the S atom contributes states per eV near the Fermi level than the d-orbital of the Mo atom. The direct donation of electron states to the MoS_2 system does not originate from the Mo atoms alone, as found in Ref. [252]. In the present work, competition is found between the d (p) orbitals of Mo (S) atoms, respectively, at a high field of 0.3 a.u. The robust bonding between the MoS_2 and Co (111) and the small distance between S and Co tolerate notable wavefunction overlap between Co, Mo, and S states. This is equivalent to that found in Ti and MoS_2/metal contacts [253, 254].

Charge at the interfaces

Figure 5.13 displays the volume charge density difference $\triangle\rho(r)$ for the two models of the pMTJs at zero field and in the presence of the electric field. The yellow (cyan) colour denotes a localised excess (depletion) of charge density in each case. In addition, the distribution of charge at the interfaces provides intuitive insights into the interactions between leads and the barrier. Figure 5.13(a,b) shows the $\triangle\rho(r)$ of Co(111)/hBN/Co(111) system plotted with an isosurface value of 1×10^{-3} e/Å^3. At zero-field, a net transfer of charges has emerged at the interface between the Co and N atoms [see Fig. 5.13(a)]. The results reveal that hBN transforms into an electron-rich region due to the large charge collection around N atoms. In contrast, at 0.1 a.u., the Co atoms evolve as holes region [see Fig. 5.13(b)] due to the insufficiency of electrons.

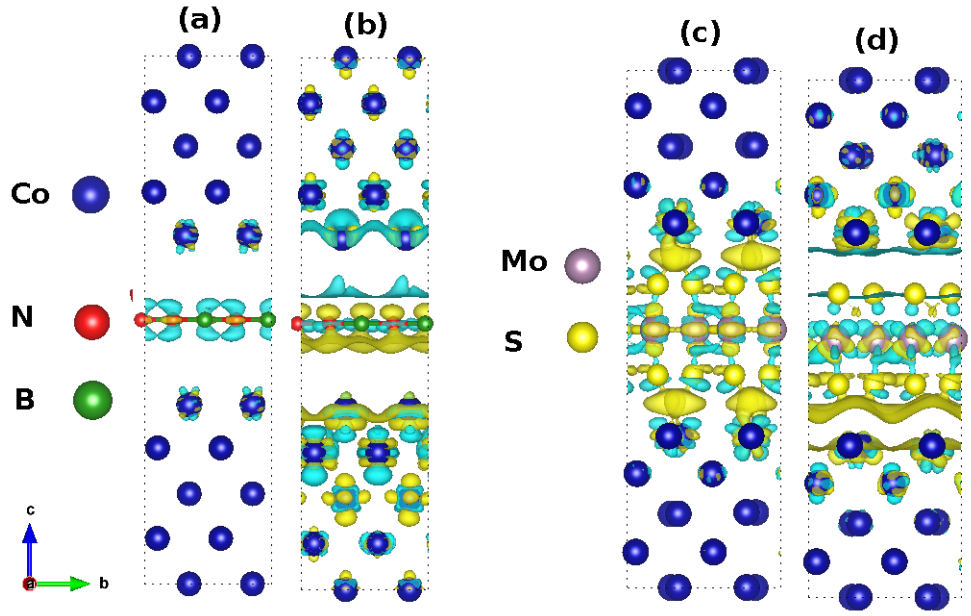

Figure 5.13: Charge density difference for a system including (left panel) monolayer hBN, and (right panel) MoS_2 tunnel barrier with an applied electric field of amplitude (a,c)0.0, and (b,d) 0.1 a.u. Yellow and cyan denote electron accumulation and depletion regions, respectively [2].

Figures 5.13(c) and (d) display the $\triangle\rho(r)$ for Co(111)/MoS_2/Co(111) model with an isosurface of 3×10^{-3} e/Å^3. These show a large density of charges in the region between Co-S bonds. Fig. 5.13(c) exhibits a large collection of charges on the

Co-S bonds even without the applied field. The charge collection zones demonstrate an electronic shadow formed in the tunnel barrier region. This is shown in yellow in the interface and suggests that this area is full of electrons as the field intensity is increased to 0.1 a.u. The top interface becomes a low electron-density region (i.e., full of holes). due to the the deficit charge density. The aggregation of charge density creates a localized surface zone in the top interface, while the bottom interface forms a wave-like pattern as shown in Fig. 5.13(d).

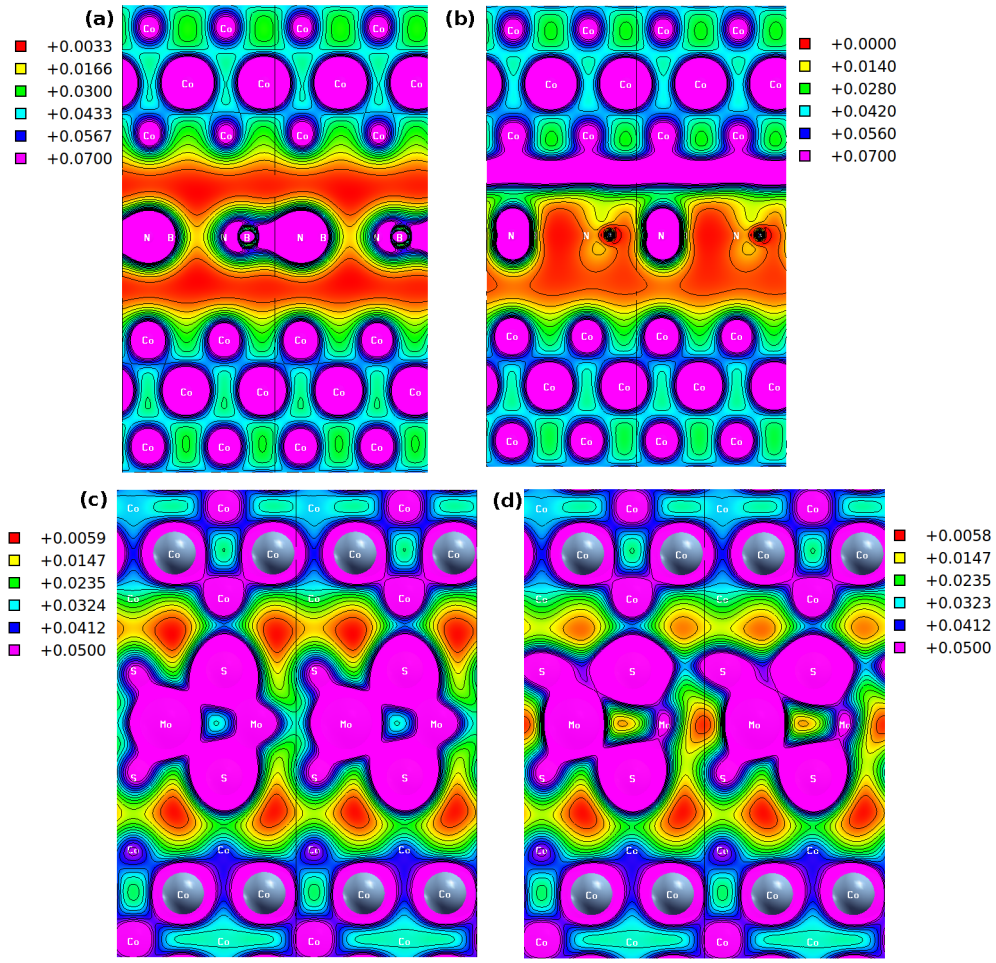

Figure 5.14: Contour plots of the total (volumetric) charge density distribution of a long [110] plane as a function of applied electric field intensity for the heterostructures of Co(111)/hBN/Co(111), in the top panels, and Co(111)/MoS_2/Co(111), in the bottom panels. The intensity values of 0.0 and 0.1 a.u. were applied in (a) and (c), and (b) and (d), respectively [2].

Figure 5.14 depicts the total charge density (CD) along the [110] plane as a 2D projection. There is a weak localization of the CD in the region between Co(111)

and hBN. This weak charge density localization represents 4% of the highest charge density found between the B-N bond in the interface [see Fig. 5.14(a)]. This is similar to the low CD region discovered between Fe(110) and hBN in graphene/hBN heterobilayer [192]. Fig. 5.14(b) displays the volume charge density at a field of 0.1 a.u. for Co(111)/hBN/Co(111) heterostructure. This alternating domains are associated with the proximity effect in the symmetric magnetic tunnel junction considered herein.

Figure 5.13(b) exhibits a broad line with no charge density region surrounding the reservoirs of heightened local CD with the hBN based barrier. This charge carrier arises via location hopping in the half-metallic phase. Even though the electric field breaks charge symmetry in the ground state, it introduces a neighbouring region of elevated charge density on one part of the interface. This form of charge distribution leads to a metallic state. An analogous transport medium for carriers through a nano-line of carries is not found in the MoS_2 barrier model. Thus, It is concluded that the electric field creates a toggling control of the CD. Figs. 5.14(a) and (b) also indicate that the applied electric field emerges in locations with high CD in the ion cores. This suggests the existence of an electric dipole via an interface. Figs. 5.14(c) and (d) demonstrate complementary CD with MoS_2 distinguished by lower CD sites at the interface. Overall, the applied field has a negligible effect on the CD relative to the ground state allocation.

5.2.4 Effect of applied electric field

Spin conductance

Mesoscopic physics addresses the interpretation of ballistic transport in condensed matter, one notable finding of mesoscopic physics is quantum conductance (QC) [255]. The goal is to gain insights into the influence of the electric field on the spin quantum conductance (QC) behavior of multilayers heterostructure, for parallel (P) and anti-parallel (AP) magnetic configuration as presented in Tables 5.2 and 5.3.

Table 5.2 illustrates the spin conductance (SC) when hBN is the barrier. At

all intensities of applied fields, the SC of the P configuration is higher than the SC of the AP, implying an extensive resistance to transmission in AP configuration. The excess spin dispersion increases the resistance due to the chiral anomaly in the Fermi level topology in the majority and minority spin domains [191]. This creates an imbalance in the spin population around the Fermi level. This manifests in spin conductance coefficient in the P(AP) configurations under varying electric field intensity. For instance, the spin conductance is 0.0001 (0.00004) Ω^{-1} for P (AP), respectively. This is an attribute of the more high spin transmission in the P orientation. However, the AP states conductance increases at a high field of 0.3 a.u. than the P states.

Table 5.2: Effect of electric field on the SC of the Co(111)/hBN/Co(111) heterostructure.

Electric	Field	Parallel			Antiparallel		
(a.u.)	10^{10} (V/m)	$T^{\uparrow}$	$T^{\downarrow}$	$G^{\uparrow\uparrow}$	$T^{\uparrow}$	$T^{\downarrow}$	$G^{\uparrow\downarrow}$
0.0	0.0	0.27284	0.93178	4.66	0.3192	0.2987	2.394
0.01	0.51	0.25774	0.71976	3.79	0.3944	0.3053	2.71
0.1	5.14	2.014	0.74109	100	0.8513	0.2284	4.183
0.3	15.43	0.03491	0.0000063	0.135	0.3801	0.2963	2.621

Table 5.3: Effect of electric field on the SC of the Co(111)/MoS_2/Co(111) heterostructure.

Electric	Field	Parallel			Antiparallel		
(a.u.)	10^{10} (V/m)	$T^{\uparrow}$	$T^{\downarrow}$	$G^{\uparrow\uparrow}(\times 10^{-5})$	$T^{\uparrow}$	$T^{\downarrow}$	$G^{\uparrow\downarrow}(\times 10^{-5})$
0.0	0.0	0.9103	1.087	7.730	0.688	1.65	9.08
0.01	0.51	1.321	1.18	9.695	0.4356	1.417	7.17
0.1	5.14	0.1795	1.82	7.748	0.24	0.2611	1.94
0.3	15.43	0.0849	0.00853	0.3622	0.0051	0.00346	0.0333

For the MoS_2 based tunnel barrier, Table 5.3 shows a relatively decreasing spin conductance. It is vital to highlight that the spin transmission coefficients for the majority and minority spin states are coupled to the spin polarization P the following equation:

$$\eta = \frac{\left(T^{\uparrow}(E_F) - T^{\downarrow}(E_F)\right)}{\left(T^{\downarrow}(E_F) + T^{\uparrow}(E_F)\right)}. \tag{5.2}$$

On the other hand, for the hBN barrier model, the spin transmission coefficient is 2.0 (0.74) e^2/h for the majority (minority) spin transmission. This was employed to get spin polarization (η) of 46% in the P spin orientation. In the AP spin states, the computed spin polarization is 57%. Then the polarization increases to 99% in the P state with the electric field increasing, but it drops to 11% in the AP state when the field is increased to 0.3 a.u.

For pMTJ-based on MoS_2, the spin transmission is higher in the absence of an external field. Its metallic carrier transport character is dominated by the spin down states ($T^{\downarrow}$) for both P and AP spin configurations. Using 1.32 (1.18) e^2/h for the majority (minority) in the P state, respectively, a small polarization of 5% is obtained. By contrast, 62% is achieved in the AP state. Also, at 0.3 a.u, the polarization increases to 82% in P-alignment and 19% for AP-alignment in both channels.

Spin-dependent transmission spectra of Co/monolayer/Co

In this section, presents the transmission spectra of both models of pMTJs as the function of energy E for P and AP spin orientations. Figures 5.15 and 5.16 demonstrate the evaluation of transmission via an applied electric field. Figure 5.15 displays the transmission spectra of pMTJs based on hBN as a tunnel barrier. At zero-field, the minority spin dominates the transmission for P (Fig. 5.16(a)), with the same trend at the field of 0.01 a.u. in Fig. 5.16(b). In contrast, in AP (Fig. 5.16(e)), both spin channel conductance is almost equal. At the higher strength of the field 0.1 and 0.3 a.u., the spin flipped the domination of spin states at E_F from minority to majority (see Fig. 5.15(c) and (g)). In addition, the transmission propagation of spin-up $T\uparrow$ at E_F (2.0) is more heightened than the spin-down (0.74) in the P configuration.

On the other side, Fig. 5.16 illustrates the transmission spectra when the MoS_2 is a barrier. Again, at zero fields, the transmission is high and governed by the minority spin $\downarrow$ for P and AP magnetic arrangements (Fig. 5.16(a,e)), suggesting a metallic nature. However, at 0.01 a.u., a significant evolution occurred in which

the conductance of P configuration is dominated by the majority spin ↑ [see Fig. 5.16(b)], and the transmission of majority (minority) spin is 1.32 (1.18). Contrary to AP, which is dominated by minority spin. At a higher field intensity of 0.3 a.u., the majority spin competes with the minority with greater conductance and exhibits considerable polarization. Opposite, in APC, the $T(E_F)$ values for the spin channels are almost matching and have a slight transmission probability (0.005 vs 0.003) as in Fig. 5.16(h). Therefore, these results coincide with Tables 5.2 and 5.3 and demonstrate the response of pMTJs to the applied electric field with changing magnetization directions. The spin-flip in the Fermi level was also seen in Figs. 5.15(c) and 5.16(b) to result in varying the values of TMR and polarization as well.

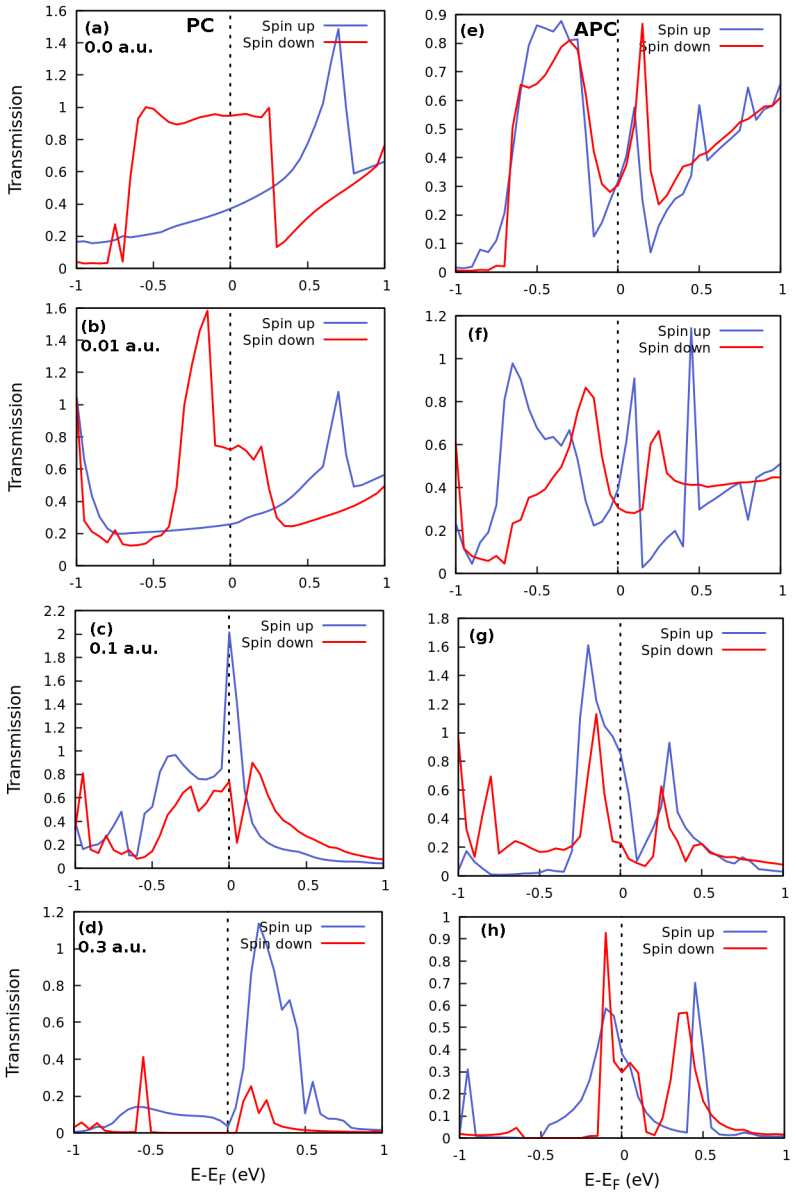

Figure 5.15: Electric field dependent transmission spectra of Co(111)/h-BN/Co(111) junction in the P (left panels), and AP configurations (right panels), around the Fermi level for the spin-up (blue color) and spin-down (red color) channels at field magnetitudes of (a,e) 0.0, (b,f) 0.01, (c,g) 0.1, (d,h) 0.3 a.u., respectively The vertical dashed lines indicate the Fermi level (E_F).

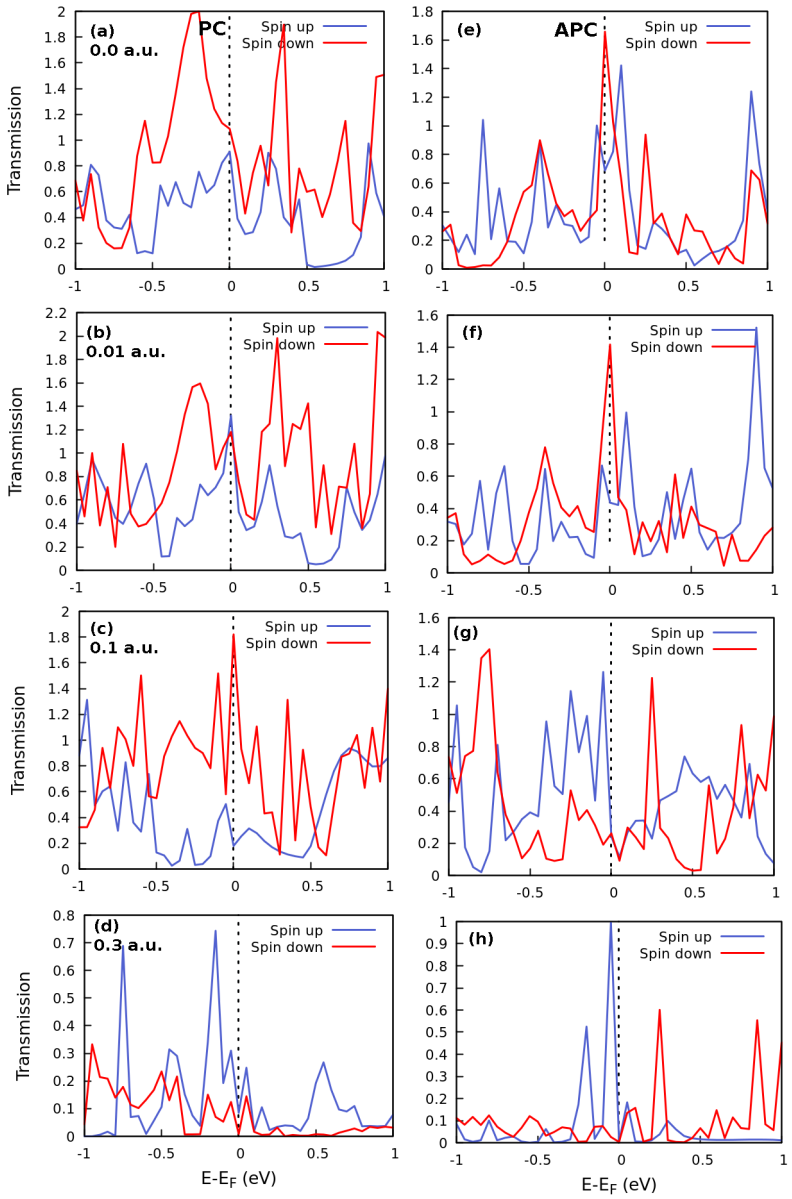

Figure 5.16: Electric field dependent transmission spectra of Co(111)/MoS_2/Co(111) satck in the P (left panels), and AP configurations (right panels), around the Fermi level for the spin-up (blue color) and spin-down (red color) channels at field magnetitudes of (a,e) 0.0, (b,f) 0.01, (c,g) 0.1, (d,h) 0.3 a.u., respectively The vertical dashed lines indicate the Fermi level (E_F).

Tunneling magnetoresistance (TMR)

The concept behind the emergence of the TMR is spin-dependent tunneling. Where the electrons of the spin-channel can exclusively tunnel into a specific spin channel [256]. Figure 5.17 shows the magnetoresistance for two different barriers model. At zero bias, the TMR is 94.95% when hBN is a barrier in the vertical stack (see Fig.

5.17(a)). The applied field remarkably fluctuates the computed TMR, especially at 0.1 a.u. The TMR achieve the highest value of 139.06% due to the extensive spin transmission coefficient discovered in the spin-up states of the P magnetic orientation. Since the TMR is positive when the electrodes are constructed with the same material [257]. The discovered drop to -94% at a field intensity of 0.3 a.u. in Fig. 5.17(a). Attributed to the magnetoelectric effect is the larger magnitude of the quantum conductance in the AP (2.621) than in P (0.135) spin states. Also, this negative value conforms to the actual one depending on the asymmetric bias. This behaviour is different from the class of barriers used. Also, the spin transmission becomes sensitive at the interface due to the bond mechanisms at the lead/barrier interface. The results reveal that the critical electric field yields quantum phase transition when hBN is a barrier analogous to the field strength where the TMR arrives at the saturation region.

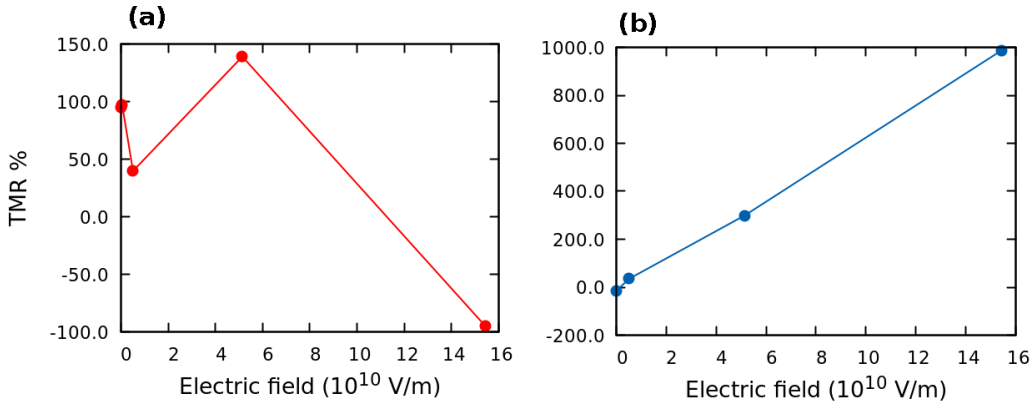

Figure 5.17: The evaluation of tunneling magnetoresistance for monolayer tunnel barrier based on (a) hBN, and (b) MoS_2, at different magnitudes of an electric field [2].

On the other hand, Fig. 5.17(b) exhibits a high TMR of 299.09% when MoS_2 as tunnel barrier at the critical field (0.1 a.u.). It is evolved to 987.02% at an intensity of 0.3 a.u. These results agree with Dolui et al. [252], they discovered a colossal magnetoresistance of 300% in the Fe/MoS_2/Fe system. In this work, the exotic increase in the TMR is due to an additional efficient spin-filter influence in the AP-alignment.

Generally, the dependence of the calculated TMR on the electric field for different tunnel barriers of the symmetric pMTJ [see Figs. 5.17] are in good agreement with those studied with symmetric regions of MoS_2, and hBN [258]. Inserting either hBN or MoS_2 as the tunnel layer in the vertical stack shows perfect spintronic performance due to the high TMR discovered: 139% (987%) for hBN (MoS_2), respectively. This shows effective modifications compared with the TMR calculated of the oxides barriers Al_2O_3 with the same Co leads [256, 259].

The wave-vector $k_{\parallel}$ resolved transmission

To gain insights into the magnetic coupling and the electric character of pMTJs and TMR, k-space-resolved spin transmission spectra within the 2D BZ at the critical field intensity were computed. Figure 5.18 displays the wavevector dependency for the spin channels (up and down) in the P-alignment and AP-alignment in the contour maps.

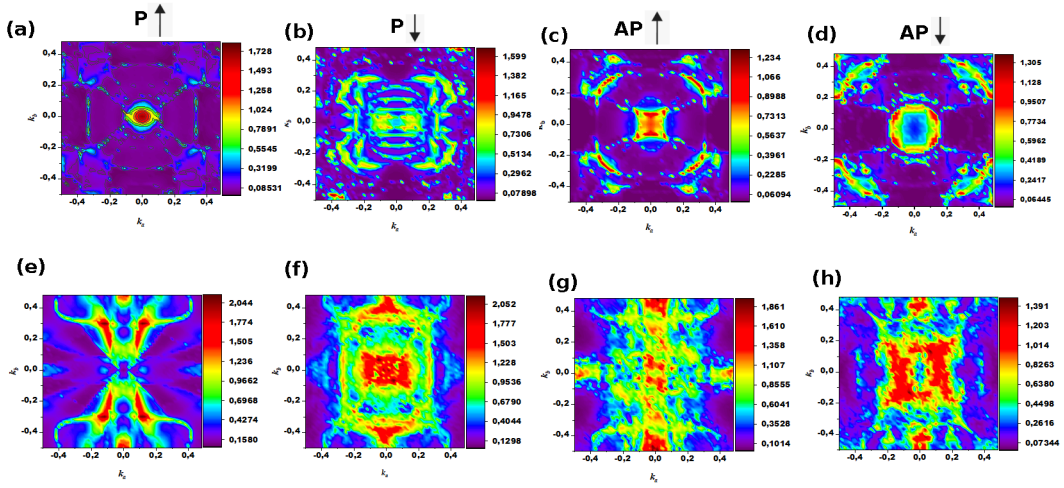

Figure 5.18: $k_{\parallel}$-resolved spin transmission spectrum at the critical field. Co(111)/hBN/Co(111) in the top panel, and Co(111)/MoS_2/Co(111) in the bottom panel. For the (a,c,e,g) majority, and (b,d,f,h) minority spin states in (a,b,e,f) parallel (P), and (c,d,g,h) antiparallel (AP) configurations, respectively, [2].

In pMTJs based on hBN, the results demonstrate that the majority-spin of Co/hBN/Co stack (top panel) in P and AP arrangements govern the transmission spectra comparative to the minority-spin as shown in Fig. 5.18(a). Obviously, from

the colour scale, the high intensity peaks emanate from the middle of BZ at the Γ-point. This confirms that majority-spin has high transmission than minority-spin. Although for P-alignment, the spin-up transmission in the middle of BZ arises due to a robust coupling between occupied and unoccupied states of Co *d*-orbitals in spin-down. This is also in a good agreement with conductance in Tables 5.2 and 5.3.

Nevertheless, for AP-alignment, the transmission spectra correspond to the majority (minority) spin, being strong (weak), close to the centre of BZ. This compromises the spin-polarized charge density values of Co-atoms at the interfaces (see Fig. 5.14(b)). In AP-alignment reveals the tiniest donations from carriers at the AP in the corners and edges of BZ. From Fig. 5.18(c), the high density emanates from the centre. However, the transmission of spin-down in Fig. 5.18(d) is characterized by low density (in blue) in the middle of BZ covered by high density. There is a different scenario for pMTJs based on the MoS_2 in the bottom panel, especially the transmission of P-alignment. The spin-down electrons have a higher transmission than the spin-up (see Figs. 5.18(e) and 5.18(f)). A high density characterizes the Γ-point. This differs from the majority spin, where the high density emanates away from the centre of BZ. In AP-alignment, both spin channels are described by high transmission spectra in the middle of the BZ and near the gamma-point.

Carrier transport phase diagram of the Co/hBN/Co model

Quantum phase transitions (QPTs) are fundamental features that insight into the nature of the condensed matter system at the ground state. Herein, the spin flip energy is used as the probe of quantum phase transitions in the transport phase of carriers. The spin-flip energy (E_{sf}) as used in the phase diagram defines a non-thermal control parameter to drive quantum phase transition by quantum fluctuations rather than thermal fluctuations. It is equal to the metric of the non-local order of the Landau theory. The spin-flip energy has been computed as the distance from the Fermi level at 0 eV, and the valence band maxima [260]. Figure 5.19 shows the transport signature phase diagram when hBN is a barrier in the system.

The results reveal a trivial transition in the carrier transport phase at a field strength of 0.1 a.u. This denotes the critical point of the applied field. Also, there is a drop in the spin-flip energy while electric field intensity increases to the quantum critical point (QCP). The spin flip energy disappears beyond QCP. The critical field where the first-order QPT occurs reveals an abrupt quantum transition from half-metallic to metallic phase at the ground state.

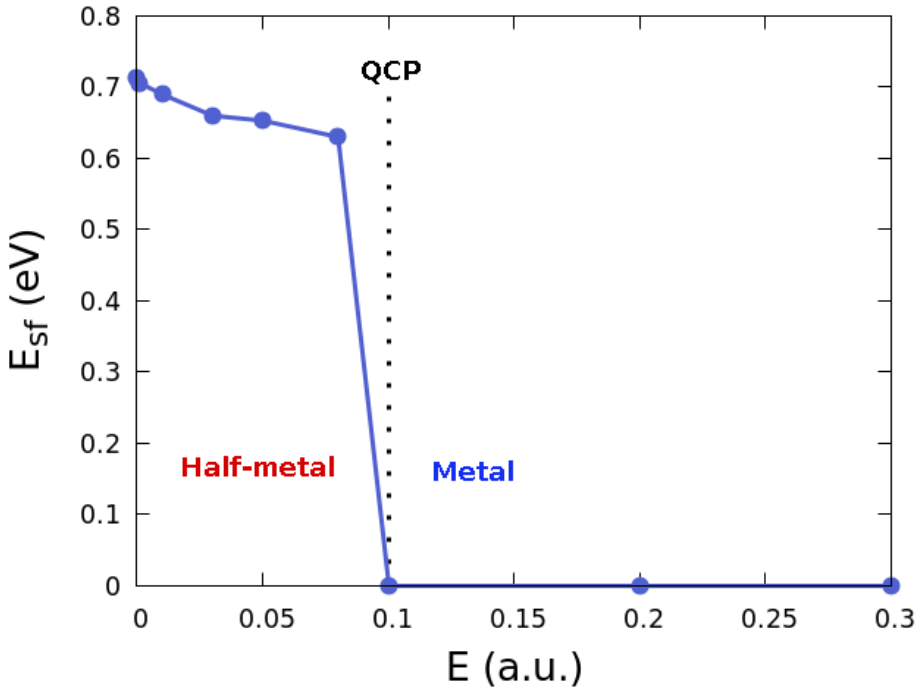

Figure 5.19: Electric field-induced carrier transport phase diagram of pMTJs based on hBN. The vertical dashed line denotes the quantum critical point [2].

The quantum critical point is found to occur at E = 0.1 a.u. This is because E= 0.1 a.u. is the only point in the spin-flip energy versus applied electric field plot [see Fig. 5.19] wherein the applied electric field has induced the gapless transport state in the monolayer hBN-based heterostructure. This effect is observed in the spin-up channel of the Co(111)/hBN/Co(111) heterostructure as a change in the quantum transport state of the system from a half-metallic to a metallic phase. For instance, the calculations have been repeated for the magnitude of the applied electric field of 0.09 and 0.095 a.u, respectively. The results are shown in the Figure 5.20. These results show a gap in the spin up channel of the projected density of states at both E=0.09 and E=0.095 a.u. This observation confirms the validity of

the above assertion. All the other values of the applied electric field before E=0.1 a.u. give rise to a finite band gap in the spin-up channel while all the values of the applied electric field beyond 0.1 a.u. give rise to the "gapless" state expected in metallic transport of carriers.

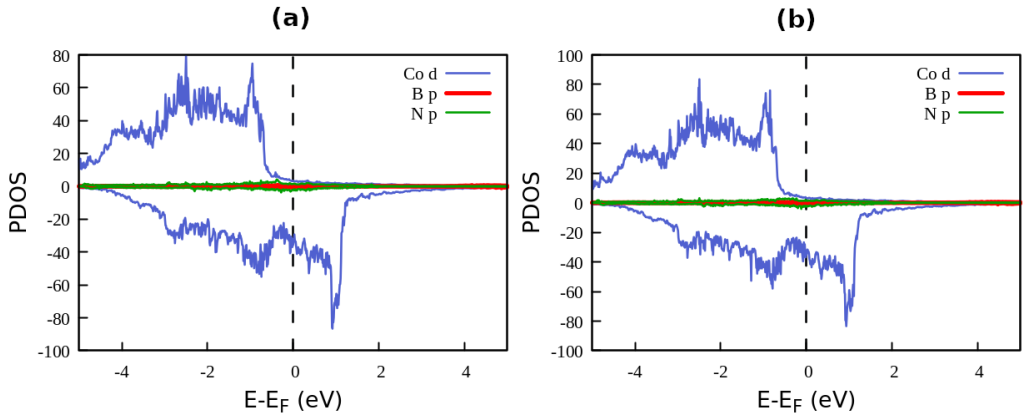

Figure 5.20: Projected density of states for Co(111)/BN/Co(111) stack at (a) 0.09a.u. and (b) 0.095a.u., respectively.

In Ref. [1], a facile electronic switch between trivial and topological quantum phases was discovered via the normalizing electronic structure of the bulk to the 2D model on the honeycomb lattice. Moreover, the effect of applying a magnetic field to the artificially-stacked multilayer heterostructure leads to the appearance of magnetic skyrmion spin textures [261]. The Coulombic exchange between the two magnetic electrodes with a monolayer barrier layer creates a symmetry-breaking mechanism. Due to first-order perturbation in the electronic states, proximity effects are induced [262, 263]. Consequently, when an external field is applied to van der Waals heterostructures (or to magnetic tunnel junctions), it modulates the time-evolution of electronic density oscillations. This is the mechanism that leads to collective excitations [264–266]. Such excitations include the charge density wave (CDW) phase at a specific region of the QPT, a spin-polarized CDW phase, and the formation of robust quasiparticles and spin texture [1, 191, 261].

5.3 Light-matter interactions

5.3.1 Emergent electrodynamics: Plasmonic responses

The coupling between light and matter forms collective excitations. Bosonic excitations such plasmons intensely affects the optical properties of the nanoparticle system. However, non-linear properties arise as an electromagnetic field (EM) response at specific QPTs energies in Dirac materials. Emergent properties originate from the interaction between the EM field and chemical bonds. These collective properties can be understood from the systematic analyses of the interband optical transitions obtained relative to the ground-state electronic density. This phenomenon can be described within electromagnetic theory by solving Maxwell's equations [267]. The contributions from the photon absorption spectrum to comprehend these optical reactions are due to the distinct intensities determined in the photoabsorption spectra analyzed. The results demonstrate wave-like interference patterns as the field response of an electronic structure and transportation signature.

The model material used herein to observed and characterize the emergent quantum transport phases is based on the computation performance of low-dimensional DMs systems. Such as nanoclusters and nano-line for TaAs and graphene, respectively. Instead of their bulk systems. This computational technique permits perspicuity into the plasmonic characters from DMs optronics reactions. The function of monolayer DMs to form van der Waals heterostructures for spintronics applications has been confirmed [261]. Moreover, modelling DMs like TaAs and graphene ensures the preservation of their edge states when geometrically reduced to their nano-size. Therefore, quantum confinement consequences evolve, and the transport signature emerges at the edges and remains topologically preserved. Manipulating edge-states ensure the intuitive formation of the topological numbers (Z_2, C) discussed in the previous section for characterizing TPDs.

Determining the upper bound of the potential for nanoparticle systems is not crucial. Instead, it is only required to determine the reference energy of the plasmonic state. It is characterized as the difference in energy between an isolated

nanocluster within an extensive vacuum area and the related Bloch state. The difference between the eigenvalue in each system compared to the propagator eigenvalue in the reference dielectric system is known as binding energy. Its calculations have been tested based on gold as a reference system to manipulate the light absorption at the nanometer scale for novel applications and fundamental investigation of physical system [268].

Figure 5.21 exhibits the localization of the near field enhancement intensity for nanostructure and dimer subsystems. Also, the growing in the classical (see Fig. 5.21(a,c)) and quantum (see Fig. 5.21(b,d)) regimes. The top (bottom) panels represent the field distribution for TaAs (graphene), respectively. The field strengths are calculated at the point where the topological phase transition occurred, with an energy scale of $t = 2.05$ eV. The classical subsystem of the TaAs cluster (Fig. 5.21(a)) is simulated as a spheroidal nanoparticle with a radius of 7.85 Å. However, the quantum subsystem (Fig. 5.21(b)) indicates the dimer of Ta-As with an interatomic space of 2.62 Å. The emergence of the enhancement of the EM field intensities around subsystems nanostructures. It is attributed to the coupling between the incident photons and the collective fluctuations of free carriers at the surface. The results demonstrate identical growth of the field intensity for both nanostructures (TaAs and graphene). Correspond to the equivalency of the electronic structure renormalization as the system's shape expansions.

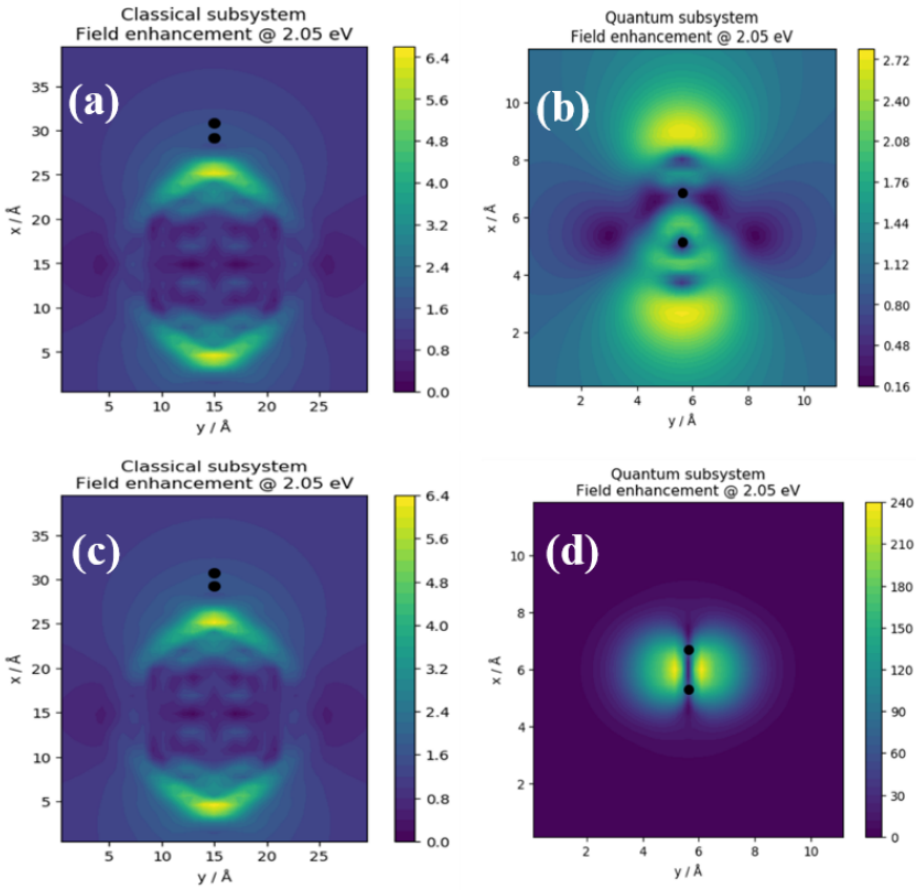

Figure 5.21: Local distribution of field enhancement in the (a,c) Classical, and (b,d) Quantum subsystems for TaAs (top panels) and graphene (bottom panels). The color bars denote the field enhancement in Volts/Å [1].

The classical and quantum mechanical prototypes show non-uniform field behavior. However, the effect of the applied electric field is observable in the area close to the dimers. The absence of inversion symmetry makes the interatomic distance of Ta-As an ill-described property in the nano-line axis. So the structure of TaAs nano-line is hard to benchmark and to simulate because it is dissimilar to the carbon nano-line model. Hence, it is reasonable to elucidate the differences observed in the profile of the induced potential from the quantum subsystem of the carbon system for comparison with the Ta-As. These analyses are based on the assumption that there is a uniform distribution of carrier density near-atomic cores. The C-C bonds exhibit a substantially increased volumetric carrier density due to the effect of the field in the graphene system.

The analysis of the two quantum subsystems demonstrates that the order of magnitude of the field enhancement in the classical subsystem is compatible. The field enhancement in the corresponding quantum subsystem of the graphene is one order of magnitude stronger than in the TaAs. The impact of the field enhancement leads to regions of high and low intensities near the atoms of the dimers, even at a low absorption kick of 10^{-5}. Therefore, once TQPT has emerged, a shift in field strength does not vary the ordering of the topological electronic phase. Figures 5.21(a,b) exhibit significant field enhancements at the edges of the nanoparticle as characterised by the yellow region. Since the field lines commonly construct uniform boundaries, the observed outwards divergence of the equipotential surfaces from the boundaries in both the quantum and classical subsystem suggest that the nanoline is behaving like a dipole configuration when subjected to an electric field. Consequently, the nanostructure core acts as a sink of field lines.

By contrast, the response of the quantum subsystem to the field enhancement demonstrates differences in the interatomic distance in Ta and As atoms of the dimer (Fig. 5.21(b)) and C-C (Fig. 5.21(d)), respectively. Remarkably, the field modes in the two dimers show two different characteristics due to the asymmetric charge distribution between the Ta-As dimer (see Fig. 5.21(b)). In Fig. 5.21(d), the field enhancement shape close to the C-C atom is uniform, thus maintaining carrier symmetry. It is attributed to the uniform response of the structure near the C-C dimer to the applied field. Altogether, the investigations show that the external field creates an extra field as an immediate response to the distortion of the local potential due mainly to the carrier redistribution. This redistribution of carriers induces a collective excitation mode similar to the charge density wave (CDW).

From the perspective of electrodynamics, the electric field $\mathbf{E}$ can be expressed as the sum of the electrostatic and electrodynamic contributions, such that

$$\mathbf{E} = -\boldsymbol{\nabla} V + \frac{\partial}{\partial t}\mathbf{A}, \tag{5.3}$$

where V denotes the electrostatic potential and $\mathbf{A}$ denotes the magnetic vector potential, respectively. It appears in the nano-structures of Dirac materials due to

the potential created by the field-induced volume charge density. The localization of the generated potential in the non-trivial phase is indicated in Fig. 5.22 of TaAs (graphene) in the top (bottom) panels, respectively. Again the potential in classical subsystems of TaAs (Fig. 5.22(a)) and graphene (Fig. 5.22(c)) are identical insofar as the depth of the potential and distribution of equipotential surfaces are involved. Nevertheless, small dissimilarities are observable in the distribution of regions of high and low potentials. While the spatial distribution of localized areas of potential extrema is almost alike in both systems, slight dissimilarities are again noticeable. This agrees with the strength of the field enhancement in similar subsystems.

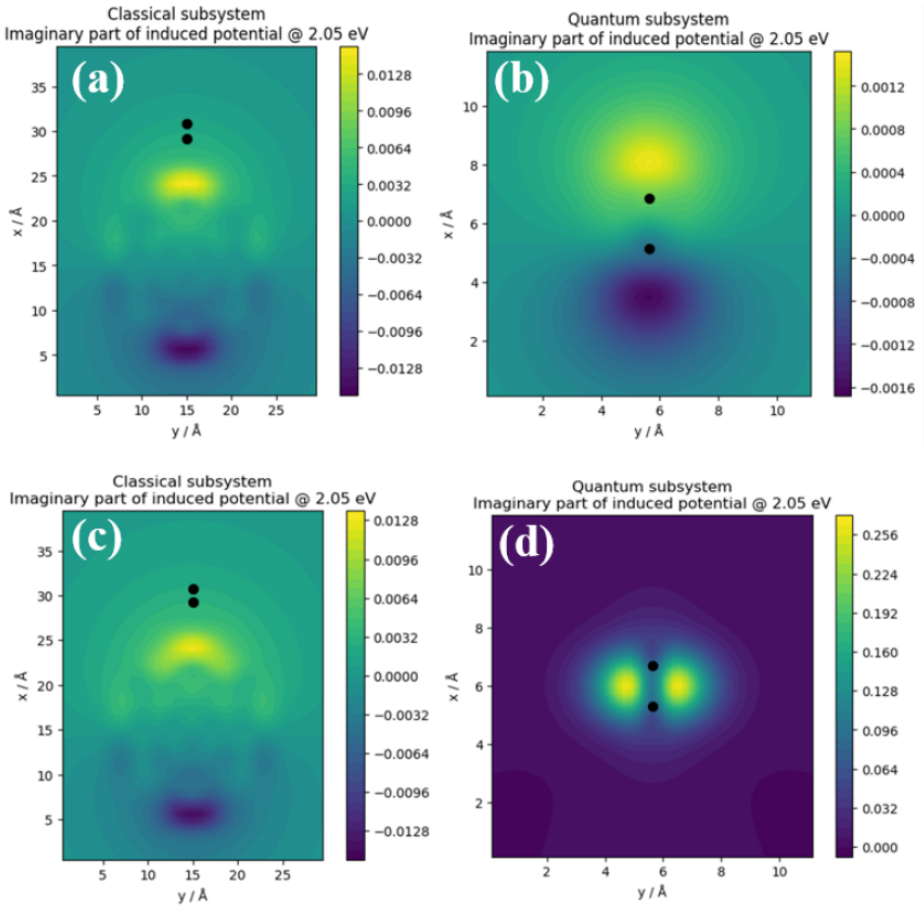

Figure 5.22: Induced potentials in TaAs (top panels) and graphene (bottom panels) for (a,c) classical, and (b,d) quantum subsystems. The color bars denote the induced potential in volts [1].

Figures 5.22(b) and (d) show the imaginary domain of the generated potential in both quantum subsystems. The results demonstrate that the generated potential

in the Ta-As dimer is less than the C-C dimer by three orders of magnitude. Also, there are two contiguous neighbouring areas of maximum and minimum potential from the atomic cores of the dimers. Notice that the applied potentials are moved along the axis of the Ta-As dimer. By contrast, the spatial location of the C-C dimer is moved out from the axis of the dimer at an angle of 90°.

Figure 5.23 illustrates the imaginary part of the generated CDW in both quantum subsystems of Ta-As (see Fig. 5.23(a)) and C-C (see Fig. 5.23(b)) dimer. The charge density allocations demonstrate high and low carrier density pockets near the atomic spots. The Ta and As atoms areas are distinguished by a high and low charge density mix. However, the axis of the C-C dimer maintains a low, but uniform charge density. The localized heightened and lower densities areas are implanted in the uniform set of disappearing carrier density, especially at large radial distances away from the dimers. However, a detectable fluctuation in the carrier density is noticeable near the Ta and As atoms of the dimer. By contrast, this is not observed in the C-C dimer.

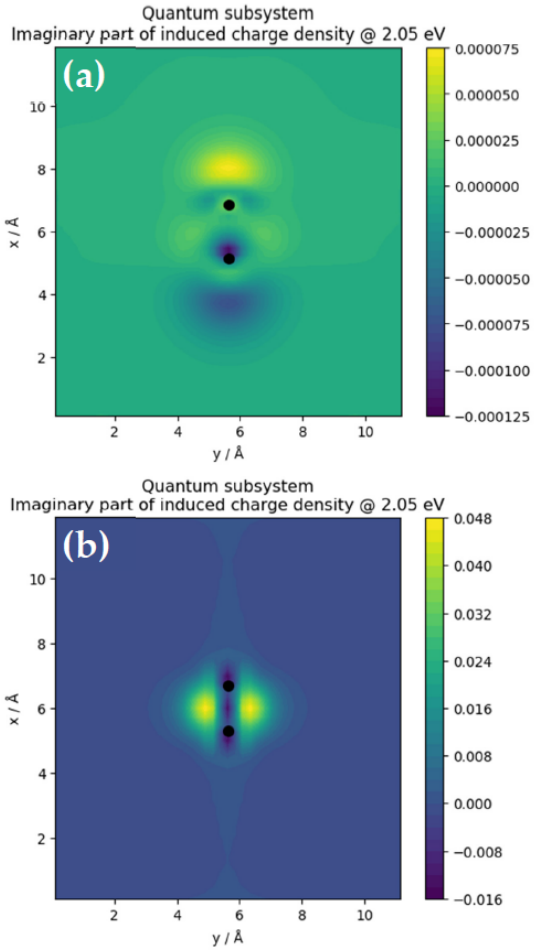

Figure 5.23: The imaginary part of the induced volume charge density in the quantum subsystems of (a) Ta-As, and (b) C-C dimers, respectively. The color bars denote the induced volume charge density in Coulombs/Å^3 [1].

Fig. 5.23(b) shows that a charge density of low magnitude is localized along the axis of the C-C dimer. The two localized areas of significantly higher charge density are found to be contiguous to the bond axis, as if their coordinates have been rotated by an angle of 90° through the center of the C-C bond length. Therefore, a continuous induced potential is anticipated as the charge accumulates. The charge deficient areas are uniformly spread near the dimer cores. The coordinate and uniform distribution of the induced charges in both systems suggest that a little excess work must be done on the individual structure to induce transport dynamics in the topological quantum phase.

Figure 5.23 also shows how the collective excitation, such as the plasmon re-

sponse of the nanostructure, originates from the vibrational modes of the chiral edge when Dirac materials are incorporated into a nano-junction. The results reveal the similarity of carrier modes in both subsystems due to the high charge density that surrounds the atom cores. This proposes an existence of a large limit between the local geometries of the Ta-As and C-C dimers, in which the electrodynamic responses of both subsystems will agree. The observed warping in the electrostatic potential of DMs signifies that carrier transportation will also depend on additional potential wells and barriers at the TQPT point. It is therefore expected that an externally applied field will not necessarily lead to a symmetric transportation of charges on the surface of the DM in the region of the topological phase diagram wherein TQPTs are expected to occur.

Some investigations of the plasmonic reaction of metallic nano-junctions have demonstrated a complete correlation between the spectral positions of the dominating resonance in the collective excitation and the imaginary part of the induced volume charge density distribution that generated the CDW with unique excitation frequencies [269]. Herein, it is found in the quantum subsystem, that the plasmonic responses agrees with the results of Fukuoka and Tanabe on similar nanostructures [270]. The agreement is due to the substantial enhancement of the EM field energy in the area encircling the nanoclusters to the distinctive character of plasmons. Correlation of the plasmonic state with the quantization of charge (or spin) transport suggests that the lightning-rod effect causes the mechanism at the atomic scale [271]. It is a character of the field enhancements (see Fig. 5.26). Accordingly, the formation of facile plasmons in van der Waals heterostructure stacks are expected. This is attributed to the induced potential gradients in the quantum subsystems (Fig. 5.25) as a result of the existence of heterobilayer interfaces.

5.3.2 Optical photoabsorption spectra

To get a deep understanding of electronic systems, the optical absorption spectra were analysed. It is one of the conventional methods of connecting the results of theoretical and experimental studies [272]. The computational modelling is based

on time-dependent density functional theory (TDDFT) within periodic boundary conditions. Figure 5.24 depicts the dependency of the optical photoabsorption spectra on the local structure of the two materials obtained by setting the probability distribution Gaussian at a width of 0.1 eV. Figures 5.24(a,b) represent the photoabsorption spectrum of the C-C dimer and bulk graphene system whereas Fig. 5.24(c,d) exhibit the identical spectra for TaAs. The photoabsorption shows some of the incident radiation absorbed by the material within the indicated range of energy. The emergence of peaks at 4.2 eV (see Fig. 5.24(a)) and 9.4 eV (see Fig. 5.24(c)) implies that optically generated transitions occur at those energy points between the valence and conduction band states. This forms exciton (electron-hole pair) in a similar manner to the quantum dots. Also, the fluctuating peaks suggests the possibility of intense absorption of radiation by the C-C dimer at the lowest energy of 4.2 eV. This corresponds to the relatively lower absorption of Ta-As dimers at high energy of 9.4 eV.

However, Fig. 5.24(b,d) shows a broad absorption spectrum of the bulk structures. These show a dominant peak at an energy of 9.96 (8.9) eV for TaAs (graphene), respectively. The inadequate resolution of the prevalent cluster peaks in the photoabsorption spectra of bulk structures is a fascinating nonlinear optical phenomenon. For instance, the location of the main peak in the spectra of both bulk structures is well-resolved in the nanocluster spectra. These seem like low intensity peaks that appear more reduced in the TaAs system than graphene due to the effect of quantum confinement. The poor resolution of the absorption peaks in the clusters is ascribed to the effects of quantum confinement, which causes the widening of the peaks in the bulk structure. It is reasonable that the reverse impact causes the sensitiveness of the measured bandgap to the dimension of the nanoparticle.

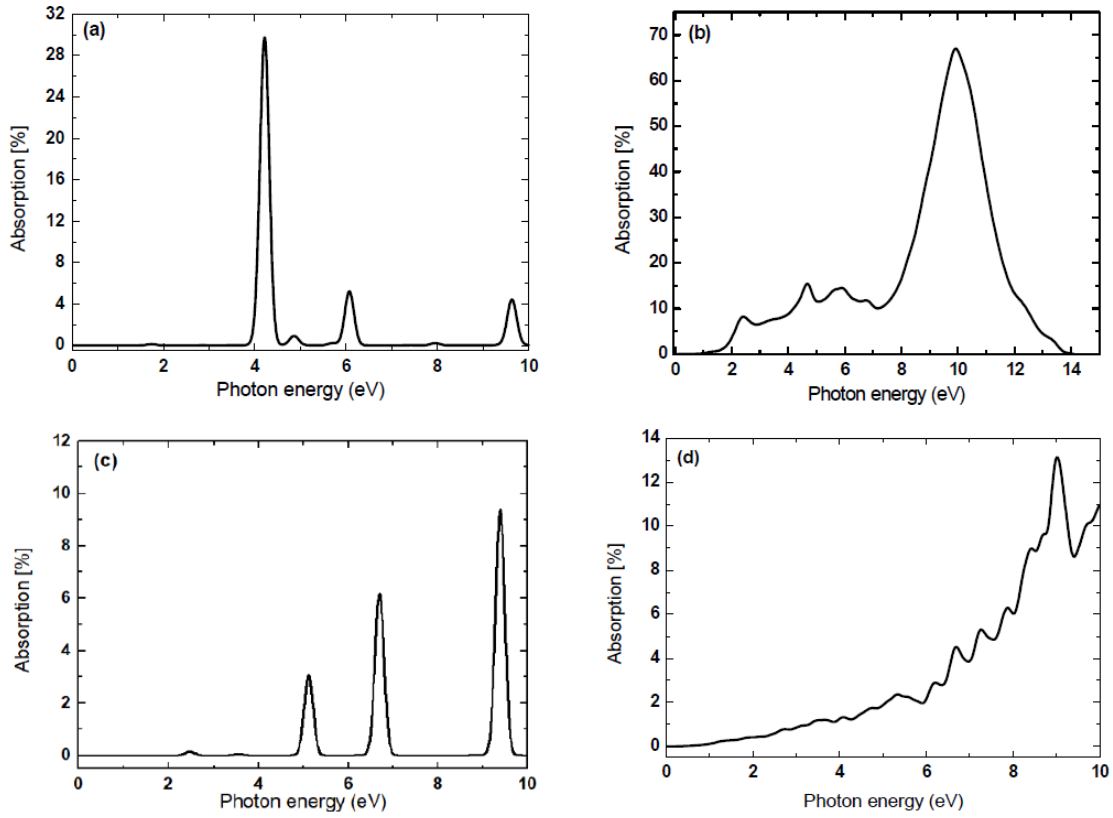

Figure 5.24: Optical photoabsorption spectra of (a) the sp^3-hybridized C-C dimer, and (b) the carbon nanoline. (c) The absorption spectrum for the Ta-As dimer, and (d) the TaAs nanocluster [1].

Despite the difference in the chemical composition between TaAs and graphene structures, their ground state at zero field is characterized by a gapless electronic state. Nevertheless, the semiconducting transport phase is characterized with a narrow bandgap. This arises from the precise mix of external perturbation fields and the intrinsic SOC. The first absorption maxima in Figs. 5.24(a)-(d) denotes electronic transitions from the valence to the conduction bands leaving behind a hole, which can combine with an electron to create an exciton (electron-hole pair). The photon energy of the first absorption maxima approximately corresponds to the width of the bandgap. Again, the discontinuous peaks in Fig. 5.24(a,c) suggest that extra transitions from the bound e-h pairs must emerge. This argument also holds because the C-C dimers exhibit little absorption peaks at energies of 1.74 and 7.96 eV in (Fig. 5.24(a)), and 2.44 and 3.68 eV in (Fig. 5.24(c)).

A precise quantum mechanical understanding of the optical absorption peaks

obtained in the previous section can be achieved by reviewing the transition contributions maps (TCM) of Kohn-Sham (KS) eigenvalues between electron-hole (e-h) transitions. Figure 5.25 displays a composite plot of the DOS and the optical TCM at particular energies in the photoabsorption spectra of the graphene system. The TCM demonstrates two separate DOS. This corresponds to one each for whole electronic states as seen in the top spectra, and the unoccupied states as in the right spectra for photoabsorption peaks at energies of 1.74 and 9.65 eV in Fig. 5.25(a), and 2.44 and 3.68 eV in Fig. 5.25(c). The spectra for both total electron (e) and hole (h) states are constant under various photoabsorption energy showing that the DOS of the carrier is not sensitive to the photon absorption.

The analysis TCM shows that any peak in the absorption spectra contains numerous single-particle transitions between e-h states. The hole (h) formation is from the Fermi level at 0.0 eV transition to the highest occupied valance band, about -3.0 eV. Moreover, the carriers are formed from the lowest unoccupied conduction band up to nearly 1.75 eV. In this broadened energy range, just carbon p-states are dynamic, and the complete transition demonstrates no contributions from the $2s$-states of carbon. Also, the number of h-states is more elevated at 9.65 eV, corresponding to the 1.74 eV. There is a net depletion of electron density at the Fermi level for the low-energy absorption, whereas there is an excess at 1.75 eV. Nevertheless, at 9.65 eV, the TCM does not exhibit any collective dipolar fluctuations since the excess density vanishes.

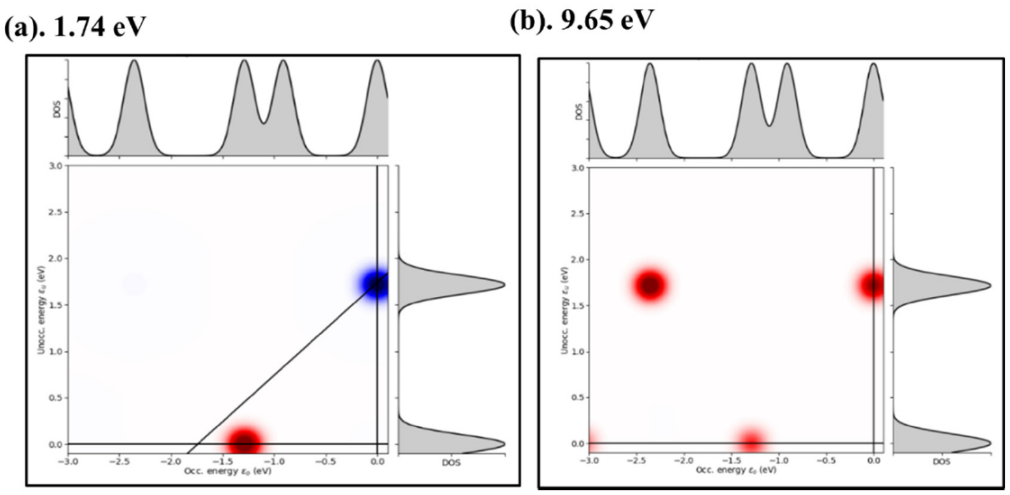

Figure 5.25: Electronic density of states combined with the optical transition contribution map at extremal energies (a) 1.74 eV. (b) 9.65 eV. The blue and red colors in the photon absorption of the graphene system show lack and excess electron density, respectively [1].

5.3.3 Carrier transport through the quantum fluid phase

Features of the near-field quantum electrodynamics in the TQP are characterized to identify an ordered quantum fluid phase. Figure 5.26 illustrates the formation of carrier density wave (CDW) through the carbon nano-line at the particular energies in the photoabsorption spectra. The results show the symmetry of the emergent field near the nano-line (1D) atoms. It is characterized by high (blue) and low (red) carrier intensities. These carrier intensities suggest a distinctive non-linear optical character in the TQPT point, like a quantum fluid phase. This gives rise to the dynamical concept affecting electrons hopping around atoms. The driven electric field sets up as a stationary waveform in a familiar vibrational pattern. The intensity positions within the corraled states vary periodically with the increase in photon energy from 1.74 to 7.95 eV. The halos of the lower field are positioned close to the carbon ions located in the middle of the nano-line (see Figs. 5.26(a)-(e)).

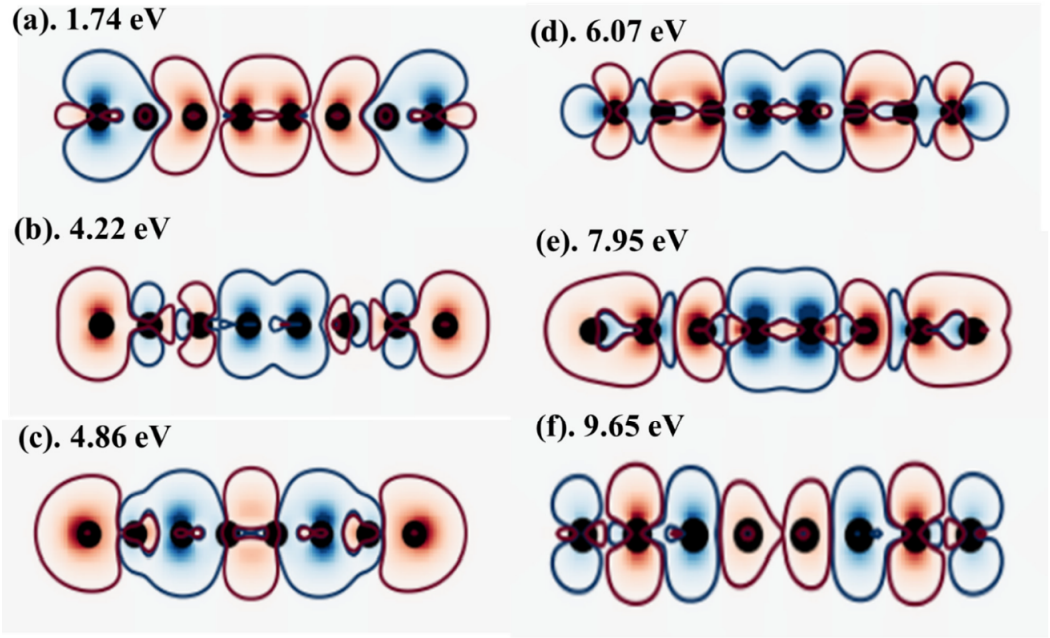

Figure 5.26: Carrier density wave of carbon nano-line at different photon energies of (a) 1.74. (b) 4.22. (c) 4.86. (d) 6.07. (e) 7.95. (f) 9.65 eV. The atomic cores are shown in black balls, while minimal and maximal carrier density (in Coulombs/Å^3) are displayed in blue and red colors, respectively [2].

On the other hand, Figure 5.26(f) reveals that at 9.65 eV, the strong field halos are positioned on the carbon atoms in the middle of the nanoline. Figure 5.26(a)-(f) unravels the intrinsic nature of a field-driven carrier density wave that is localized in the region between the carbon bonds. The resulting standing wave in the near-neighbor locations on the carbon nanoline forms a stationary charge density wave (CDW). This proposes a possible foundational basis for the transport of carriers through the CDW state in emergent applications in optoelectronics, photonics, quantum optics, and quantum computing. Since the time reversal symmetry is not preserved in the nanoline, the observed standing wave approximates the signature of the spin density wave (SDW) state whenever spin is a proper eigenstate of the system's Hamiltonian. A similar scenario is discovered in the Ta-As dimer because the induced CDW is close to the constituent atoms despite its isolated character.

Chapter 6

Conclusion

In this thesis, first-principles and tight-binding model calculations have been used to investigate the electronic ground state of bulk tantalum arsenide and graphene, respectively. Computational experiments are also performed to unravel the underlying nature of quantum phase transitions in Dirac materials using a suitably renormalized ground-state on the graphene lattice. The findings show that nanoplasmonic modes have distinct properties as an emergent response to topological quantum phases. Combining two or more fields in the tunable tight binding model of the graphene gives a rich spectrum of topological phases. This provides a theoretical foundation for experimentalists to alter the carrier states in Dirac materials by adding external fields.

Furthermore, the investigation of magnetoelectric coupling and proximity-induced phenomena may develop when an insulating monolayer of a Dirac material is inserted as the tunnel barrier layer of the perpendicular magnetic tunnel junction (pMTJ) in the ferromagnetic metal-insulator-metal multilayer stack. The response of the spin transport signatures in symmetric pMTJs to externally applied electric field show a quantum phase change from half-metallic to full-metallic phase when the model insulator material is hBN. No phase transition is observed when the insulator material is molybdenum disulphide. These observations are understood in terms of the strong hybridization of the p-orbitals of N and B atoms with the d-orbitals of Co in the interface.

Analyses of tunneling magnetoresistance demonstrate a giant signal of 987.02% (139.06%) in MoS_2 (hBN) insulator model, respectively. The strength of the applied field at the QCP coincides with an electric field magnitude of 0.1 Hatree a.u. at which the TMR reachs its maximum value. The findings provide insights into dissipative scattering anomalies in spin logic devices. This work constitutes a critical first step toward achieving a lower energy delay product performance and a faster switching operation in spintronic devices.

Bibliography

[1] M. A. Hussien and A. M. Ukpong, "Electrodynamics of topologically ordered quantum phases in dirac materials," *Nanomaterials*, vol. 11, no. 11, p. 2914, 2021.

[2] M. A. Hussien and A. M. Ukpong, "Quantum phase transition in the spin transport properties of ferromagnetic metal-insulator-metal hybrid materials," *Nanomaterials*, vol. 12, no. 11, p. 1836, 2022.

[3] A. Bandyopadyay and D. Jana, "Dirac materials in a matrix way," *Universal Journal of Materials Science*, vol. 8, no. 2, pp. 32–44, 2020.

[4] A. K. Geim and I. V. Grigorieva, "Van der waals heterostructures," *Nature*, vol. 499, no. 7459, pp. 419–425, 2013.

[5] N. Blomquist, "Large-scale nanographite exfoliation for low-cost metal-free supercapacitors," 2016.

[6] A. Bansil, H. Lin, and T. Das, "Colloquium: Topological band theory," *Reviews of Modern Physics*, vol. 88, no. 2, p. 021004, 2016.

[7] A. C. Neto, F. Guinea, N. M. Peres, K. S. Novoselov, and A. K. Geim, "The electronic properties of graphene," *Reviews of modern physics*, vol. 81, no. 1, p. 109, 2009.

[8] L. Janssen, I. F. Herbut, and M. M. Scherer, "Compatible orders and fermion-induced emergent symmetry in dirac systems," *Physical Review B*, vol. 97, no. 4, p. 041117, 2018.

[9] M. Bahramy, O. Clark, B.-J. Yang, J. Feng, L. Bawden, J. Riley, I. Marković,

F. Mazzola, V. Sunko, D. Biswas, *et al.*, "Ubiquitous formation of bulk dirac cones and topological surface states from a single orbital manifold in transition-metal dichalcogenides," *Nature materials*, vol. 17, no. 1, pp. 21–28, 2018.

[10] F. Liu and K. Wakabayashi, "Novel topological phase with a zero berry curvature," *Physical review letters*, vol. 118, no. 7, p. 076803, 2017.

[11] P. V. Sriluckshmy, K. Saha, and R. Moessner, "Interplay between topology and disorder in a two-dimensional semi-dirac material," *Physical Review B*, vol. 97, no. 2, p. 024204, 2018.

[12] D. Xiao, G.-B. Liu, W. Feng, X. Xu, and W. Yao, "Coupled spin and valley physics in monolayers of MoS_2 and other group-vi dichalcogenides," *Physical review letters*, vol. 108, no. 19, p. 196802, 2012.

[13] J. Lu, O. Zheliuk, I. Leermakers, N. F. Yuan, U. Zeitler, K. T. Law, and J. Ye, "Evidence for two-dimensional ising superconductivity in gated MoS_2," *Science*, vol. 350, no. 6266, pp. 1353–1357, 2015.

[14] N. F. Yuan, K. F. Mak, and K. Law, "Possible topological superconducting phases of MoS_2," *Physical review letters*, vol. 113, no. 9, p. 097001, 2014.

[15] Y.-T. Hsu, A. Vaezi, M. H. Fischer, and E.-A. Kim, "Topological superconductivity in monolayer transition metal dichalcogenides," *Nature communications*, vol. 8, no. 1, pp. 1–6, 2017.

[16] L. Šmejkal, Y. Mokrousov, B. Yan, and A. H. MacDonald, "Topological antiferromagnetic spintronics," *Nature physics*, vol. 14, no. 3, pp. 242–251, 2018.

[17] F. Zhang, "Brought to light," *Nature Physics*, vol. 14, no. 2, pp. 111–113, 2018.

[18] J. Sau, "A roadmap for a scalable topological quantum computer," *Physics*, vol. 10, p. 68, 2017.

[19] H. Zhang, C.-X. Liu, S. Gazibegovic, D. Xu, J. A. Logan, G. Wang, N. Van Loo, J. D. Bommer, M. W. De Moor, D. Car, *et al.*, "Quantized majorana conductance," *Nature*, vol. 556, no. 7699, pp. 74–79, 2018.

[20] P. A. M. Dirac, "The quantum theory of the electron," *Proceedings of the*

Royal Society of London. Series A, Containing Papers of a Mathematical and Physical Character, vol. 117, no. 778, pp. 610–624, 1928.

[21] E. Majorana, "Theory of the symmetry of electrons and positrons," *Nuovo Cim*, vol. 14, no. 171, p. 50, 1937.

[22] H. Weyl, "Elektron und gravitation. i," *Zeitschrift für Physik*, vol. 56, no. 5-6, pp. 330–352, 1929.

[23] A. M. Tsvelik, *Quantum field theory in condensed matter physics*. Cambridge university press, 2007.

[24] R. K. Ellis, W. J. Stirling, and B. R. Webber, *QCD and collider physics*. Cambridge university press, 2003.

[25] I. Merches, D. Tatomir, and R. E. Lupu, *Basics of quantum electrodynamics*. Taylor & Francis, 2013.

[26] P. A. M. Dirac, "A theory of electrons and protons," *Proceedings of the Royal Society of London. Series A, Containing papers of a mathematical and physical character*, vol. 126, no. 801, pp. 360–365, 1930.

[27] T. Wehling, A. M. Black-Schaffer, and A. V. Balatsky, "Dirac materials," *Advances in Physics*, vol. 63, no. 1, pp. 1–76, 2014.

[28] L. Zhang, J. Zhou, H. Li, L. Shen, and Y. P. Feng, "Recent progress and challenges in magnetic tunnel junctions with 2d materials for spintronic applications," *Applied Physics Reviews*, vol. 8, no. 2, p. 021308, 2021.

[29] K. S. Novoselov, A. K. Geim, S. V. Morozov, D.-e. Jiang, Y. Zhang, S. V. Dubonos, I. V. Grigorieva, and A. A. Firsov, "Electric field effect in atomically thin carbon films," *science*, vol. 306, no. 5696, pp. 666–669, 2004.

[30] K. S. Novoselov, V. Fal, L. Colombo, P. Gellert, M. Schwab, K. Kim, *et al.*, "A roadmap for graphene," *nature*, vol. 490, no. 7419, pp. 192–200, 2012.

[31] R. Mas-Balleste, C. Gomez-Navarro, J. Gomez-Herrero, and F. Zamora, "2d materials: to graphene and beyond," *Nanoscale*, vol. 3, no. 1, pp. 20–30, 2011.

[32] S. Z. Butler, S. M. Hollen, L. Cao, Y. Cui, J. A. Gupta, H. R. Gutiérrez,

T. F. Heinz, S. S. Hong, J. Huang, A. F. Ismach, *et al.*, "Progress, challenges, and opportunities in two-dimensional materials beyond graphene," *ACS nano*, vol. 7, no. 4, pp. 2898–2926, 2013.

[33] R. Rahman and S. Bandyopadhyay, "The cost of energy-efficiency in digital hardware: The trade-off between energy dissipation, energy–delay product and reliability in electronic, magnetic and optical binary switches," *Applied Sciences*, vol. 11, no. 12, p. 5590, 2021.

[34] C. Jin, F. Lin, K. Suenaga, and S. Iijima, "Fabrication of a freestanding boron nitride single layer and its defect assignments," *Physical review letters*, vol. 102, no. 19, p. 195505, 2009.

[35] H. J. Conley, B. Wang, J. I. Ziegler, R. F. Haglund Jr, S. T. Pantelides, and K. I. Bolotin, "Bandgap engineering of strained monolayer and bilayer MoS_2," *Nano letters*, vol. 13, no. 8, pp. 3626–3630, 2013.

[36] A. Castellanos-Gomez, R. Roldán, E. Cappelluti, M. Buscema, F. Guinea, H. S. van der Zant, and G. A. Steele, "Local strain engineering in atomically thin MoS_2," *Nano letters*, vol. 13, no. 11, pp. 5361–5366, 2013.

[37] N. Mounet, M. Gibertini, P. Schwaller, D. Campi, A. Merkys, A. Marrazzo, T. Sohier, I. E. Castelli, A. Cepellotti, G. Pizzi, *et al.*, "Two-dimensional materials from high-throughput computational exfoliation of experimentally known compounds," *Nature nanotechnology*, vol. 13, no. 3, pp. 246–252, 2018.

[38] A. B. Patel, H. K. Machhi, P. Chauhan, S. Narayan, V. Dixit, S. S. Soni, P. K. Jha, G. K. Solanki, K. D. Patel, and V. M. Pathak, "Electrophoretically deposited $MoSe_2/WSe_2$ heterojunction from ultrasonically exfoliated nanocrystals for enhanced electrochemical photoresponse," *ACS applied materials & interfaces*, vol. 11, no. 4, pp. 4093–4102, 2019.

[39] D. Zhong, K. L. Seyler, X. Linpeng, R. Cheng, N. Sivadas, B. Huang, E. Schmidgall, T. Taniguchi, K. Watanabe, M. A. McGuire, *et al.*, "Van der waals engineering of ferromagnetic semiconductor heterostructures for spin and valleytronics," *Science advances*, vol. 3, no. 5, p. e1603113, 2017.

[40] X. Tao, L. Zhang, X. Zheng, H. Hao, X. Wang, L. Song, Z. Zeng, and H. Guo, "h−BN/graphene van der waals vertical heterostructure: a fully spin-polarized photocurrent generator," *Nanoscale*, vol. 10, no. 1, pp. 174–183, 2018.

[41] R. Peierls, "Quelques propriétés typiques des corps solides," in *Annales de l'institut Henri Poincaré*, vol. 5, pp. 177–222, 1935.

[42] L. D. Landau and E. M. Lifshitz, *Course of theoretical physics*. Elsevier, 2013.

[43] N. D. Mermin, "Crystalline order in two dimensions," *Physical Review*, vol. 176, no. 1, p. 250, 1968.

[44] J. Evans, P. Thiel, and M. C. Bartelt, "Morphological evolution during epitaxial thin film growth: Formation of 2d islands and 3d mounds," *Surface Science Reports*, vol. 61, no. 1-2, pp. 1–128, 2006.

[45] A. Geim and K. Novoselov, "The rise of graphene, nature materials, 6," 2007.

[46] N. Peres and R. M. Ribeiro, "Focus on graphene," *New Journal of Physics*, vol. 11, no. 9, p. 095002, 2009.

[47] M. A. Poothanari, Y. B. Pottathara, and S. Thomas, "Carbon nanostructures for electromagnetic shielding applications," in *Industrial Applications of Nanomaterials*, pp. 205–223, Elsevier, 2019.

[48] A. W. Tsen, L. Brown, M. P. Levendorf, F. Ghahari, P. Y. Huang, R. W. Havener, C. S. Ruiz-Vargas, D. A. Muller, P. Kim, and J. Park, "Tailoring electrical transport across grain boundaries in polycrystalline graphene," *Science*, vol. 336, no. 6085, pp. 1143–1146, 2012.

[49] L. Liao, Y.-C. Lin, M. Bao, R. Cheng, J. Bai, Y. Liu, Y. Qu, K. L. Wang, Y. Huang, and X. Duan, "High-speed graphene transistors with a self-aligned nanowire gate," *Nature*, vol. 467, no. 7313, pp. 305–308, 2010.

[50] Y. Wu, Y.-m. Lin, A. A. Bol, K. A. Jenkins, F. Xia, D. B. Farmer, Y. Zhu, and P. Avouris, "High-frequency, scaled graphene transistors on diamond-like carbon," *Nature*, vol. 472, no. 7341, pp. 74–78, 2011.

[51] Y.-M. Lin, A. Valdes-Garcia, S.-J. Han, D. B. Farmer, I. Meric, Y. Sun, Y. Wu,

C. Dimitrakopoulos, A. Grill, P. Avouris, *et al.*, "Wafer-scale graphene integrated circuit," *Science*, vol. 332, no. 6035, pp. 1294–1297, 2011.

[52] M. P. Levendorf, C.-J. Kim, L. Brown, P. Y. Huang, R. W. Havener, D. A. Muller, and J. Park, "Graphene and boron nitride lateral heterostructures for atomically thin circuitry," *Nature*, vol. 488, no. 7413, pp. 627–632, 2012.

[53] S. Garaj, W. Hubbard, A. Reina, J. Kong, D. Branton, and J. Golovchenko, "Graphene as a subnanometre trans-electrode membrane," *Nature*, vol. 467, no. 7312, pp. 190–193, 2010.

[54] D. Rodrigo, O. Limaj, D. Janner, D. Etezadi, F. J. G. De Abajo, V. Pruneri, and H. Altug, "Mid-infrared plasmonic biosensing with graphene," *Science*, vol. 349, no. 6244, pp. 165–168, 2015.

[55] D. Voiry, J. Yang, J. Kupferberg, R. Fullon, C. Lee, H. Y. Jeong, H. S. Shin, and M. Chhowalla, "High-quality graphene via microwave reduction of solution-exfoliated graphene oxide," *Science*, vol. 353, no. 6306, pp. 1413–1416, 2016.

[56] Y. Zhu, S. Murali, M. D. Stoller, K. Ganesh, W. Cai, P. J. Ferreira, A. Pirkle, R. M. Wallace, K. A. Cychosz, M. Thommes, *et al.*, "Carbon-based supercapacitors produced by activation of graphene," *science*, vol. 332, no. 6037, pp. 1537–1541, 2011.

[57] M. Xu, D. Fujita, and N. Hanagata, "Perspectives and challenges of emerging single-molecule dna sequencing technologies," *Small*, vol. 5, no. 23, pp. 2638–2649, 2009.

[58] Y. Liu, "Application of graphene oxide in water treatment," in *IOP Conference Series: Earth and Environmental Science*, vol. 94, p. 012060, IOP Publishing, 2017.

[59] S. Bae, H. Kim, Y. Lee, X. Xu, J.-S. Park, Y. Zheng, J. Balakrishnan, T. Lei, H. R. Kim, Y. I. Song, *et al.*, "Roll-to-roll production of 30-inch graphene films for transparent electrodes," *Nature nanotechnology*, vol. 5, no. 8, pp. 574–578, 2010.

[60] X. Wang, L. Zhi, and K. Müllen, "Transparent, conductive graphene electrodes for dye-sensitized solar cells," *Nano letters*, vol. 8, no. 1, pp. 323–327, 2008.

[61] J. Xu, S. Singh, J. Katoch, G. Wu, T. Zhu, I. Žutić, and R. K. Kawakami, "Spin inversion in graphene spin valves by gate-tunable magnetic proximity effect at one-dimensional contacts," *Nature communications*, vol. 9, no. 1, pp. 1–6, 2018.

[62] J.-C. Charlier, P. C. Eklund, J. Zhu, and A. C. Ferrari, "Electron and phonon properties of graphene: their relationship with carbon nanotubes," *Carbon nanotubes*, pp. 673–709, 2007.

[63] K. S. Novoselov, A. K. Geim, S. V. Morozov, D. Jiang, M. I. Katsnelson, I. Grigorieva, S. Dubonos, Firsov, and AA, "Two-dimensional gas of massless dirac fermions in graphene," *nature*, vol. 438, no. 7065, pp. 197–200, 2005.

[64] Y. Zhang, Y.-W. Tan, H. L. Stormer, and P. Kim, "Experimental observation of the quantum hall effect and berry's phase in graphene," *nature*, vol. 438, no. 7065, pp. 201–204, 2005.

[65] I. Bialynicki-Birula and Z. Bialynicka-Birula, "Berryâs phase in the relativistic theory of spinning particles," *Physical Review D*, vol. 35, no. 8, p. 2383, 1987.

[66] B. Lv, H. Weng, B. Fu, X. P. Wang, H. Miao, J. Ma, P. Richard, X. Huang, L. Zhao, G. Chen, *et al.*, "Experimental discovery of weyl semimetal TaAs," *Physical Review X*, vol. 5, no. 3, p. 031013, 2015.

[67] C. Herring, "Effect of time-reversal symmetry on energy bands of crystals," *Physical Review*, vol. 52, no. 4, p. 361, 1937.

[68] H. B. Nielsen and M. Ninomiya, "The adler-bell-jackiw anomaly and weyl fermions in a crystal," *Physics Letters B*, vol. 130, no. 6, pp. 389–396, 1983.

[69] X. Wan, A. M. Turner, A. Vishwanath, and S. Y. Savrasov, "Topological semimetal and fermi-arc surface states in the electronic structure of pyrochlore iridates," *Physical Review B*, vol. 83, no. 20, p. 205101, 2011.

[70] K.-Y. Yang, Y.-M. Lu, and Y. Ran, "Quantum hall effects in a weyl semimetal:

Possible application in pyrochlore iridates," *Physical Review B*, vol. 84, no. 7, p. 075129, 2011.

[71] S.-M. Huang, S.-Y. Xu, I. Belopolski, C.-C. Lee, G. Chang, B. Wang, N. Alidoust, G. Bian, M. Neupane, C. Zhang, *et al.*, "A weyl fermion semimetal with surface fermi arcs in the transition metal monopnictide TaAs class," *Nature communications*, vol. 6, no. 1, pp. 1–6, 2015.

[72] H. Weng, C. Fang, Z. Fang, B. A. Bernevig, and X. Dai, "Weyl semimetal phase in noncentrosymmetric transition-metal monophosphides," *Physical Review X*, vol. 5, no. 1, p. 011029, 2015.

[73] S.-Y. Xu, I. Belopolski, N. Alidoust, M. Neupane, G. Bian, C. Zhang, R. Sankar, G. Chang, Z. Yuan, C.-C. Lee, *et al.*, "Discovery of a weyl fermion semimetal and topological fermi arcs," *Science*, vol. 349, no. 6248, pp. 613–617, 2015.

[74] C. Zhang, Z. Yuan, S. Xu, Z. Lin, B. Tong, M. Z. Hasan, J. Wang, C. Zhang, and S. Jia, "Tantalum monoarsenide: an exotic compensated semimetal," *arXiv preprint arXiv:1502.00251*, 2015.

[75] T. Ojanen, "Helical fermi arcs and surface states in time-reversal invariant weyl semimetals," *Physical Review B*, vol. 87, no. 24, p. 245112, 2013.

[76] A. C. Potter, I. Kimchi, and A. Vishwanath, "Quantum oscillations from surface fermi arcs in weyl and dirac semimetals," *Nature communications*, vol. 5, no. 1, pp. 1–6, 2014.

[77] Z. Fang, N. Nagaosa, K. S. Takahashi, A. Asamitsu, R. Mathieu, T. Ogasawara, H. Yamada, M. Kawasaki, Y. Tokura, and K. Terakura, "The anomalous hall effect and magnetic monopoles in momentum space," *Science*, vol. 302, no. 5642, pp. 92–95, 2003.

[78] G. B. Halász and L. Balents, "Time-reversal invariant realization of the weyl semimetal phase," *Physical Review B*, vol. 85, no. 3, p. 035103, 2012.

[79] A. Zyuzin, S. Wu, and A. Burkov, "Weyl semimetal with broken time reversal and inversion symmetries," *Physical Review B*, vol. 85, no. 16, p. 165110, 2012.

[80] F. Arnold, M. Naumann, S.-C. Wu, Y. Sun, M. Schmidt, H. Borrmann, C. Felser, B. Yan, and E. Hassinger, "Chiral weyl pockets and fermi surface topology of the weyl semimetal taas," *Physical review letters*, vol. 117, no. 14, p. 146401, 2016.

[81] M. Naumann, F. Arnold, Z. Medvecka, S.-C. Wu, V. Süss, M. Schmidt, B. Yan, N. Huber, L. Worch, M. A. Wilde, *et al.*, "Weyl nodes close to the fermi energy in nbas," *physica status solidi (b)*, vol. 259, no. 5, p. 2100165, 2022.

[82] G. E. Volovik, *Exotic properties of superfluid ^3He*, vol. 1. World Scientific, 1992.

[83] D. Vollhardt and P. Wolfle, "The superfluid phases of helium 3," *Taylor and Francis, London*, 1990.

[84] A. V. Balatsky, I. Vekhter, and J.-X. Zhu, "Impurity-induced states in conventional and unconventional superconductors," *Reviews of Modern Physics*, vol. 78, no. 2, p. 373, 2006.

[85] M. Z. Hasan and C. L. Kane, "Colloquium: topological insulators," *Reviews of modern physics*, vol. 82, no. 4, p. 3045, 2010.

[86] X.-L. Qi and S.-C. Zhang, "Topological insulators and superconductors," *Reviews of Modern Physics*, vol. 83, no. 4, p. 1057, 2011.

[87] J. Cayssol, "Introduction to dirac materials and topological insulators," *Comptes Rendus Physique*, vol. 14, no. 9-10, pp. 760–778, 2013.

[88] S. D. Sarma, S. Adam, E. Hwang, and E. Rossi, "Electronic transport in two-dimensional graphene," *Reviews of modern physics*, vol. 83, no. 2, p. 407, 2011.

[89] M. Vojta, "Quantum phase transitions," *Reports on Progress in Physics*, vol. 66, no. 12, p. 2069, 2003.

[90] L. Bayha, M. Holten, R. Klemt, K. Subramanian, J. Bjerlin, S. M. Reimann, G. M. Bruun, P. M. Preiss, and S. Jochim, "Observing the emergence of a quantum phase transition shell by shell," *nature*, vol. 587, no. 7835, pp. 583–587, 2020.

[91] S. Sachdev, *Quantum phase transitions*. Cambridge university press, 2011.

[92] "*Transitions in focus*," *Nature Phys*, vol. 4, p. 157, 2008.

[93] C. Li, G. Zhang, S. Lin, and Z. Song, "Quantum phase transition induced by real-space topology," *Scientific reports*, vol. 6, no. 1, pp. 1–7, 2016.

[94] S. L. Sondhi, S. Girvin, J. Carini, and D. Shahar, "Continuous quantum phase transitions," *Reviews of modern physics*, vol. 69, no. 1, p. 315, 1997.

[95] S. Sachdev, "Colloquium: Order and quantum phase transitions in the cuprate superconductors," *Reviews of Modern Physics*, vol. 75, no. 3, p. 913, 2003.

[96] K. Y. Bliokh, D. Leykam, M. Lein, and F. Nori, "Topological non-hermitian origin of surface maxwell waves," *Nature communications*, vol. 10, no. 1, pp. 1–7, 2019.

[97] T. Liu, J. J. He, F. Nori, *et al.*, "Majorana corner states in a two-dimensional magnetic topological insulator on a high-temperature superconductor," *Physical Review B*, vol. 98, no. 24, p. 245413, 2018.

[98] D. Leykam, K. Y. Bliokh, C. Huang, Y. D. Chong, and F. Nori, "Edge modes, degeneracies, and topological numbers in non-hermitian systems," *Physical review letters*, vol. 118, no. 4, p. 040401, 2017.

[99] S. H. Mousavi, A. B. Khanikaev, and Z. Wang, "Topologically protected elastic waves in phononic metamaterials," *Nature communications*, vol. 6, no. 1, pp. 1–7, 2015.

[100] M. Z. Hasan, C. L. Kane, *et al.*, "Topological insulators," *Rev. Mod. Phys*, vol. 82, no. 4, pp. 3045–3067, 2010.

[101] D. J. Thouless, M. Kohmoto, M. P. Nightingale, and M. den Nijs, "Quantized hall conductance in a two-dimensional periodic potential," *Physical review letters*, vol. 49, no. 6, p. 405, 1982.

[102] B. Huckestein, "Scaling theory of the integer quantum hall effect," *Reviews of Modern Physics*, vol. 67, no. 2, p. 357, 1995.

[103] X.-L. Qi, T. L. Hughes, and S.-C. Zhang, "Topological field theory of time-

reversal invariant insulators," *Physical Review B*, vol. 78, no. 19, p. 195424, 2008.

[104] J. Yu and C.-X. Liu, "Piezoelectricity and topological quantum phase transitions in two-dimensional spin-orbit coupled crystals with time-reversal symmetry," *Nature communications*, vol. 11, no. 1, pp. 1–9, 2020.

[105] H. Pan, Z. Li, C.-C. Liu, G. Zhu, Z. Qiao, and Y. Yao, "Valley-polarized quantum anomalous hall effect in silicene," *Physical review letters*, vol. 112, no. 10, p. 106802, 2014.

[106] H. Oike, F. Kagawa, N. Ogawa, A. Ueda, H. Mori, M. Kawasaki, and Y. Tokura, "Phase-change memory function of correlated electrons in organic conductors," *Physical Review B*, vol. 91, no. 4, p. 041101, 2015.

[107] Y. Hadad, A. B. Khanikaev, and A. Alu, "Self-induced topological transitions and edge states supported by nonlinear staggered potentials," *Physical Review B*, vol. 93, no. 15, p. 155112, 2016.

[108] S. Ganeshan, K. Sun, and S. D. Sarma, "Topological zero-energy modes in gapless commensurate aubry-andré-harper models," *Physical review letters*, vol. 110, no. 18, p. 180403, 2013.

[109] C. A. Downing and G. Weick, "Topological plasmons in dimerized chains of nanoparticles: robustness against long-range quasistatic interactions and retardation effects," *The European Physical Journal B*, vol. 91, no. 10, pp. 1–14, 2018.

[110] J. Shapiro, "The bulk-edge correspondence in three simple cases," *Reviews in Mathematical Physics*, vol. 32, no. 03, p. 2030003, 2020.

[111] E. Eberhard and R. Dreizler, "Density functional theory. an advanced course," 2011.

[112] E. Schrödinger, "Quantisierung als eigenwertproblem," *Annalen der physik*, vol. 385, no. 13, pp. 437–490, 1926.

[113] J. Kohanoff, *Electronic structure calculations for solids and molecules: theory*

and computational methods. Cambridge university press, 2006.

[114] D. J. Griffiths, *Introduction to quantum mechanics.* Pearson International Edition (Pearson Prentice Hall, Upper Saddle River, 2005), 1960.

[115] R. M. Martin, *Electronic structure: basic theory and practical methods.* Cambridge university press, 2020.

[116] J. C. Inkson, *Many-body theory of solids: an introduction.* Springer Science & Business Media, 2012.

[117] M. Born and R. Oppenheimer, "Zur quantentheorie der molekeln," *Annalen der physik*, vol. 389, no. 20, pp. 457–484, 1927.

[118] P. Ehrenfest, "Bemerkung über die angenäherte gültigkeit der klassischen mechanik innerhalb der quantenmechanik," *Zeitschrift für Physik*, vol. 45, no. 7-8, pp. 455–457, 1927.

[119] P. Güttinger, "Das verhalten von atomen im magnetischen drehfeld," *Zeitschrift für Physik*, vol. 73, no. 3, pp. 169–184, 1932.

[120] H. Hellman, "Einführung in die quantenchemie," *Franz Deuticke, Leipzig*, vol. 285, 1937.

[121] R. P. Feynman, "Forces in molecules," *Physical review*, vol. 56, no. 4, p. 340, 1939.

[122] W. Koch and M. C. Holthausen, *A chemist's guide to density functional theory.* John Wiley & Sons, 2015.

[123] J. P. Perdew and S. Kurth, "Density functionals for non-relativistic coulomb systems in the new century," in *A primer in density functional theory*, pp. 1–55, Springer, 2003.

[124] J.-L. Calais, "Density-functional theory of atoms and molecules. rg parr and w. yang, oxford university press, new york, oxford, 1989. ix+ 333 pp. price£ 45.00," 1993.

[125] R. Dreizler and E. Gross, "Density functional theory springer verlag," 1990.

[126] P. Hohenberg and W. Kohn, "Inhomogeneous electron gas," *Physical review*, vol. 136, no. 3B, p. B864, 1964.

[127] W. Kohn and L. J. Sham, "Self-consistent equations including exchange and correlation effects," *Physical review*, vol. 140, no. 4A, p. A1133, 1965.

[128] L. H. Thomas, "The calculation of atomic fields," in *Mathematical proceedings of the Cambridge philosophical society*, vol. 23, pp. 542–548, Cambridge University Press, 1927.

[129] F. Jüttner, "Die relativistische quantentheorie des idealen gases," *Zeitschrift für Physik*, vol. 47, no. 7-8, pp. 542–566, 1928.

[130] R. G. Parr and W. Yang, "Density-functional theory of atoms and molecules. international series of monographs on chemistry," *Oxford University Press, New York*, vol. 3, pp. 14312–14321, 1994.

[131] J. P. Perdew and K. Schmidt, "Jacobâs ladder of density functional approximations for the exchange-correlation energy," in *AIP Conference Proceedings*, vol. 577, pp. 1–20, American Institute of Physics, 2001.

[132] V. N. Staroverov, G. E. Scuseria, J. Tao, and J. P. Perdew, "Tests of a ladder of density functionals for bulk solids and surfaces," *Physical Review B*, vol. 69, no. 7, p. 075102, 2004.

[133] J. P. Perdew, A. Ruzsinszky, J. Tao, V. N. Staroverov, G. E. Scuseria, and G. I. Csonka, "Prescription for the design and selection of density functional approximations: More constraint satisfaction with fewer fits," *The Journal of chemical physics*, vol. 123, no. 6, p. 062201, 2005.

[134] A. V. Krukau, O. A. Vydrov, A. F. Izmaylov, and G. E. Scuseria, "Influence of the exchange screening parameter on the performance of screened hybrid functionals," *The Journal of chemical physics*, vol. 125, no. 22, p. 224106, 2006.

[135] J. P. Perdew, K. Burke, and M. Ernzerhof, "Generalized gradient approximation made simple," *Physical review letters*, vol. 77, no. 18, p. 3865, 1996.

[136] J. P. Perdew, A. Ruzsinszky, G. I. Csonka, O. A. Vydrov, G. E. Scuseria, L. A. Constantin, X. Zhou, and K. Burke, "Restoring the density-gradient expansion for exchange in solids and surfaces," *Physical review letters*, vol. 100, no. 13, p. 136406, 2008.

[137] C. Kittel, P. McEuen, and P. McEuen, *Introduction to solid state physics*, vol. 8. Wiley New York, 1996.

[138] N. Ashcroft and N. Mermin, "Solid state physics; thomson learning, inc," *Stamford, CT*, 1976.

[139] F. Bloch, "Über die quantenmechanik der elektronen in kristallgittern," *Zeitschrift für physik*, vol. 52, no. 7, pp. 555–600, 1929.

[140] C. Friedrich, "Tetrahedron integration method for strongly varying functions: Application to the g t self-energy," *Physical Review B*, vol. 100, no. 7, p. 075142, 2019.

[141] P. Lambin and J.-P. Vigneron, "Computation of crystal green's functions in the complex-energy plane with the use of the analytical tetrahedron method," *Physical Review B*, vol. 29, no. 6, p. 3430, 1984.

[142] H. J. Monkhorst and J. D. Pack, "Special points for brillouin-zone integrations," *Physical review B*, vol. 13, no. 12, p. 5188, 1976.

[143] J. C. Phillips and L. Kleinman, "New method for calculating wave functions in crystals and molecules," *Physical Review*, vol. 116, no. 2, p. 287, 1959.

[144] F. Nogueira, A. Castro, and M. A. Marques, "A tutorial on density functional theory," *A Primer in Density Functional Theory*, pp. 218–256, 2003.

[145] M. C. Payne, M. P. Teter, D. C. Allan, T. Arias, and a. J. Joannopoulos, "Iterative minimization techniques for ab initio total-energy calculations: molecular dynamics and conjugate gradients," *Reviews of modern physics*, vol. 64, no. 4, p. 1045, 1992.

[146] C. Herring, "A new method for calculating wave functions in crystals," *Physical Review*, vol. 57, no. 12, p. 1169, 1940.

[147] D. Hamann, M. Schlüter, and C. Chiang, "Norm-conserving pseudopotentials," *Physical Review Letters*, vol. 43, no. 20, p. 1494, 1979.

[148] G. B. Bachelet, D. R. Hamann, and M. Schlüter, "Pseudopotentials that work: From h to pu," *Physical Review B*, vol. 26, no. 8, p. 4199, 1982.

[149] G. Kresse and D. Joubert, "From ultrasoft pseudopotentials to the projector augmented-wave method," *Physical review b*, vol. 59, no. 3, p. 1758, 1999.

[150] P. E. Blöchl, "Projector augmented-wave method," *Physical review B*, vol. 50, no. 24, p. 17953, 1994.

[151] N. Holzwarth, G. Matthews, R. Dunning, A. Tackett, and Y. Zeng, "Comparison of the projector augmented-wave, pseudopotential, and linearized augmented-plane-wave formalisms for density-functional calculations of solids," *Physical Review B*, vol. 55, no. 4, p. 2005, 1997.

[152] R. Martin, "Electronic structure–basic theory and practical methods, cambridge univ," *Pr., West Nyack, NY*, 2004.

[153] D. Vanderbilt, "Soft self-consistent pseudopotentials in a generalized eigenvalue formalism," *Physical review B*, vol. 41, no. 11, p. 7892, 1990.

[154] D. Hobbs, G. Kresse, and J. Hafner, "Fully unconstrained noncollinear magnetism within the projector augmented-wave method," *Physical Review B*, vol. 62, no. 17, p. 11556, 2000.

[155] P. L. Taylor, P. L. Taylor, O. Heinonen, *et al.*, *A quantum approach to condensed matter physics*. Cambridge University Press, 2002.

[156] L. L. Foldy and S. A. Wouthuysen, "On the dirac theory of spin 1/2 particles and its non-relativistic limit," *Physical Review*, vol. 78, no. 1, p. 29, 1950.

[157] L. Foldy, "The electromagnetic properties of dirac particles," *Physical Review*, vol. 87, no. 5, p. 688, 1952.

[158] S. Weinberg, *Lectures on quantum mechanics*. Cambridge University Press, 2015.

[159] I. O. Abdallah Ali, *A First-Principles Study on Phase Stability, Electronic*

Structure and optical properties of some halide perovskites for photovoltaic applications. PhD thesis, 2019.

[160] S. Majumdar, H. Majumdar, and R. Österbacka, "Comprehensive nanoscience and technology, vol. 1," 2011.

[161] M. Johnson, P. Bloemen, F. Den Broeder, and J. De Vries, "Magnetic anisotropy in metallic multilayers," *Reports on Progress in Physics*, vol. 59, no. 11, p. 1409, 1996.

[162] D. L. Mills and S. M. Rezende, "Spin damping in ultrathin magnetic films," *Spin Dynamics in Confined Magnetic Structures II*, pp. 27–59, 2003.

[163] M. Wu, J. Jiang, and M. Weng, "Spin dynamics in semiconductors," *Physics Reports*, vol. 493, no. 2-4, pp. 61–236, 2010.

[164] N. Nagaosa, J. Sinova, S. Onoda, A. H. MacDonald, and N. P. Ong, "Anomalous hall effect," *Reviews of modern physics*, vol. 82, no. 2, p. 1539, 2010.

[165] J. C. Slater and G. F. Koster, "Simplified lcao method for the periodic potential problem," *Physical Review*, vol. 94, no. 6, p. 1498, 1954.

[166] J. Fry, N. Brener, F. Case, and N. Desai, "Two-center approximation in the quantum theory of solids," *Physical Review B*, vol. 15, no. 12, p. 5811, 1977.

[167] Y. F. Suprunenko, E. Gorbar, V. Loktev, and S. Sharapov, "Effect of next-nearest-neighbor hopping on the electronic properties of graphene," *Low Temperature Physics*, vol. 34, no. 10, pp. 812–817, 2008.

[168] F. Utermohlen, "Tight-binding model for graphene," 2018. Available at: https://cpb-us-w2.wpmucdn.com/u.osu.edu/dist/3/67057/files/2018/09/graphene_tight-binding_model-1ny95f1.pdf, Accessed on 17 July 2022.

[169] S. J. Chae, F. Güneş, K. K. Kim, E. S. Kim, G. H. Han, S. M. Kim, H.-J. Shin, S.-M. Yoon, J.-Y. Choi, M. H. Park, *et al.*, "Synthesis of large-area graphene layers on poly-nickel substrate by chemical vapor deposition: wrinkle formation," *Advanced materials*, vol. 21, no. 22, pp. 2328–2333, 2009.

[170] E. Runge and E. K. Gross, "Density-functional theory for time-dependent systems," *Physical review letters*, vol. 52, no. 12, p. 997, 1984.

[171] E. Makkonen, T. P. Rossi, A. H. Larsen, O. Lopez-Acevedo, P. Rinke, M. Kuisma, and X. Chen, "Real-time time-dependent density functional theory implementation of electronic circular dichroism applied to nanoscale metal–organic clusters," *The Journal of Chemical Physics*, vol. 154, no. 11, p. 114102, 2021.

[172] J. J. Mortensen, L. B. Hansen, and K. W. Jacobsen, "Real-space grid implementation of the projector augmented wave method," *Physical Review B*, vol. 71, no. 3, p. 035109, 2005.

[173] J. Enkovaara, C. Rostgaard, J. J. Mortensen, J. Chen, M. Dułak, L. Ferrighi, J. Gavnholt, C. Glinsvad, V. Haikola, H. Hansen, *et al.*, "Electronic structure calculations with gpaw: a real-space implementation of the projector augmented-wave method," *Journal of physics: Condensed matter*, vol. 22, no. 25, p. 253202, 2010.

[174] A. H. Larsen, M. Vanin, J. J. Mortensen, K. S. Thygesen, and K. W. Jacobsen, "Localized atomic basis set in the projector augmented wave method," *Physical Review B*, vol. 80, no. 19, p. 195112, 2009.

[175] M. Kuisma, A. Sakko, T. P. Rossi, A. H. Larsen, J. Enkovaara, L. Lehtovaara, and T. T. Rantala, "Localized surface plasmon resonance in silver nanoparticles: Atomistic first-principles time-dependent density-functional theory calculations," *Physical Review B*, vol. 91, no. 11, p. 115431, 2015.

[176] A. Smogunov, A. Dal Corso, and E. Tosatti, "Ballistic conductance of magnetic Co and Ni nanowires with ultrasoft pseudopotentials," *Physical Review B*, vol. 70, no. 4, p. 045417, 2004.

[177] B. Larade, J. Taylor, H. Mehrez, and H. Guo, "Conductance, i- v curves, and negative differential resistance of carbon atomic wires," *Physical Review B*, vol. 64, no. 7, p. 075420, 2001.

[178] M. Brandbyge, J.-L. Mozos, P. Ordejón, J. Taylor, and K. Stokbro, "Density-

functional method for nonequilibrium electron transport," *Physical Review B*, vol. 65, no. 16, p. 165401, 2002.

[179] J. Palacios, A. Pérez-Jiménez, E. Louis, E. SanFabián, and J. Vergés, "First-principles phase-coherent transport in metallic nanotubes with realistic contacts," *Physical review letters*, vol. 90, no. 10, p. 106801, 2003.

[180] K. S. Thygesen, M. Bollinger, and K. W. Jacobsen, "Conductance calculations with a wavelet basis set," *Physical Review B*, vol. 67, no. 11, p. 115404, 2003.

[181] N. Lang, "Resistance of atomic wires," *Physical Review B*, vol. 52, no. 7, p. 5335, 1995.

[182] V. Shukla, *Computational Studies of 2D Materials: Application to Energy Storage and Electron Transport in Nanoscale Devices*. PhD thesis, Acta Universitatis Upsaliensis, 2019.

[183] D. S. Fisher and P. A. Lee, "Relation between conductivity and transmission matrix," *Physical Review B*, vol. 23, no. 12, p. 6851, 1981.

[184] M. B. Nardelli, "Electronic transport in extended systems: Application to carbon nanotubes," *Physical Review B*, vol. 60, no. 11, p. 7828, 1999.

[185] C.-L. Zhang, S.-Y. Xu, I. Belopolski, Z. Yuan, Z. Lin, B. Tong, G. Bian, N. Alidoust, C.-C. Lee, S.-M. Huang, *et al.*, "Signatures of the adler–bell–jackiw chiral anomaly in a weyl fermion semimetal," *Nature communications*, vol. 7, no. 1, pp. 1–9, 2016.

[186] P. Giannozzi, S. Baroni, N. Bonini, M. Calandra, R. Car, C. Cavazzoni, D. Ceresoli, G. L. Chiarotti, M. Cococcioni, I. Dabo, *et al.*, "Quantum espresso: a modular and open-source software project for quantum simulations of materials," *Journal of physics: Condensed matter*, vol. 21, no. 39, p. 395502, 2009.

[187] M. Methfessel and A. Paxton, "High-precision sampling for brillouin-zone integration in metals," *Physical Review B*, vol. 40, no. 6, p. 3616, 1989.

[188] Y. Nishida, "Renormalization group analysis of graphene with a supercritical

coulomb impurity," *Physical Review B*, vol. 94, no. 8, p. 085430, 2016.

[189] M. S. Foster and I. L. Aleiner, "Graphene via large n: A renormalization group study," *Physical Review B*, vol. 77, no. 19, p. 195413, 2008.

[190] A. M. Ukpong, "Axial field induced spin response in Fe/hBN-based tunnel junctions," *Physical Review B*, vol. 100, no. 3, p. 035424, 2019.

[191] A. M. Ukpong, "Ab initio studies of coherent spin transport in Fe−hBN/graphene van der waals multilayers," *Journal of Physics: Condensed Matter*, vol. 29, no. 28, p. 285302, 2017.

[192] A. M. Ukpong, "Tunable magnetotransport in Fe/hBN/graphene/hBN/Pt(Fe) epitaxial multilayers," *Journal of Physics D: Applied Physics*, vol. 51, no. 9, p. 095302, 2018.

[193] M. Piquemal-Banci, R. Galceran, S. Caneva, M.-B. Martin, R. Weatherup, P. Kidambi, K. Bouzehouane, S. Xavier, A. Anane, F. Petroff, *et al.*, "Magnetic tunnel junctions with monolayer hexagonal boron nitride tunnel barriers," *Applied Physics Letters*, vol. 108, no. 10, p. 102404, 2016.

[194] M. Gurram, S. Omar, and B. J. van Wees, "Bias induced up to 100% spin-injection and detection polarizations in ferromagnet/bilayer−hBN/graphene/hBN heterostructures," *Nature communications*, vol. 8, no. 1, pp. 1–7, 2017.

[195] M. Piquemal-Banci, R. Galceran, M.-B. Martin, F. Godel, A. Anane, F. Petroff, B. Dlubak, and P. Seneor, "2d-mtjs: introducing 2d materials in magnetic tunnel junctions," *Journal of Physics D: Applied Physics*, vol. 50, no. 20, p. 203002, 2017.

[196] C. R. Dean, A. F. Young, I. Meric, C. Lee, L. Wang, S. Sorgenfrei, K. Watanabe, T. Taniguchi, P. Kim, K. L. Shepard, *et al.*, "Boron nitride substrates for high-quality graphene electronics," *Nature nanotechnology*, vol. 5, no. 10, pp. 722–726, 2010.

[197] K. F. Mak, C. Lee, J. Hone, J. Shan, and T. F. Heinz, "Atomically thin MoS_2: a new direct-gap semiconductor," *Physical review letters*, vol. 105, no. 13,

p. 136805, 2010.

[198] H. Zhang, M. Ye, Y. Wang, R. Quhe, Y. Pan, Y. Guo, Z. Song, J. Yang, W. Guo, and J. Lu, "Magnetoresistance in Co/2DMoS$_2$/Co and Ni/2DMoS$_2$/Ni junctions," *Physical Chemistry Chemical Physics*, vol. 18, no. 24, pp. 16367–16376, 2016.

[199] A. H. Larsen, J. J. Mortensen, J. Blomqvist, I. E. Castelli, R. Christensen, M. Dułak, J. Friis, M. N. Groves, B. Hammer, C. Hargus, *et al.*, "The atomic simulation environmentâa python library for working with atoms," *Journal of Physics: Condensed Matter*, vol. 29, no. 27, p. 273002, 2017.

[200] T. Thonhauser, S. Zuluaga, C. Arter, K. Berland, E. Schröder, and P. Hyldgaard, "Spin signature of nonlocal correlation binding in metal-organic frameworks," *Physical review letters*, vol. 115, no. 13, p. 136402, 2015.

[201] D. Langreth, B. I. Lundqvist, S. D. Chakarova-Käck, V. Cooper, M. Dion, P. Hyldgaard, A. Kelkkanen, J. Kleis, L. Kong, S. Li, *et al.*, "A density functional for sparse matter," *Journal of Physics: Condensed Matter*, vol. 21, no. 8, p. 084203, 2009.

[202] K. Berland, V. R. Cooper, K. Lee, E. Schröder, T. Thonhauser, P. Hyldgaard, and B. I. Lundqvist, "van der waals forces in density functional theory: a review of the vdw-df method," *Reports on Progress in Physics*, vol. 78, no. 6, p. 066501, 2015.

[203] N. Marzari, D. Vanderbilt, A. De Vita, and M. Payne, "Thermal contraction and disordering of the al(110) surface," *Physical review letters*, vol. 82, no. 16, p. 3296, 1999.

[204] N. Richter, *Electronic and magnetic properties of selected two-dimensional materials*. PhD thesis, Johannes Gutenberg-Universität Mainz, 2017.

[205] T. Garandel, R. Arras, X. Marie, P. Renucci, and L. Calmels, "Electronic structure of the co(0001)/MoS$_2$ interface and its possible use for electrical spin injection in a single MoS$_2$ layer," *Physical Review B*, vol. 95, no. 7, p. 075402, 2017.

[206] T. Garandel, R. Arras, X. Marie, P. Renucci, and L. Calmels, "Charge transfer and magnetization of a MoS_2 monolayer at the co(0001)/MoS_2 interface," in *Journal of Physics: Conference Series*, vol. 903, p. 012017, IOP Publishing, 2017.

[207] H. J. Choi and J. Ihm, "Ab initio pseudopotential method for the calculation of conductance in quantum wires," *Physical Review B*, vol. 59, no. 3, p. 2267, 1999.

[208] S. Wu, J. S. Ross, G.-B. Liu, G. Aivazian, A. Jones, Z. Fei, W. Zhu, D. Xiao, W. Yao, D. Cobden, *et al.*, "Electrical tuning of valley magnetic moment through symmetry control in bilayer mos2," *Nature Physics*, vol. 9, no. 3, pp. 149–153, 2013.

[209] A. Saxena, "Broken symmetry, ferroic phase transitions and multifunctional materials," *Integrated Ferroelectrics*, vol. 131, no. 1, pp. 3–24, 2011.

[210] D. Xiao, M.-C. Chang, and Q. Niu, "Berry phase effects on electronic properties," *Reviews of modern physics*, vol. 82, no. 3, p. 1959, 2010.

[211] X. Xu, W. Yao, D. Xiao, and T. F. Heinz, "Spin and pseudospins in layered transition metal dichalcogenides," *Nature Physics*, vol. 10, no. 5, pp. 343–350, 2014.

[212] W.-K. Tse, Z. Qiao, Y. Yao, A. MacDonald, and Q. Niu, "Quantum anomalous hall effect in single-layer and bilayer graphene," *Physical Review B*, vol. 83, no. 15, p. 155447, 2011.

[213] H. Min, J. Hill, N. A. Sinitsyn, B. Sahu, L. Kleinman, and A. H. MacDonald, "Intrinsic and rashba spin-orbit interactions in graphene sheets," *Physical Review B*, vol. 74, no. 16, p. 165310, 2006.

[214] D. Sheng, Z. Weng, L. Sheng, and F. Haldane, "Quantum spin-hall effect and topologically invariant chern numbers," *Physical review letters*, vol. 97, no. 3, p. 036808, 2006.

[215] Z. Qiao, S. A. Yang, W. Feng, W.-K. Tse, J. Ding, Y. Yao, J. Wang, and Q. Niu, "Quantum anomalous hall effect in graphene from rashba and exchange

effects," *Physical Review B*, vol. 82, no. 16, p. 161414, 2010.

[216] Y. Yang, Z. Xu, L. Sheng, B. Wang, D. Xing, and D. Sheng, "Time-reversal-symmetry-broken quantum spin hall effect," *Physical review letters*, vol. 107, no. 6, p. 066602, 2011.

[217] E. Blount, "Bloch electrons in a magnetic field," *Physical Review*, vol. 126, no. 5, p. 1636, 1962.

[218] G. H. Wannier, "Dynamics of band electrons in electric and magnetic fields," *Reviews of Modern Physics*, vol. 34, no. 4, p. 645, 1962.

[219] J. Luttinger, "The effect of a magnetic field on electrons in a periodic potential," *Physical Review*, vol. 84, no. 4, p. 814, 1951.

[220] W. Kohn, "Theory of bloch electrons in a magnetic field: the effective hamiltonian," *Physical Review*, vol. 115, no. 6, p. 1460, 1959.

[221] H. Fischbeck, "Theory of bloch electrons in a magnetic field," *physica status solidi (b)*, vol. 38, no. 1, pp. 11–62, 1970.

[222] J. L. Villanueva, *Topological electronic phases in graphene*. PhD thesis, Universidad de Santiago de Compostela, 2016.

[223] C. L. Kane and E. J. Mele, "Z_2 topological order and the quantum spin hall effect," *Physical review letters*, vol. 95, no. 14, p. 146802, 2005.

[224] C. L. Kane and E. J. Mele, "Quantum spin hall effect in graphene," *Physical review letters*, vol. 95, no. 22, p. 226801, 2005.

[225] X.-G. Wen, *Quantum field theory of many-body systems: from the origin of sound to an origin of light and electrons*. OUP Oxford, 2004.

[226] B. Bernevig and T. Hughes, "Topological insulators and topological superconductors princeton univ," 2013.

[227] L. Balents, "Weyl electrons kiss," *Physics*, vol. 4, p. 36, 2011.

[228] C. Zhang, S.-Y. Xu, I. Belopolski, Z. Yuan, Z. Lin, B. Tong, N. Alidoust, C.-C. Lee, S.-M. Huang, H. Lin, *et al.*, "Observation of the adler-bell-jackiw chiral

anomaly in a weyl semimetal," *arXiv preprint arXiv:1503.02630*, 2015.

[229] J. Murray, J. Taylor, L. Calvert, Y. Wang, E. Gabe, and J. Despault, "Phase relationships and thermodynamics of refractory metal pnictides: the metal-rich tantalum arsenides," *Journal of the Less Common Metals*, vol. 46, no. 2, pp. 311–320, 1976.

[230] B. Yan and C. Felser, "Topological materials: Weyl semimetals," *Annual Review of Condensed Matter Physics*, vol. 8, pp. 337–354, 2017.

[231] J. Buckeridge, D. Jevdokimovs, C. Catlow, and A. Sokol, "Bulk electronic, elastic, structural, and dielectric properties of the weyl semimetal TaAs," *Physical Review B*, vol. 93, no. 12, p. 125205, 2016.

[232] M. Zeng, W. Huang, and G. Liang, "Spin-dependent thermoelectric effects in graphene-based spin valves," *Nanoscale*, vol. 5, no. 1, pp. 200–208, 2013.

[233] S. Murakami, S. Iso, Y. Avishai, M. Onoda, and N. Nagaosa, "Tuning phase transition between quantum spin hall and ordinary insulating phases," *Physical Review B*, vol. 76, no. 20, p. 205304, 2007.

[234] X.-H. Chen, I. McCulloch, M. T. Batchelor, and H.-Q. Zhou, "Symmetry-protected trivial phases and quantum phase transitions in an anisotropic antiferromagnetic spin-1 biquadratic model," *Physical Review B*, vol. 102, no. 8, p. 085146, 2020.

[235] F. D. M. Haldane, "Model for a quantum hall effect without landau levels: Condensed-matter realization of the" parity anomaly"," *Physical review letters*, vol. 61, no. 18, p. 2015, 1988.

[236] N. Teleman, "The index theorem for topological manifolds," *Acta Mathematica*, vol. 153, pp. 117–152, 1984.

[237] S. V. Faleev, S. S. Parkin, and O. N. Mryasov, "Brillouin zone spin filtering mechanism of enhanced tunneling magnetoresistance and correlation effects in a co(0001)/h−BN/co(0001) magnetic tunnel junction," *Physical Review B*, vol. 92, no. 23, p. 235118, 2015.

[238] H. Zhong, R. Quhe, Y. Wang, Z. Ni, M. Ye, Z. Song, Y. Pan, J. Yang, L. Yang, M. Lei, *et al.*, "Interfacial properties of monolayer and bilayer MoS_2 contacts with metals: beyond the energy band calculations," *Scientific reports*, vol. 6, no. 1, pp. 1–16, 2016.

[239] J. Zhu, Y. Lan, H. Du, Y. Zhang, and J. Su, "Tuning water transport through nanochannels by changing the direction of an external electric field," *Physical Chemistry Chemical Physics*, vol. 18, no. 27, pp. 17991–17996, 2016.

[240] W. Wang, A. Narayan, L. Tang, K. Dolui, Y. Liu, X. Yuan, Y. Jin, Y. Wu, I. Rungger, S. Sanvito, *et al.*, "Spin-valve effect in NiFe/MoS_2/NiFe junctions," *Nano letters*, vol. 15, no. 8, pp. 5261–5267, 2015.

[241] S. F. Matar, A. Houari, and M. Belkhir, "Ab initio studies of magnetic properties of cobalt and tetracobalt nitride Co_4N," *Physical Review B*, vol. 75, no. 24, p. 245109, 2007.

[242] J. Wang, J. Hu, J. Ma, J. Zhang, L. Chen, and C. Nan, "Full 180 magnetization reversal with electric fields," *Scientific reports*, vol. 4, no. 1, pp. 1–6, 2014.

[243] S.-W. Yang, R.-C. Peng, T. Jiang, Y.-K. Liu, L. Feng, J.-J. Wang, L.-Q. Chen, X.-G. Li, and C.-W. Nan, "Non-volatile 180° magnetization reversal by an electric field in multiferroic heterostructures," *Advanced Materials*, vol. 26, no. 41, pp. 7091–7095, 2014.

[244] A. Moskaltsova, J. Krieft, D. Graulich, T. Matalla-Wagner, and T. Kuschel, "Impact of the magnetic proximity effect in pt on the total magnetic moment of pt/co/ta trilayers studied by x-ray resonant magnetic reflectivity," *AIP Advances*, vol. 10, no. 1, p. 015154, 2020.

[245] D.-O. Kim, K. M. Song, Y. Choi, B.-C. Min, J.-S. Kim, J. W. Choi, and D. R. Lee, "Asymmetric magnetic proximity effect in a pd/co/pd trilayer system," *Scientific reports*, vol. 6, no. 1, pp. 1–8, 2016.

[246] C. Lee, F. Katmis, P. Jarillo-Herrero, J. S. Moodera, and N. Gedik, "Direct measurement of proximity-induced magnetism at the interface between a topological insulator and a ferromagnet," *Nature communications*, vol. 7,

no. 1, pp. 1–6, 2016.

[247] A. M. Ukpong and N. Chetty, "Half-metallic ferromagnetism in substitutionally doped boronitrene," *Physical Review B*, vol. 86, no. 19, p. 195409, 2012.

[248] J. Yao, X. Song, X. Gao, G. Tian, P. Li, H. Fan, Z. Huang, W. Yang, D. Chen, Z. Fan, *et al.*, "Electrically driven reversible magnetic rotation in nanoscale multiferroic heterostructures," *ACS nano*, vol. 12, no. 7, pp. 6767–6776, 2018.

[249] S. Manipatruni, D. E. Nikonov, C.-C. Lin, B. Prasad, Y.-L. Huang, A. R. Damodaran, Z. Chen, R. Ramesh, and I. A. Young, "Voltage control of unidirectional anisotropy in ferromagnet-multiferroic system," *Science advances*, vol. 4, no. 11, p. eaat4229, 2018.

[250] J. Tong, F. Luo, L. Ruan, G. Qin, L. Zhou, F. Tian, and X. Zhang, "Publisher's note:"high and reversible spin polarization in a collinear antiferromagnet"[appl. phys. rev. 7, 031405 (2020)]," *Applied Physics Reviews*, vol. 7, no. 3, p. 039901, 2020.

[251] Z. Liu, H. Chen, J. Wang, J. Liu, K. Wang, Z. Feng, H. Yan, X. Wang, C. Jiang, J. Coey, *et al.*, "Electrical switching of the topological anomalous hall effect in a non-collinear antiferromagnet above room temperature," *Nature Electronics*, vol. 1, no. 3, pp. 172–177, 2018.

[252] K. Dolui, A. Narayan, I. Rungger, and S. Sanvito, "Efficient spin injection and giant magnetoresistance in Fe/MoS_2/Fe junctions," *Physical Review B*, vol. 90, no. 4, p. 041401, 2014.

[253] J. Kang, W. Liu, and K. Banerjee, "High-performance MoS_2 transistors with low-resistance molybdenum contacts," *Applied Physics Letters*, vol. 104, no. 9, p. 093106, 2014.

[254] D. Y. Qiu, H. Felipe, and S. G. Louie, "Optical spectrum of MoS_2: many-body effects and diversity of exciton states," *Physical review letters*, vol. 111, no. 21, p. 216805, 2013.

[255] B. K. Nikolic and P. B. Allen, "Quantum transport in ballistic conductors: evolution from conductance quantization to resonant tunnelling," *Journal of*

Physics: Condensed Matter, vol. 12, no. 46, p. 9629, 2000.

[256] M. Julliere, "Tunneling between ferromagnetic films," *Physics letters A*, vol. 54, no. 3, pp. 225–226, 1975.

[257] E. Y. Tsymbal, O. N. Mryasov, and P. R. LeClair, "Spin-dependent tunnelling in magnetic tunnel junctions," *Journal of Physics: Condensed Matter*, vol. 15, no. 4, p. R109, 2003.

[258] J. S. Moodera, L. R. Kinder, T. M. Wong, and R. Meservey, "Large magnetoresistance at room temperature in ferromagnetic thin film tunnel junctions," *Physical review letters*, vol. 74, no. 16, p. 3273, 1995.

[259] J. MacLaren, X.-G. Zhang, and W. Butler, "Validity of the julliere model of spin-dependent tunneling," *Physical Review B*, vol. 56, no. 18, p. 11827, 1997.

[260] K. Capelle, G. Vignale, and C. A. Ullrich, "Spin gaps and spin-flip energies in density-functional theory," *Physical Review B*, vol. 81, no. 12, p. 125114, 2010.

[261] A. M. Ukpong, "Emergence of nontrivial spin textures in frustrated van der waals ferromagnets," *Nanomaterials*, vol. 11, no. 7, p. 1770, 2021.

[262] Q. Tong, M. Chen, and W. Yao, "Magnetic proximity effect in a van der waals moiré superlattice," *Physical Review Applied*, vol. 12, no. 2, p. 024031, 2019.

[263] M. Bora and P. Deb, "Magnetic proximity effect in two-dimensional van der waals heterostructure," *Journal of Physics: Materials*, vol. 4, no. 3, p. 034014, 2021.

[264] Z. Wang, I. Gutiérrez-Lezama, N. Ubrig, M. Kroner, M. Gibertini, T. Taniguchi, K. Watanabe, A. Imamoğlu, E. Giannini, and A. F. Morpurgo, "Very large tunneling magnetoresistance in layered magnetic semiconductor CrI_3," *Nature communications*, vol. 9, no. 1, pp. 1–8, 2018.

[265] S. Li, Z. Ye, X. Luo, G. Ye, H. H. Kim, B. Yang, S. Tian, C. Li, H. Lei, A. W. Tsen, *et al.*, "Magnetic-field-induced quantum phase transitions in a van der waals magnet," *Physical Review X*, vol. 10, no. 1, p. 011075, 2020.

[266] M. Arai, R. Moriya, N. Yabuki, S. Masubuchi, K. Ueno, and T. Machida,

"Construction of van der waals magnetic tunnel junction using ferromagnetic layered dichalcogenide," *Applied Physics Letters*, vol. 107, no. 10, p. 103107, 2015.

[267] S. A. Maier *et al.*, *Plasmonics: fundamentals and applications*, vol. 1. Springer, 2007.

[268] D. Solis Jr, B. Willingham, S. L. Nauert, L. S. Slaughter, J. Olson, P. Swanglap, A. Paul, W.-S. Chang, and S. Link, "Electromagnetic energy transport in nanoparticle chains via dark plasmon modes," *Nano letters*, vol. 12, no. 3, pp. 1349–1353, 2012.

[269] F. Marchesin, P. Koval, M. Barbry, J. Aizpurua, and D. Sanchez-Portal, "Plasmonic response of metallic nanojunctions driven by single atom motion: quantum transport revealed in optics," *ACS Photonics*, vol. 3, no. 2, pp. 269–277, 2016.

[270] N. Fukuoka and K. Tanabe, "Lightning-rod effect of plasmonic field enhancement on hydrogen-absorbing transition metals," *Nanomaterials*, vol. 9, no. 9, p. 1235, 2019.

[271] M. Urbieta, M. Barbry, Y. Zhang, P. Koval, D. Sánchez-Portal, N. Zabala, and J. Aizpurua, "Atomic-scale lightning rod effect in plasmonic picocavities: A classical view to a quantum effect," *ACS nano*, vol. 12, no. 1, pp. 585–595, 2018.

[272] T. B. Ngwenya, A. M. Ukpong, and N. Chetty, "Defect states of complexes involving a vacancy on the boron site in boronitrene," *Physical Review B*, vol. 84, no. 24, p. 245425, 2011.